



TECHNICKÁ UNIVERZITA V LIBERCI
www.tul.cz

LIBEREC | ZITTAU/GÖRLITZ | JELENIA GÓRA



ACC JOURNAL XXV 1/2019

Issue A

Natural Sciences and Technology



INTERNATIONALES
HOCHSCHULINSTITUT
ZITTAU

ZENTRALE WISSENSCHAFTLICHE
EINRICHTUNG DER TU DRESDEN



Uniwersytet Ekonomiczny
we Wrocławiu

TECHNICKÁ UNIVERZITA V LIBERCI

HOCHSCHULE ZITTAU/GÖRLITZ

INTERNATIONALES HOCHSCHULINSTITUT ZITTAU (TU DRESDEN)

UNIWERSYTET EKONOMICZNY WE WROCŁAWIU

WYDZIAŁ EKONOMII, ZARZĄDZANIA I TURYSTYKI W JELENIEJ GÓRZE

Indexed in:

INDEX  COPERNICUS
I N T E R N A T I O N A L

Liberec – Zittau/Görlitz – Wrocław/Jelenia Góra

© **Technická univerzita v Liberci 2019**

ISSN 1803-9782 (Print)

ISSN 2571-0613 (Online)

ACC JOURNAL je mezinárodní vědecký časopis, jehož vydavatelem je Technická univerzita v Liberci. Na jeho tvorbě se podílí čtyři vysoké školy sdružené v Akademickém koordinačním středisku v Euroregionu Nisa (ACC). Ročně vycházejí zpravidla tři čísla.

ACC JOURNAL je periodikum publikující původní recenzované vědecké práce, vědecké studie, příspěvky ke konferencím a výzkumným projektům. První číslo obsahuje příspěvky zaměřené na oblast přírodních věd a techniky, druhé číslo je zaměřeno na oblast ekonomie, třetí číslo pojednává o tématech ze společenských věd. ACC JOURNAL má charakter recenzovaného časopisu. Jeho vydání navazuje na sborník „Vědecká pojednání“, který vycházel v letech 1995-2008.

ACC JOURNAL is an international scientific journal. It is published by the Technical University of Liberec. Four universities united in the Academic Coordination Centre in the Euroregion Nisa participate in its production. There are usually three issues of the journal annually.

ACC JOURNAL is a periodical publishing original reviewed scientific papers, scientific studies, papers presented at conferences, and findings of research projects. The first issue focuses on natural sciences and technology, the second issue deals with the science of economics, and the third issue contains findings from the area of social sciences. ACC JOURNAL is a reviewed one. It is building upon the tradition of the “Scientific Treatises” published between 1995 and 2008.

Hlavní recenzenti (major reviewers):

Ing. Darina Jašíková, Ph.D.

Technical University of Liberec
Institute for Nanomaterials, Advanced Technology and
Innovation (CxI)
Czech Republic

Ing. Vojtěch Radolf, Ph.D.

The Czech Academy of Sciences
Institute of Thermomechanics
Czech Republic

Contents

Research Articles

Sloshing Simulation of a Tank Oscillating Towards Multiple Degrees of Freedom by Particle Method.....	7
Shigeyuki Hibi; Kazuki Yabushita	
The Experimental Study of Diffuser Geometry for Low Pressure Exhaust Casing of Steam Turbine.....	17
Robert Kalista; Lukáš Kanta; Lev Feldberg	
Investigation of Stimulated Bag-Breakup Processes in Laboratory Modeling of Wind-Wave Interaction	28
Alexander Kandaurov; Daniil Sergeev; Yuliya Troitskaya	
Numerical Simulation of Aeroelastic Effects for an Airfoil with Two Degrees of Freedom	39
Marek Pátý; Jan Halama	
Laser Generated Plasma Followed by Shocks and Increasing Cavitation Bubble in a Mini-Glass Tube	58
Petr Schovanec; Walter Garen; Sandra Koch; Walter Neu; Petra Dančová; Darina Jašíková; Michal Kotek; Václav Kopecký	
Application of Mach-Zehnder Interferometers for Isolator Shock Trains.....	68
Taishi Takeshita; Shinichiro Nakao; Yoshiaki Miyazato	
Flow Control around a Circular Cylinder by a Small Rod	78
Takayuki Tsutsui	

Miscellanea

Efficient Heating and Cooling with Borehole Heat Exchangers	88
Axel Gerschel; Markus Haack; Prasanth Subramani; Lukas Stöckmann; Thomas Schäfer; Tom Walter; Tino Schütte; Jörn Krimmling	
List of Authors	93
Guidelines for Contributors	94
Editorial Board	95

Research Articles

SLOSHING SIMULATION OF A TANK OSCILLATING TOWARDS MULTIPLE DEGREES OF FREEDOM BY PARTICLE METHOD

Shigeyuki Hibi¹; Kazuki Yabushita

National Defense Academy, Department of Mechanical Systems Engineering,
1-10-20 Hashirimizu, Yokosuka, Kanagawa, 239-8686, Japan
e-mail: hibiteru@nda.ac.jp

Abstract

The tank sloshing problem is very important at design time in LNG/LPG ships. This problem causes impulsive loads to ship structures and is often treated as a non-linear one. In order to estimate these impulsive loads, properly many studies have been carried out through both experimental and numerical approaches. Impulsive pressure on the wall of a tank induced by forced multi-degree oscillations is focused in this research. It is shown in the past authors' experiment that forced multi-degree oscillations cause stronger impulsive pressure as compared to individual oscillations. Numerical analysis by a particle method based on finite volume technique is introduced in this study to simulate the above phenomena. The suggested particle method is shown to be useful for simulating a strong nonlinear phenomenon. The authors discuss the calculated results of pressure time history with the experimental results.

Keywords

Sloshing; Impulsive load and pressure; Particle method; Finite volume method.

Introduction

Sloshing is a phenomenon in which a liquid surface fluctuates violently when a tank with a free surface is shaken at a cycle close to the natural period of the tank. Large impulsive loads may be applied to walls of the tank at this time. In LNG/LPG ships sailing through irregular waves, large impulsive pressure may be generated on the wall near ceiling area when liquid cargo collides to walls of a cargo tank. Then it is important to know the fluctuating pressure caused by sloshing when considering the strength of tank as a structural member in ship design.

On the other hand, it is known that a ship navigating through waves has a coupled motion of two degrees of freedom and three degrees of freedom, called longitudinal motion and lateral motion, respectively. For this reason, the hull will fluctuate with a phase difference in some axial direction or rotation direction to those axes. As a result, it is possible that larger sloshing may be caused in tanks inside the ship.

In the previous study [1] an apparatus which can oscillate a tank by force was introduced in order to investigate impulsive pressure on the wall of the tank. This apparatus can oscillate it simultaneously towards 3 degrees of freedom (up-down, left-right and rotation) with each phase differences. Through the experiments it was shown larger impulsive pressure could be excited under oscillating the tank simultaneously towards multiple degrees of freedom than under single direction oscillation and the specific phase differences to appear the largest peak values of pressure was identified.

In this study the authors verified the results of above experiments by numerical simulation. The authors have developed a particle method [2] with finite volume technique in order to

stably simulate a fluid phenomenon with strong nonlinearity such as sloshing. At first static pressure in a tank was verified with the particle method varying the particle number. Next by comparing the time history of pressure with the experiment result of previous study, the effectiveness of the proposed particle method was assured.

1 Numerical Analysis Based on Particle Method with Finite Volume Technique

In particle methods, fluid is modeled as a collection of particles and discretized by considering the interaction between particles without a calculation lattice. Therefore, particle methods are suitable for intense fluid analysis with strong nonlinearity. Here, we explain the outline of the particle method proposed by us with finite volume techniques.

The fundamental equations described by a fluid particle coordinates \hat{r} are represented by the Navier–Stokes equations and the continuous equation.

$$\left. \frac{\partial \mathbf{v}}{\partial t} \right|_{\hat{r}} = -\frac{1}{\rho} \hat{\nabla} p + \mathbf{K} + \nu \hat{\nabla} \cdot \hat{\nabla} \mathbf{v} \quad (1)$$

$$\hat{\nabla} \cdot \hat{\nabla} p = \rho \lim_{\Delta t \rightarrow 0} \frac{\hat{\nabla}(t, \hat{r}) \cdot \mathbf{v}(t - \Delta t, \hat{r} - \Delta \hat{r})}{\Delta t} \quad (2)$$

Here \mathbf{v} is the speed of particles, p is the pressure of particles, ρ is the density of fluid, \mathbf{K} is outer forces and ν is the kinematic coefficient of viscosity of fluid. From Gauss's theorem equations (1) and (2) are transformed into flow equations of integral shape.

$$\left. \frac{\partial \mathbf{v}}{\partial t} \right|_{\hat{r}} = - \lim_{V \rightarrow 0} \frac{1}{\rho V} \int_S p \mathbf{n} dS + \mathbf{K} + \lim_{V \rightarrow 0} \frac{\nu}{V} \int_S \frac{\partial \mathbf{v}}{\partial n} dS \quad (3)$$

$$\lim_{V \rightarrow 0} \frac{1}{V} \int_S \frac{\partial p}{\partial n} dS = \lim_{\substack{\Delta t \rightarrow 0 \\ V \rightarrow 0}} \frac{\rho}{V \Delta t} \int_S \mathbf{v}(t - \Delta t) \cdot \mathbf{n} dS \quad (4)$$

Here \mathbf{n} is the normal vector of a particle and V is the volume of a particle.

Eventually, the discretized equations are derived from equations (3) and (4) in the proposed method.

$$\frac{\mathbf{v}_i - \mathbf{v}_i^{n-1}}{\Delta t} = -\frac{1}{\rho \pi R^2} \sum_{\substack{j=1 \\ i \neq j}}^N \left(P_i + (P_j - P_i) \frac{R}{r_{ij}} \right) \mathbf{n}_{ij} \Delta S_{ij} + \mathbf{K} + \frac{\nu}{\pi R^2} \sum_{\substack{j=1 \\ i \neq j}}^N \frac{\mathbf{v}_j - \mathbf{v}_i}{r_{ij}} \Delta S_{ij} \quad (5)$$

$$\begin{aligned} & \sum_{\substack{j=1 \\ i \neq j}}^N \frac{P_j - P_i}{r_{ij}} \Delta S_{ij} - \frac{P_i}{R} (2\pi R - S_i) \\ &= \frac{\rho}{\Delta t} \left(\sum_{\substack{j=1 \\ i \neq j}}^N \left(\mathbf{v}_i^{n-1} + (\mathbf{v}_j^{n-1} - \mathbf{v}_i^{n-1}) \frac{R}{r_{ij}} \right) \cdot \mathbf{n}_{ij} \Delta S_{ij} - \mathbf{v}_i^{n-1} \cdot \mathbf{S}_i \right) \end{aligned} \quad (6)$$

Here

$$\begin{aligned} \mathbf{r}_i &= (x_i, y_i) \\ \mathbf{r}_{ij} &= \mathbf{r}_j - \mathbf{r}_i \\ r_{ij} &= \sqrt{(x_j - x_i)^2 + (y_j - y_i)^2} \\ \mathbf{n}_{ij} &= \frac{\mathbf{r}_{ij}}{r_{ij}} \end{aligned}$$

$$\begin{aligned}\Delta S_{ij} &= 2\alpha R^2(1 - \cos \theta_{ij}) \\ \alpha &= \frac{2}{\sum_{j=1, j \neq i}^N (1 - \cos \theta_{ij})}\end{aligned}\quad (7)$$

$$\begin{aligned}S_i &= \sum_{j=1, j \neq i}^N n_{ij} \Delta S_{ij}, S_i = \sum_{j=1, j \neq i}^N \Delta S_{ij} \\ K &= (0, -g) \\ \theta_{ij} &= \begin{cases} \cos^{-1} \frac{r_{ij}}{2R} & (r_{ij} < \sqrt{2}R) \\ \sin^{-1} \frac{R}{r_{ij}} & (\sqrt{2}R \leq r_{ij}) \end{cases}\end{aligned}$$

Subscript i means the particle number of interest and subscript j means the neighboring particle number of the particle i . Superscript n indicates the time step number.

r_i means position vector of the i -th particle. The particles are assumed to be spherical (in 2D model just round) and the influence of the neighboring particle j to the particle i is carried out through the micro surface area ΔS_{ij} expressed by equation (7) according to the concept of the Finite Volume Method.

R stands for the radius of a particle and satisfies the following equation.

$$\pi R^2 = D^2 \quad (8)$$

D is the average inter-particle distance and is determined by the spatial resolution of the calculation model. This parameter corresponds to the smoothing length h in the SPH[3].

Considering the efficiency and stability of calculation, it is considered that neighboring particles far from the so called influence radius r_e do not affect. In this study the following value is adopted for the parameter r_e .

$$r_e = 3.1 D \quad (9)$$

The pressure value of particles at each time step is obtained by implicitly solving the equation (6) using the PCGS method. The velocity value of particles is also obtained from the equation (5) implicitly using the PCGS method in case of considering viscosity of fluid and explicitly in case that viscosity is not taken into consideration.

2 Experimental Apparatus and Condition

2.1 Specification of Oscillation Apparatus

The apparatus used in this study can oscillate a tank attached on the bracket harmonically and simultaneously towards 3 degrees of freedom with each phase differences (See Fig. 1 and Table 1).

The size of tank is 400, 400, 100 (mm) (Height, Width, Depth). We define the symbols for the oscillation directions of 3 degrees of freedom as follows in Fig. 2. Heave oscillation (Up – down) stands for Z and Sway oscillation (Left – right) stands for X and Roll oscillation (Rotation) stands for θ .

A pressure sensor is attached on the right side of the tank mounted on the apparatus. The position of the sensor is 40 mm from the bottom. The pressure receiver has round area with diameter of 8mm.

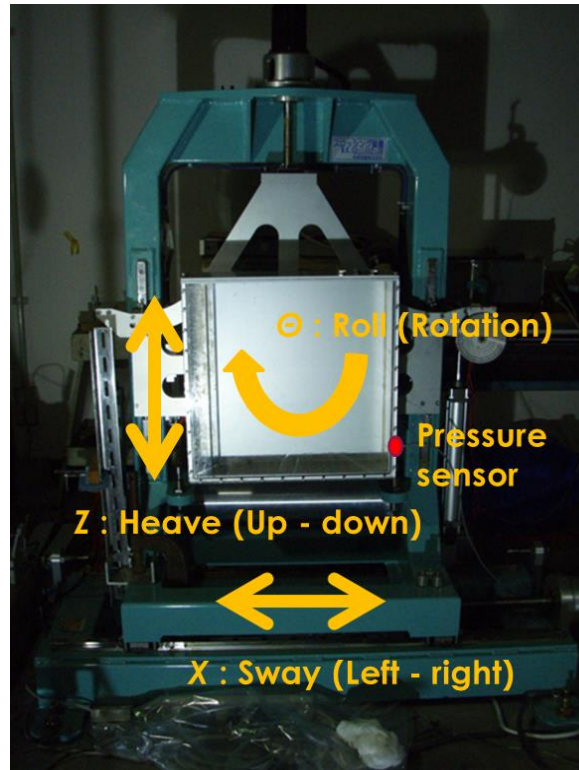


Fig. 1: Oscillation apparatus with 3 degrees of freedom

Tab. 1: Specification of the apparatus about oscillation

Direction of oscillation	Maximum amplitude	Minimum period
Heave (Z) (Up-down)	± 50 mm	1.0 sec.
Sway (X) (Left-right)	± 50 mm	1.0 sec.
Roll (θ) (rotation)	± 45 deg.	1.0 sec.

2.2 Selection of Phase Differences during Simultaneous Oscillation towards 2 Degrees of Freedom

In previous study [1] we chose 3 pairs of 2 degrees of freedom from 3 ones. Those will be subscribed as follows ($\theta - X$, $\theta - Z$, $X - Z$). The oscillation period is uniformly 1.08 sec. which is close to the natural period of the tank in case of the water depth is 60 mm (fixed). The oscillation amplitudes are 15 mm for X and Z and 20 degrees for θ .

We measured time histories of pressure on the wall of the tank repeatedly while changing the phase difference from 0 degree to 360 degrees. We identified the phase difference which cause the largest peak value of pressure for each oscillation pair ($\theta - X$, $\theta - Z$, $X - Z$). The results are shown in Table 2.

Tab. 2: Phase difference which cause the largest peak value

Oscillation pair	Phase difference
$\theta - X$	15 degrees
$\theta - Z$	335 degrees
$X - Z$	220 degrees

3 Numerical Simulation and Discussion

3.1 Comparison of Calculation Accuracy of the Particle Method with Static Pressure

At first we confirm accuracy of the proposed particle method by static pressure. In Fig. 2 a tank model used in the above experiment is shown. Water depth is 60mm as in the experiment. The total particle number is 3,700. The average inter-particle distance D is 38 mm. We define this model of spatial resolution as the base model and name it X1 model. In addition to this model we prepare 3 additional models named $X_{1/2}$ (1,500 particles), X2 (10,500 particles), X4 (33,700 particles) model of which D is half, double and 4 times each other.

Numerical simulation was carried out with the time step of 0.0001 sec. in all cases. Fig. 3 shows the time history of static pressure at the bottom of tank. In all calculation models we can see some fluctuations for the first few seconds in simulation time and after that the pressure values become fairly stable. These fluctuations of pressure occur when relative position of particles turns more stable and closer from the initial particle arrangement in a tetragonal lattice.

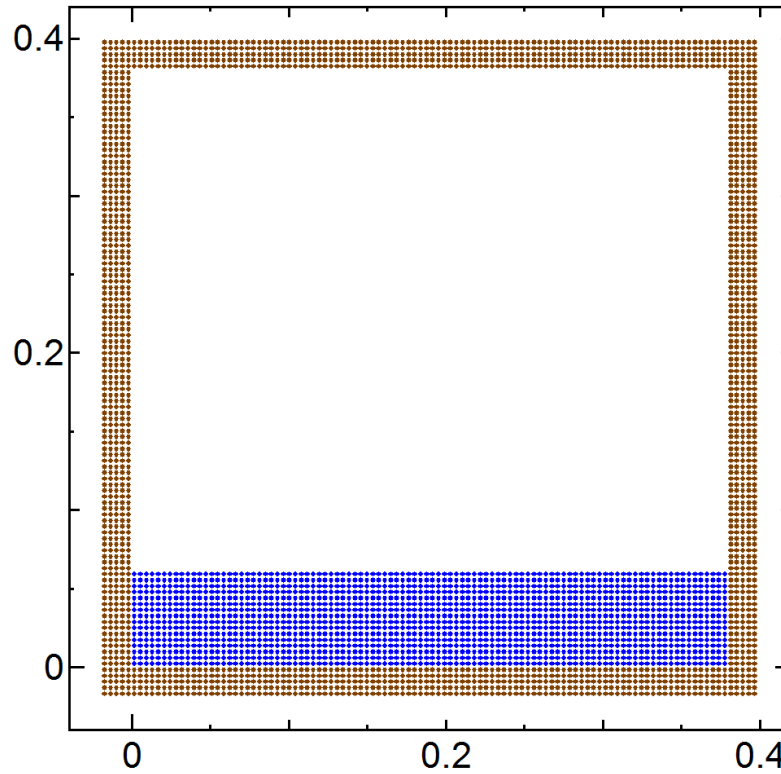


Fig. 2: Initial particle arrangement for static pressure

Table 2 shows Comparison of static pressure with the theoretical value. It can be seen that the calculation accuracy is improved according to the spatial resolution.

Tab. 3: Comparison of static pressure with the theoretical value

	Simulation result (Pa)	Error (%)
X1	616	3.36
X2	610	2.35
X4	607	1.85

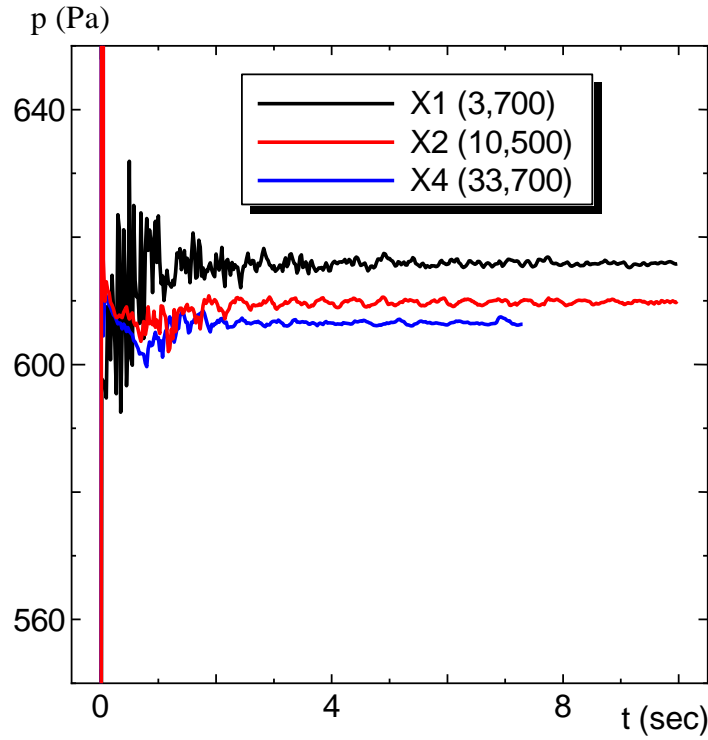


Fig. 3: Time history of static pressure at the bottom of tank

3.2 Numerical Simulation of Forced Oscillation towards 2 Degrees of Freedom

Numerical simulation was carried out under the same conditions as experiment obtained in Section 3.2. Fig. 4 (a) to Fig. 4 (d) show comparison of the experiment and simulation results for time history of pressure value at the position where the pressure sensor is attached. The experimental values are results obtained through a 100Hz low-pass filter and the accuracy of those results are evaluated by a FFT analysis and statistical approaches in the previous paper [1].

From these results, it can be seen that the numerical results have good agreement with the experiment for each models where pressure peaks are observed. But at the time when the pressure sensor is exposed by forced oscillation as shown in Fig. 6 (a) and (b), the pressure values by numerical simulation are 0 in any models, whereas the experiment results show significant values which is not 0. The reason for this is due to viscosity and surface tension in actual water. Even if the pressure sensor is exposed, actually some water is traveling on the wall surface or some water remains on the sensor because of surface tension. However the current proposed particle method does not consider these effects.

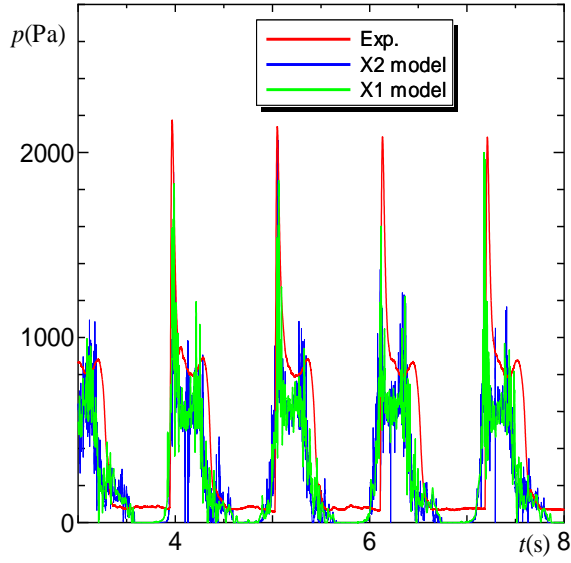


Fig. 4 (a): Time history about $\theta - X$ oscillation.

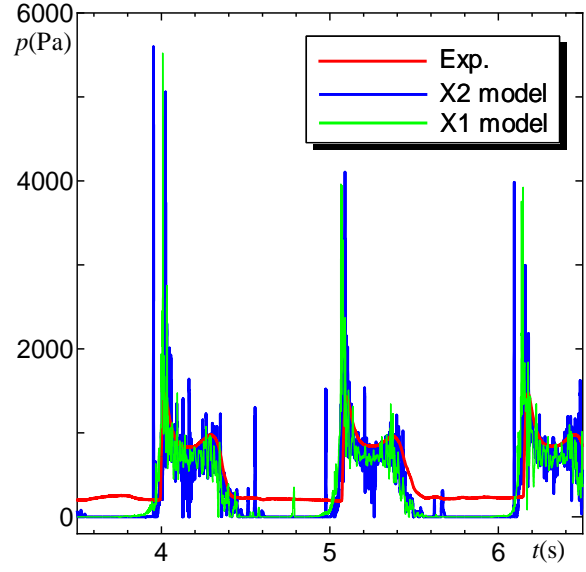


Fig. 4 (b): Time history about $\theta - Z$ oscillation.

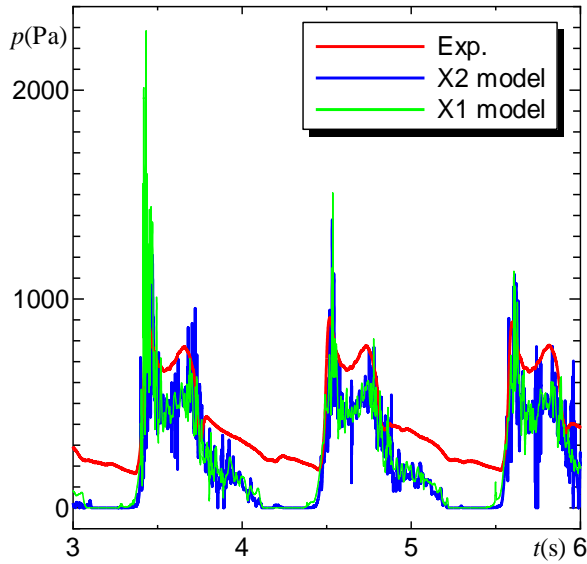


Fig. 4 (c): Time history about $X - Z$ oscillation

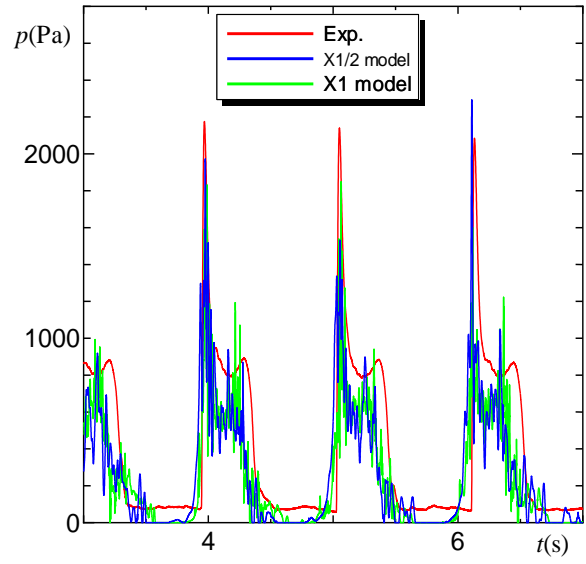


Fig. 4 (d): Time history about $\theta - X$ oscillation.

Although the peak period and peak value shown in Figures are almost reproduced, the simulation results show that the pressure values are evaluated to a smaller value as compared with the experimental values in all models. One reason for this is that relatively low peak values are considered to be difficult to stand due to numerical viscosity. Another reason is believed to be due to the relation between the area of the pressure sensor and the special resolution in the simulation. While the diameter of the pressure sensor is 8 mm, the average inter-particle distance D is 38 mm in the X1 model and 19 mm in the X2 model. Further study will be needed for this problem.



Fig. 5 (a): Moment of exposure of the pressure sensor about $\theta - X$ oscillation.



Fig. 5 (b): Moment of exposure of the pressure sensor about $X - Z$ oscillation.

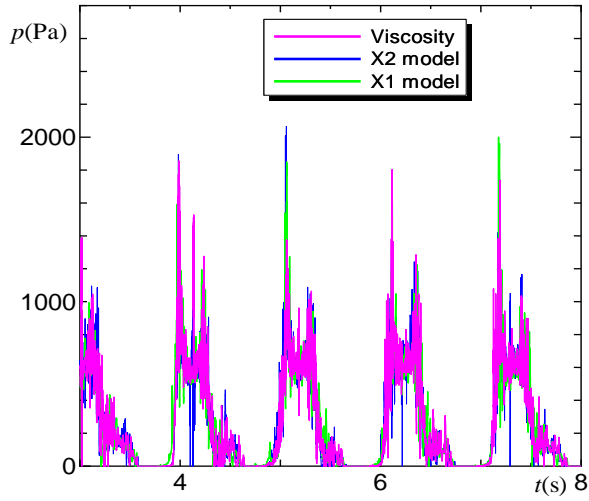


Fig. 6 (a): Time history about $\theta - X$ oscillation.

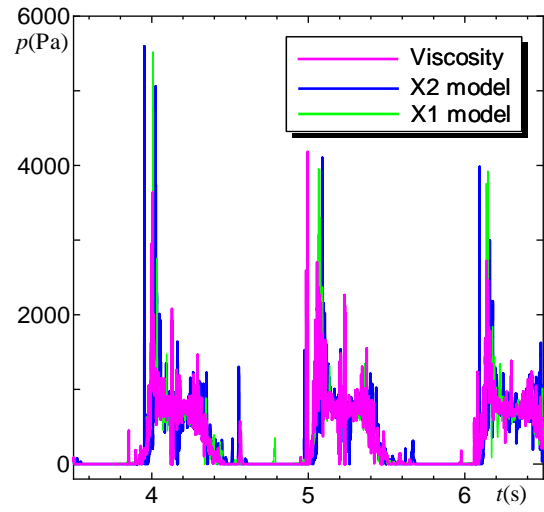


Fig. 6 (b): Time history about $\theta - Z$ oscillation.

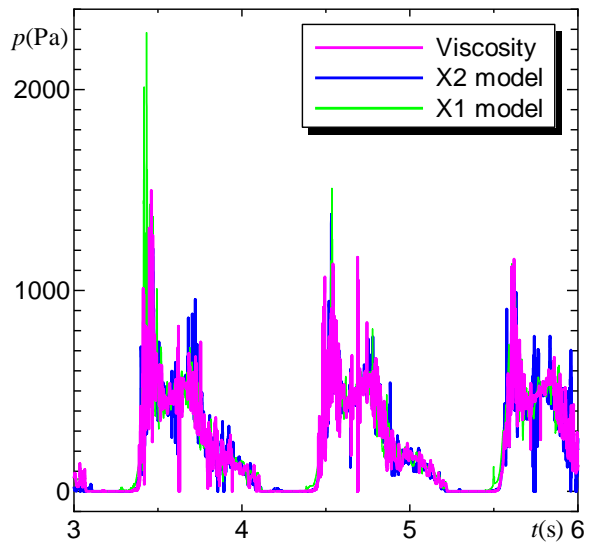


Fig. 6 (c): Time history about $Z - X$ oscillation.

In Fig. 4 (d) the numerical result added for the X1/2 model about $\theta - X$ is shown. Even if the number of particles is just 1,500, it is observed that the accuracy of the analysis is similar. This shows the superiority of the proposed particle method.

Fig. 6 (a) to Fig. 6 (c) show comparison of the experiment and simulation results considering fluid viscosity for time history of pressure value at the position where the pressure sensor is attached.

From these results, it can be seen that there certainly is a tendency that the pressure fluctuation becomes looser, such as peak values but even in the case of considering the influence of the fluid viscosity, there is no big change in the overall pressure fluctuation. This implies that influence of the fluid viscosity is limited in the simulation of intense flows like this study's experiment even though explicitly taking into consideration and the surface tension and wettability by that may be much more important for pressure fluctuation.

Conclusion

In this study the authors carried out numerical simulation of forced oscillation towards 2 degrees of freedom and compared with the previous experimental results. Some considerations were found about it as below.

- Effectiveness of the proposed particle method is shown through the numerical simulation of intense sloshing phenomena.
- In addition to the shape of the pressure sensor, the viscosity of water and the surface tension on the wall of tank are considered to be related to the pressure fluctuation.

Literature

- [1] HIBI, S.: Study on the impulsive pressure of tank oscillating by force towards multiple degrees of freedom. *EPJ Web of Conferences*. 2018, Vol. 180, Paper No. 02034. DOI: [10.1051/epjconf/201818002034](https://doi.org/10.1051/epjconf/201818002034)
- [2] YABUSHITA, K.; HIBI, S: to be posted. *Journal of Marine Science and Technology*.
- [3] MONAGHAN, J. J.: Simulating Free Surface Flows with SPH. *Journal of Computational Physics*. 1994, Vol. 110, Issue 2, pp. 399–406.

SIMULACE ŠPLOUCHÁNÍ NÁDRŽE OSCILUJÍCÍ K VÍCE STUPŇŮM VOLNOSTI METODOU ČÁSTIC

Problém nárazu nádrže je velmi důležitý ve fázi navrhování lodí LNG / LPG. Tento problém způsobuje impulzní zatížení lodních struktur a často je považován za nelineární. Za účelem správného odhadu těchto impulsních zatížení bylo provedeno mnoho studií jak pomocí experimentálních, tak i numerických přístupů. Tento výzkum se soustřeďuje na impulsní tlak na stěnu nádrže vyvolaný nucenými vícecestupňovými oscilacemi. V předchozím experimentu se ukázalo, že nucené vícecestupňové oscilace způsobují silnější impulzivní tlak ve srovnání s jednotlivými oscilacemi. V této studii je popsána numerická analýza metodou částic založená na technice konečných objemů pro simulaci výše uvedených jevů. Navrhovaná metoda částic se zdá být užitečná pro simulaci silného nelineárního jevu. Autoři srovnávají vypočtené výsledky časové historie tlaku s experimentálními výsledky.

SIMULATION DES PLÄTSCHERNS DES TANKS ZU EINER MEHRSTUFIGEN SCHWINGUNG DES SPIELRAUMS MIT DER TEILCHENMETHODE

Das Problem des Anstoßes des Tanks ist in der Phase des Entwurfs von LNG/ LPG-Schiffen sehr wichtig. Dieses Problem verursacht eine impulsartige Belastung der Schiffsstruktur und wird oft als nichtlinear betrachtet. Zum Zweck der richtigen Schätzung dieser impulsartigen Belastungen wurden viele Studien sowohl mit Hilfe von experimentellen als auch numerischen Ansätzen durchgeführt. Diese Untersuchung konzentriert sich auf den Impulsdruck an der Wand des Tanks, welcher durch erzwungene mehrstufige Schwingungen hervorgerufen wurde. Im vorangegangenen Experiment hat sich gezeigt, dass erzwungene mehrstufige Schwingungen einen stärkeren Impulsdruck im Vergleich mit den einzelnen Schwingungen erzeugen. In dieser Studie wird die numerische Analyse der Teilchenmethode beschrieben, welche auf der Technik der endlichen Inhalte für die Simulation der oben angeführten Erscheinungen basiert. Die vorgeschlagene Teilchenmethode scheint für die Simulation einer nichtlinearen Erscheinung nützlich. Die Autoren vergleichen die berechneten Ergebnisse der zeitlichen Historie des Drucks mit den experimentellen Ergebnissen.

SYMULACJA CHŁUPANIA ZBIORNIKA OSCYLUJĄCA DO KILKU STOPNI SWOBODY METODĄ CZĄSTEK

Zagadnienie uderzenia zbiornika jest bardzo ważne na etapie projektowania statków na LNG/LPG. Problem ten powoduje impulsowe obciążenie struktury statku i często uważany jest za nieliniowy. W celu prawidłowego oszacowania tych obciążeń impulsowych przeprowadzono wiele badań opartych na podejściu zarówno doświadczalnym, jak i numerycznym. W niniejszym badaniu skupiono się na ciśnieniu impulsowym działającym na ścianę zbiornika, wywołanym wymuszonymi kilkustopniowymi oscylacjami. Z poprzedniego doświadczenia wynikało, że wymuszone kilkustopniowe oscylacje powodują większe ciśnienie impulsowe w porównaniu z pojedynczymi oscylacjami. W niniejszym opracowaniu opisano analizę numeryczną metodą cząstek opartą na technice skończonej pojemności służącą do symulacji powyżej opisanych zjawisk. Zaproponowana metoda cząstek wydaje się być przydatna do symulowania silnego zjawiska nieliniowego. Autorzy porównują obliczone historyczne wyniki ciśnienia z wynikami przeprowadzonych doświadczeń.

THE EXPERIMENTAL STUDY OF DIFFUSER GEOMETRY FOR LOW PRESSURE EXHAUST CASING OF STEAM TURBINE

Robert Kalista^{1,2}; Lukáš Kanta²; Lev Feldberg³

¹ Doosan Skoda Power, Experimental Research of Flow,
Tylova 1/57, Pilsen, 301 28, Czech Republic

² University of West Bohemia, Department of Power System Engineering,
Univerzitní 8, Pilsen, 306 14, Czech Republic

³ NPO CKTI, Joint-Stock Company, Polzunov Scientific & Development Association on
Research and Design of Power Equipment,
St. Petersburg, Atamanskaya str., 3/6, 191167, Russia
e-mail: ¹robert.kalista@doosan.com

Abstract

The performance of the last stage of the LP part of a steam turbine is strongly influenced by the effectivity of the downstream exhaust casing. The 90° turning of the flow in a relatively short axial distance is a major cause of losses and the design of low-loss diffuser still remains a challenge for mechanical engineers. In this paper, results of studies on a several steam turbine exhaust diffuser designs of SKODA have been reported. Several experimental measurements were carried out in the special sector model air test rig. This unique test rig allows visual observation of the flow by the Schlieren method and evaluating the loss coefficient of static pressure in the diffuser. The test rig allows achieving very high (supersonic) speeds. The range of observed velocities was from 30 to 360 m/s. The experimental data from these measurements are very useful to be able to predict the exhaust casing losses during the real operation of steam turbine in non-designed states. The behaviour of individual diffuser designs has been discussed.

Keywords

Diffuser; Steam turbine; Exhaust casing; Pressure loss.

Introduction

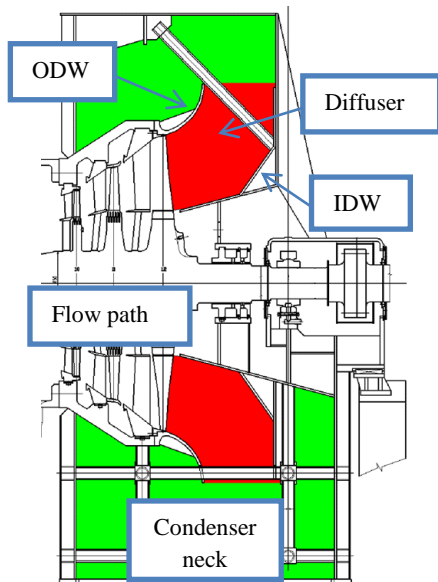
As is well known, the performance of the last stage of the low pressure part of a steam turbine is strongly influenced by the effectivity of the downstream exhaust casing. The efficiency of the exhaust hood depends on many structural factors such as the design of the diffuser parts, dimensions of the outer casing or arrangement of internal supports. The fact that the influences on the last stage output can be quite important is dealt with in e.g. [1] by Hoznedl who provides as an example a 1090 MW turbine in the nuclear power plant with a pressurized water reactor where the increase of pressure loss between the last stage and the condenser by only 2000 Pa can cause output loss of about 4MW for one LP flow.

The low-pressure exhaust casing consisting of the diffuser, the exhaust hood and the condenser neck connects the last stage turbine and the condenser (see Fig. 1). The condenser is located below the turbine level and the steam flow leaving the last stage must change its direction about 90° from the axial direction to the radial direction before exhausting into the condenser. The function of the exhaust hood is to bring the steam into the condenser with minimal energy losses and to transform the output kinetic energy into potential energy. This

mechanism leads to expansion line prolongation between the stage inlet and outlet and to higher turbine power output.

Previous studies and experimental measurements have shown that just the diffuser area has the most significant influence on the total loss of the exhaust casing, for example [2] and [3]. The 90° turning of the flow in a relatively short axial distance is a major cause of losses and the design of low-loss exhaust systems still remains a challenge for mechanical engineers.

With development of CFD methods it is already a common practice to use numeric simulations to analyse and to optimize exhaust hood shapes. A lot of works dealt with this topic in the past, for example [4]. However, the great difficulty of these computations has always been the size and complexity of the computing area. From the point of view of computational and time capacities it is very difficult to fully capture very complex flowing through the entire output tract. For this reason CFD computations are simplified variously and this reduces credibility of results. From the above mentioned and other reasons it is always appropriate to complete CFD computations with relevant experimental measurements and thus to validate obtained results mutually.



ODW – Outer Diffuser Wall; IDW – Inner Diffuser Wall

Fig. 1: Sketch of the axial-radial exhaust casing

1 The Purpose of Experimental Measurement

The aim of this paper is the experimental study of flow in the sector model of low pressure axial-radial diffuser. The observed diffuser was designed by SKODA for an extra-long 54" last stage blade made from titanium. The sector model of the diffuser [7] at optical benches of the laboratory of physical and technical problems of power equipment of NPO CKTI JSC is investigated. This unique test rig allows visual observation of the flow by the Schlieren method and evaluation of the loss coefficient of static pressure in the diffuser. For one geometry of low pressure diffuser a few different variations of inlet velocities were tested. The test rig allows achieving very high (supersonic) speeds. The range of observed velocities was from 30 to 360 m/s. The effect of velocity change was observed. During such similar experiments, it is not usual for such high inlet velocities to be achieved. For this reason, the results obtained are of unique value.

The test facility also has the possibility to blow compressed air into the boundary layer of the ODW (Outer Diffuser Wall). The blown stream of air adds sufficient energy to the boundary

layer, which may delay or prevent its separation from the surface of the diffuser and thus energy losses of the entire output tract should decrease essentially. Much attention to the influence of blowing into the wall of the diffuser together with the influence of the radial leakage of the steam over the bandage of the moving blade was already paid in the past. The air blowing into the boundary layer and simulation of the steam leakage over bandage sealing was not realised in this work. In this paper we concentrate to examine only the sensitivity of velocity on the loss coefficient of the low pressure diffuser.

2 Test Facility

The sketch of diffuser with the main dimensions is shown in Figure 2. The diffuser geometry is described by four basic dimensionless numbers (see Table 1). The sector model of low pressure diffuser is 1:10 scale. The dimensions of the model may differ slightly from the real state, depending on the layout options of the experimental test facility. The following table shows the values of the four basic characteristics for the tested diffuser model.

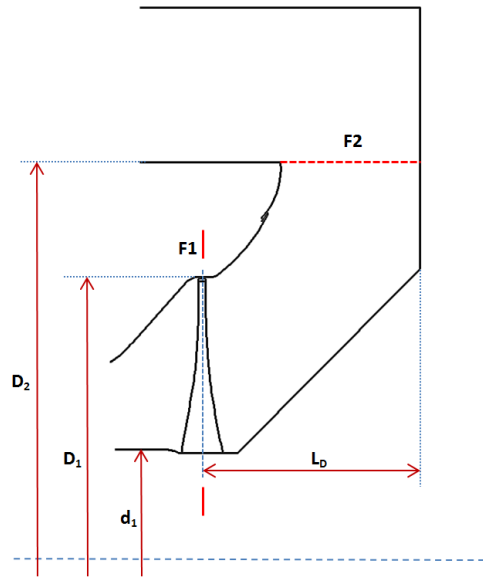


Fig. 2: The sketch of diffuser with characteristics dimensions

Tab. 1: Diffuser geometry

Hub-Tip ratio $d = \frac{d_1}{D_1} = 0.42$	Expansion degree $n = \frac{F_2}{F_1} = 1.50$
Diffuser radiality $D = \frac{D_2}{D_1} = 1.30$	Diffuser elongation $L = \frac{L_p}{D_1} = 0.36$

The illustrative photo of the test facility is shown in Figure 3.



Fig. 3: *Photo of sector model of diffuser (illustrative photo)*

2.1 Advantages and Disadvantages of the Sector Model

The principle of sectorial modelling has a number of advantages. First, it makes it possible to visually observe the flow by using a large arsenal of optical methods. Second, the sector model makes it possible to carry out studies at full-scale flow velocities in a diffuser at lower energy costs. (Air consumption is 10 - 15 times less than in the 3D model of the same scale). Third, this type of construction is much simpler, cheaper, and allows easy variation of the basic geometric parameters of the circular diffuser (elongation, radially, area ratio, internal and external contour configuration) at a constant bushing ratio, which provides mobility in carrying out the experiment.

The studies on the sector model allow significant energy saving (both in terms of the power of the blowers and the duration of the experiments), which becomes particularly important due to a sharp increase in the cost of energy today. In addition, the sector model allows investigation of the effect of inlet conditions (such as radial leakage of the last stage) on the efficiency of the diffuser.

The disadvantages of the sector model in comparison with the 3D model are:

- the complexity of modelling such an important phenomenon as the twist of the flow at the entrance to the diffuser,
- the possibility of studying only an isolated diffuser without an exhaust hood.

In addition, it is important to note that there is some deviation from the geometric similarity in the sector model associated with the technological possibilities. On the other hand, the comparison between the use of a sectional and a full 3D model of the exhaust hood was already tested. No important difference was found using both approaches [6].

3 Description of Measurement

Evaluation of diffuser power performance values assumed for our researches involves flow parameters measurement at inlet and outlet reference cross-sections. Location of pressure measurement points is shown at Fig. 4. The basic element of experimental test rig is the

compressed air source (fan, compressor – different in dependence on the required inlet velocities – pressure ratio). In front of the diffuser model is a stabilisation vessel. A large volume of the stabilisation vessel causes a zero flow velocity (with respect to the Bernoulli equation). Due to the minimum airflow rate in these parts, the stagnation pressure and temperature is measured here.

Design of diffuser model does not allow measurement in the plane corresponding to axis of last stage blades as side walls of the channel in this point are limited with protection glasses. For this reason the inlet reference cross-section (A-A) is located 100 mm upstream of the blade axis. Pressure is measured at nine points from both sides of trapezoidal channel. Measurement points in symmetrical locations on opposite sides are paralleled (seen in Figure 4). Outlet reference cross-section (B-B) is located 200 mm downstream of the outlet edge. Pressure is measured at 20 points distributed at the perimeter from both sides of rectangle channel. Measurement points in symmetrical locations on opposite longer sides are paralleled again. The main flow-rate has been measured by means of an orifice located at the exhaust pipe from the test rig.

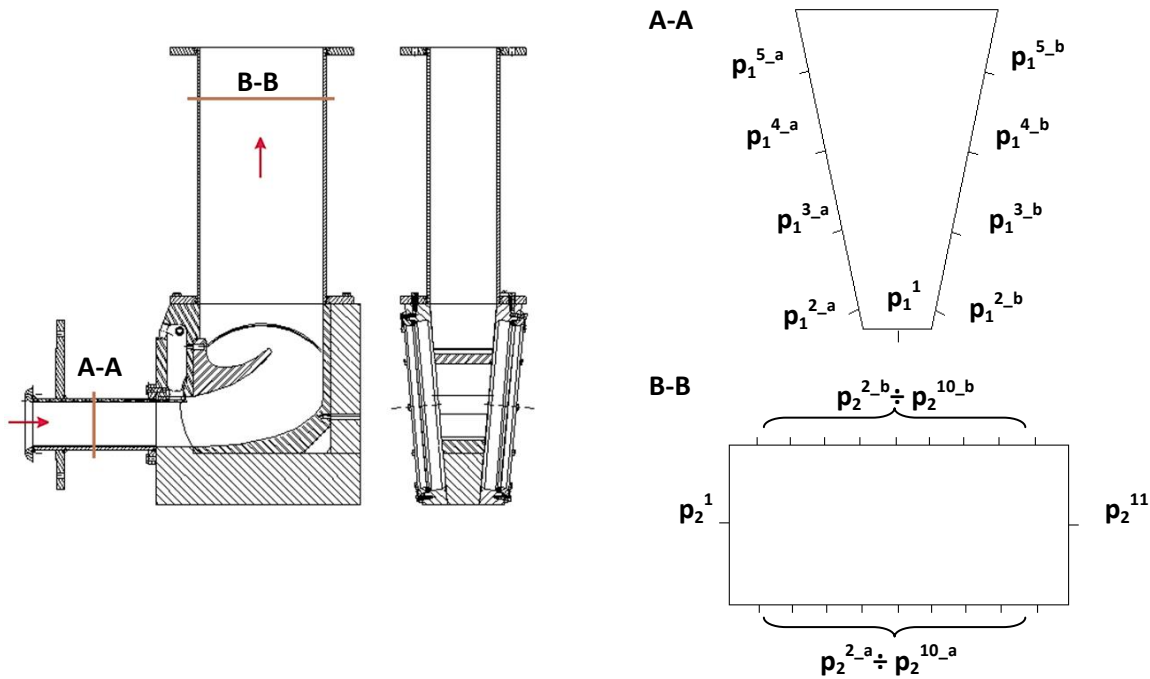


Fig. 4: Sketch of measurement

Figure 4 shows the designation of the individual quantities in the respective measuring planes.

Flow stagnation temperature has been measured with the help of a chromel-cupel thermocouple with analog transducer to voltage. Ambient pressure is measured by a stationary calibrated barometer. The total pressure in the stabilisation vessel is measured by one absolute pressure transducer. All other pressures (static pressures at diffuser inlet/outlet, static pressure before/behind the orifice) are measured by a second pressure transducer of the same type (measurement range $0 \div 0.15$ Mpa). Measurement of individual pressures takes place step by step using a rotary pneumatic switch. The output from the pressure transmitter (4-20 mA) is displayed on the measuring computer.

3.1 Evaluation of Experimental Data

Processing of experiment results was based on results of direct measurement of temperature, static pressure and total pressure at inlet cross-section and static pressure at outlet cross-section (conventionally named “isoentropic” approach).

Diffuser energy characteristics are estimated by total loss coefficient, which was calculated by the following formula

$$\zeta_T = \frac{1 - \left(\frac{\bar{P}_2}{\bar{P}_{01}}\right)^{\frac{k-1}{k}}}{1 - \left(\frac{\bar{P}_1}{\bar{P}_{01}}\right)^{\frac{k-1}{k}}} \quad (1)$$

where

- \bar{P}_{01} – averaged total pressure in inlet control section,
- \bar{P}_1 – averaged pressure in inlet control section
- \bar{P}_2 – averaged pressure in outlet control section

The mean pressure value in the inlet section is determined by numerical integration of the individual pressure values along the trapezoidal channel height, see equation 2 and Figure 5.

$$\bar{P}_1 = \frac{1}{FP1} \sum_{j=1}^{N-2} P_1^j \left\{ \frac{y_{j+1} - y_{j-1}}{2} [a + \operatorname{tg} \alpha \left(\frac{y_{j+1} - y_{j-1}}{2} + y_j \right)] \right\} \quad (2)$$

where:

- FP1 – integration area
- y – height coordinates of static pressure tap
- N – number of static pressure taps
- α – the sector diffuser opening angle

It is important to note the fact that the area FP1 is not equal to F1.

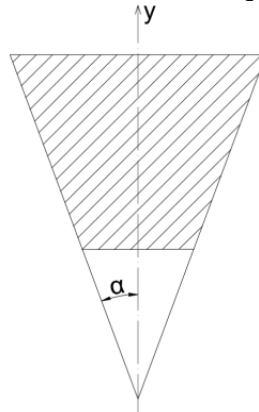


Fig. 5: The inlet control section

The dependence of the total loss coefficient on the inlet isoentropic Mach number was evaluated.

3.2 Flow Visualization – The Optical Method

Flow visualization is essential for exploring and understanding fluid behaviour and can be both qualitative and quantitative. The main methods for visualization of these flows are

optical methods. The three basic principal optical methods are: shadow, Schlieren and interferometry. In this case, the optical Schlieren method was used.

In general, flow field is transparent environment with light refraction index n . The light refraction index in each flow field point is the function of air density in that point, which is function of velocity, pressure and air temperature. The relation between air density and the refraction index is called the Gladstone-Dale equation $n = 1 + K\rho$. The constant K is different for each gas. A light ray, passing through a nonhomogeneous refracted field, is deflected from its original direction and a light path is different from that of an undisturbed ray. The equation (3) shows the dependence of the deflection of light rays on the value of the gradient of the refractive index of the medium, integrated over the thickness of the optical inhomogeneity.

$$\varepsilon(x, y, z) = \frac{1}{n} \int_0^D \frac{\partial}{\partial s} n(x, y, z) dz \quad (3)$$

where:

D – thickness of optical inhomogeneity (width of working area).

4 Obtained Results

All measurements for the examined diffuser were performed under similar conditions over a wide range of inlet velocities from $Ma = 0.15$ to “aerodynamic blockage” ($Ma \sim 1.10$). Reynolds number Re varied from 2.35×10^5 to 4.6×10^6 .

Figure 6 shows the dependence of total energy losses on inlet velocity into diffuser. Up to $Ma = 0.7$ is the negligible dependence of loss on inlet velocity. Slight differences in measured values of total losses do not reach levels of measurement uncertainty. Based on this finding, it can be said that the diffuser losses are independent of inlet velocity until the reaching of $Ma = 0.7$. With a further increase of inlet velocity to the transonic region, the behaviour of losses is difficult to explain. The sharp drop in losses is over with the aerodynamic blockage of the diffuser channel at $Ma = 0.96$ which is accompanied by a sharp increase in losses.

The usual velocity in the diffuser inlet during operation is within the range $Ma = 0.4 \div 0.7$. In some turbine limit states these values may be higher. For the purpose of proper design is very useful to know that in the range of these axial velocities, the total losses of the diffuser are practically unchanged. However, the unchanged value of the diffuser losses, which is higher than 100%, suggests that the shape of the LP diffuser is not optimal for the purely axial character of flow.

Interestingly, similar results were obtained in the previous experimental measurement of several shape variants of the LP diffuser type Skoda mentioned in the report [5]. A sample of the obtained results is shown in Figure 7. These are the results of the measurement for the diffuser 1-3 and 0-4 shape version, which are compared with the results for the basic shape of diffuser (marked: basic variant) for 54 last stage blade, see Figure 7. Even in this case, there was an aerodynamic blockage of the diffuser and a sharp increase in total losses around the area of the sound velocity. It is interesting to find that the basic variant of diffuser achieves the lowest level of total losses even though it was designed for inlet flow with a significant radial component of velocity that is not simulated during the measurement.

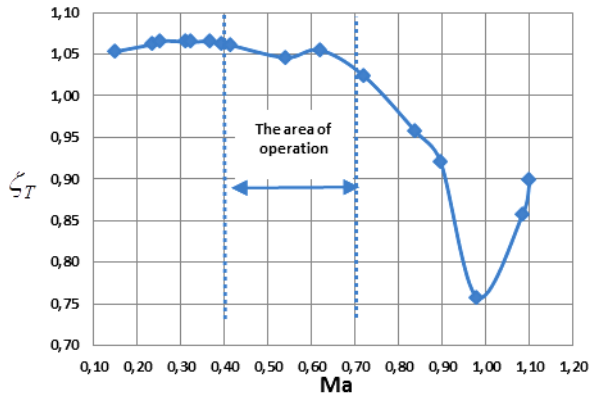


Fig. 6: Dependence of total loss coefficient on the inlet isoentropic Mach number

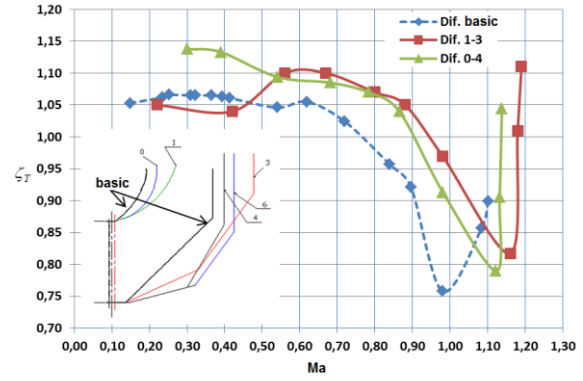


Fig. 7: Comparison of results with previous measurements

The explanation of the obtained results can be partially found in the flow visualization by using the Schlieren method. Figure 8 shows four images for different inlet velocities in the diffuser. The flow direction is, in this case, from left to right. For $Ma = 0.40$ the character of flow corresponds with high loss at level. Flow-rate in diffuser is so small that practically the diffuser effect does not occur. A significant separation of the boundary layer on the ODW is due to the absence of a radial component of velocity and a small flow compression in the IDW region that would help to direct the flow towards the ODW. A significant improvement in diffuser filling is evident with increasing velocity. More visible is also the more significant bending of the flow in the radial direction. The fourth picture captures the occurrence of a series of shock waves in flowing in the transonic region. This corresponds to a significant increase in losses in the diffuser.

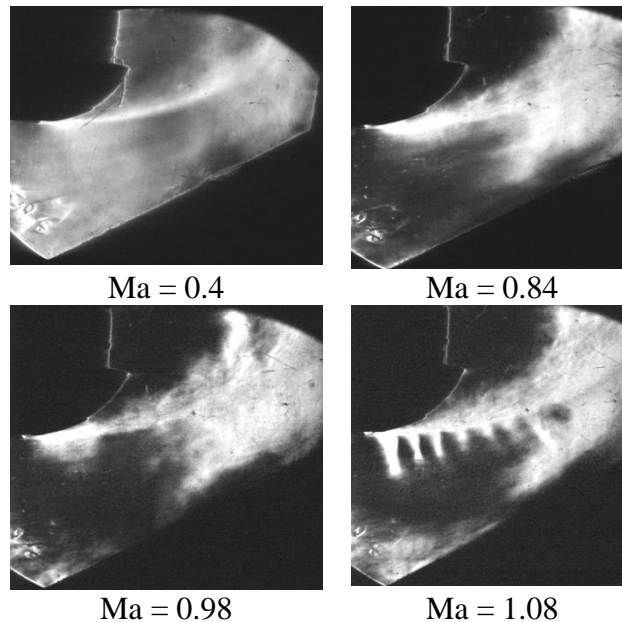


Fig. 8: Visualization of flowing obtained results

Conclusion

Several experimental measurements were carried out at NPO CKTI. The most extensive measurement was concerned with monitoring the loss coefficient of the diffuser for an extra-long 54 last stage blade in dependence on the inlet isoentropic Mach number. Experimental measurements were performed on the sector model of the monitored diffuser. The Schlieren

method was used to visualize the flow. From the obtained results, it is evident that up to $Ma \approx 0.7$ the pressure losses are practically independent of the velocity. This demonstrates the ability of the diffuser to operate over a wide range of inlet flow rates without the significant variable of diffuser losses.

As the inlet velocity increases, the total diffuser losses are sharply decreasing. This phenomenon is manifested up to the area of the transonic velocities, where aerodynamic blockage of the diffuser and formation of the shock waves occurs, resulting in a severe degradation of the diffuser function.

In the next part of the paper, the obtained results are compared with the results from previous years, which were carried out under similar conditions. Unfortunately, compared variants varied more or less from each other and it was not possible to compare the absolute values of the obtained loss coefficients. On the other hand, from the trends of the obtained results, a similar behaviour is visible.

This is a useful finding that demonstrates the correctness and suitability of the experimental methods used.

The individual results presented in this report point to the interesting behaviour of the diffuser, especially for higher inlet velocities. To explain this issue, it is necessary to do more experiments and numerical simulations.

Acknowledgment

This work was realized with financial contribution of TA ČR within the project TJ01000048 – Lowering outlet losses in steam turbines of modern construction.

Nomenclature

F	Area [m ²]
p	Pressure [Pa]
Ma	Mach number [-]
Re	Reynolds number [-]
ζ_T	Total loss coefficient [-]
ODW	Outer diffuser wall
IDW	Inner diffuser wall

Subscripts

0	Total pressure
1	Diffuser inlet
2	Diffuser outlet

Literature

- [1] M. HOZNEDL et al.: The Pressure Field at the Output From a Low Pressure Exhaust Hood and Condenser Neck of the 1090 MW Steam Turbine: Experimental and Numerical Research. In: *Proceedings of ASME Turbo Expo 2018*. Oslo, Norway. 2018, Paper No. GT2018-75248. ISBN 978-0-7918-5117-3. DOI: [10.1115/GT2018-75248](https://doi.org/10.1115/GT2018-75248)
- [2] KALISTA, R.; MRÓZEK, L.; HOZNEDL, M.: The Experimental Investigation of the Internal Support Effects on Exhaust Casing Pressure Recovery. In: *Proceedings of ASME 2017 International Mechanical Engineering Congress and Exposition*. 2017, Paper No. IMECE2017-70279. ISBN 978-0-7918-5841-7. DOI: [10.1115/IMECE2017-70279](https://doi.org/10.1115/IMECE2017-70279)

- [3] HOZNEDL, M.; PACÁK, A.; TAJČ, L.: Effect of internal elements of the steam turbine exhaust hood on losses. *EPJ Web of Conferences*. 2012, Vol. 25, Paper No. 01024. DOI: [10.1051/epjconf/20122501024](https://doi.org/10.1051/epjconf/20122501024)
- [4] FU, Jing-Lun; LIU, Jian-Jun: Investigation of Influential Factors on the Aerodynamic Performance of a Steam Turbine Exhaust System. In: *Proceedings of ASME Turbo Expo 2010*. Glasgow, UK. 2010. Paper No. GT2010-22316. ISBN 978-0-7918-4402-1. eISBN 978-0-7918-3872-3. DOI: [10.1115/GT2010-22316](https://doi.org/10.1115/GT2010-22316)
- [5] ФЕЛЬДБЕРГ, Л. А.: *Аэродинамическое исследование диффузора цнд турбины Шкода на секторной модели. внутренний отчет для SKODA*. Контракт 203/290912/11. 2009.
- [6] TAJČ, L. et al.: The experimental investigation of the influence of the flow swirl and the tip clearance on aerodynamics characteristics of exhaust hoods. In: *Turbomachinery 2007*. Athens, Greece. 2007, pp. 395–404.
- [7] ДОБКЕС, А. П.; НИШНЕВИЧ, В. А.; ФЕЛЬДБЕРГ, Л. А.; ЮШКЕВИЧ, Ю. Э.: *Устройство для исследования газовых потоков оптическими методами*. Авторское свидетельство СССР 811116.

EXPERIMENTÁLNÍ ZKOUŠKA GEOMETRIE DIFUZORU PRO NÍZKOTLAKOVÉ VÝFUKOVÉ PLÁŠTĚ PARNÍ TURBÍNY

Výkon posledního stupně LP části parní turbíny je silně ovlivněn efektivitou spodního výfukového pláště. Otáčení 90° v relativně krátké axiální vzdálenosti je hlavní příčinou ztrát a konstrukce difuzoru s nízkou ztrátou stále zůstává výzvou pro strojní inženýry. V tomto článku byly publikovány výsledky studií několika konstrukcí difuzoru výfukových plynů parodontu ŠKODA. Několik experimentálních měření bylo provedeno ve speciálním sektorovém modelu vzduchotechniky. Toto jedinečné zkušební zařízení umožňuje vizuální pozorování průtoku metodou Schlieren a vyhodnocení ztrátového koeficientu statického tlaku v difuzoru. Testovací zařízení umožňuje dosažení velmi vysokých (nadzvukových) rychlostí. Rozsah pozorovaných rychlostí byl od 30 do 360 m/s. Experimentální data z těchto měření jsou velmi užitečná, aby bylo možné předvídat ztráty výfukových plášťů během reálné činnosti parní turbíny v neupravených stavech. Bylo popsáno chování jednotlivých návrhů difuzoru.

EXPERIMENTALE PRÜFUNG DER DIFFUSERGEOMETRIE FÜR NIEDRIGDRUCKAUSPUFFMÄNTEL DER DAMPFTURBINE

Die Leistung der letzten Stufe des LP-Teils der Dampfturbine wird stark von der Effektivität des unteren Auspuffmantels beeinflusst. Eine Drehung um 90° in relativ kurzer Axialentfernung ist der Hauptgrund der Verluste und die Konstruktion eines Diffusors mit niedrigem Verlust bleibt weiterhin eine Herausforderung für die Maschinenbauingenieure. In diesem Artikel werden die Ergebnisse der Studien einiger Konstruktionen des Diffusors von Auspuffgasen des Parodonts ŠKODA publiziert. Es wurden einige experimentelle Messungen in einem speziellen Sektorenmodell der Lufttechnik durchgeführt. Diese einzigartige Versuchseinrichtung ermöglicht ein visuelles Beobachten der Durchflussmenge mit der Schlieren-Methode und eine Auswertung des Verlustkoeffizienten des statischen Drucks im Diffusor. Die Testeinrichtung ermöglicht das Erreichen sehr hoher Geschwindigkeiten (Überschallgeschwindigkeit). Der Umfang der beobachteten Geschwindigkeiten betrug zwischen 30 und 360 m/s. Die aus dieser Messung hervorgegangenen experimentellen Daten sind sehr nützlich dazu, die Verluste der Auspuffummantelungen während der realen Tätigkeit der Dampfturbine in unregelmäßigen Zuständen voraussagen zu können. Es wird das Verhalten der einzelnen Entwürfe des Diffusors beschrieben.

EKSPERYMENTALNA PRÓBA GEOMETRII DYFUZORA DLA NISKOPRĘŻNYCH OBUDÓW WYLOTOWYCH TURBINY PAROWEJ

Na wydajność ostatniego stopnia niskoprężnej części turbiny parowej w dużym stopniu wpływa skuteczność dolnej obudowy wylotowej. Obroty 90° przy stosunkowo małej odległości osiowej stanowią podstawową przyczynę strat a konstrukcja dyfuzora o niskich stratach pozostaje wciąż wyzwaniem dla inżynierów maszyn. W niniejszym artykule przedstawiono wyniki badań obejmujących kilka konstrukcji dyfuzora wylotowego w turbinach marki ŠKODA. Kilka eksperymentalnych pomiarów przeprowadzono w specjalnym modelu sektorowym systemu wentylacyjnego. To wyjątkowe urządzenie testowe umożliwia wizualną obserwację przepływów przy wykorzystaniu metody Schlierena oraz ocenę współczynnika strat ciśnienia statycznego w dyfuzorze. Urządzenie testowe pozwala na osiągnięcie bardzo dużych (naddźwiękowych) prędkości. Zakres obserwowanych prędkości wynosił od 30 do 360 m/s. Dane eksperymentalne z tych pomiarów są bardzo przydatne do prognozowania strat w obudowach wylotowych w trakcie realnej pracy turbiny parowej także o innej konstrukcji. Opisano także zachowania poszczególnych konstrukcji dyfuzora.

INVESTIGATION OF STIMULATED BAG-BREAKUP PROCESSES IN LABORATORY MODELING OF WIND-WAVE INTERACTION

Alexander Kandaurov¹; Daniil Sergeev²; Yuliya Troitskaya³

Institute of Applied Physics RAS, Geophysical Research Division,

603950 Ulyanova st. 46, Nizhny Novgorod, Russia

e-mail: ¹kandaurov@hydro.appl.sci-nnov.ru; ²sergeev4758@gmail.com;

³yuliya@hydro.appl.sci-nnov.ru

Abstract

The laboratory experiments for identification of mechanisms of the spume droplet's formation in marine atmospheric boundary layer, when strong wind tears off water from the crest of the waves, were carried out at the High-speed wind-wave flume of IAP RAS. The main mechanism responsible for the generation of spume droplets is bag breakup fragmentation of small-scale disturbances that arise at the air–water interface under the strong wind. This work concentrates on investigation of a separate bag-breakup event that was forced to occur in a dried high-speed wind-wave flume. The details of the bag-breakup fragmentation were investigated qualitatively and quantitatively using synchronized multiperspective high-speed video recording in shadowgraph configuration.

Keywords

Wind-wave interaction; Atmospheric boundary layer; Wind-wave flume; Sea spray; Bag-breakup; High-speed video; Particle tracking velocimetry.

Introduction

Sea sprays are typical element of the marine atmospheric boundary layer and important environmental effect. Difficulties of direct measurements in hurricane conditions and insufficient knowledge about the mechanisms of the spume droplet's formation are the main reasons for insufficient knowledge on the sea spray generation function, which characterizes the size distribution of droplets injected from a unit of surface in a unit of time, leading to significant uncertainties in estimations of sea sprays influence on the marine atmospheric boundary layer [1-6]. For example, the empirical function of spray generation may differ by six orders of magnitude based on different observation reports (see a review of experimental data in [7]). Even the spray-generation mechanisms in extreme winds remained undetermined [4, 7].

The laboratory experiments for identification of these mechanisms, when strong wind tears off water from the crest of the waves, were carried out at the High-speed wind-wave flume of IAP RAS. As previous studies showed based on statistical analysis of number of these phenomena at different winds, the main mechanism responsible for the generation of spume droplets is bag-breakup fragmentation of small-scale disturbances that arise at the air–water interface under the strong wind [8]. This regime is characterized by inflating and consequent bursting of the short-lived objects, bags. It begins with increase of small-scale elevation of the surface, transforming to small “sails” then inflated to a water film bordered by a thicker rim and at last blows up, so the droplets are produced from rupture of the water film and fragmentation of the rim.

One of the most important problems, we are trying to solve, is to construct the spray generation function as the basis for calculating the contribution of spray to exchange processes at the air-sea interface. In our previous work [8], the statistics on bag-breakup events have already been found as a result of processing high-speed recordings of the water surface at high winds in flume. To build the spray generation function, we need to know in addition what droplets are formed during one bag-breakup fragmentation. Then the spray generation function can be found as convolution of the of “bag” generation function and of the distribution function of droplets from one “bag-breakup”. In this model experiment, we develop methods for obtaining this distribution for a single “bag”. The spontaneous characterization of their occurrence on the water surface complicated detailed studies, and in this work we study the separate bag-breakup event that was forced to occur in a dried high-speed wind-wave flume.

The first part of the article is devoted to the description of the methodology of experiments at high-speed wind-wave flume. The second part describes how high-speed video recordings of “bags” were processed to obtain spray characteristics. The work is summarized in conclusion.

1 Experiment and Measurements

1.1 High-Speed Wind-Wave Flume

The experiments were performed in the High-speed wind-wave flume located on top of the Large Thermostratified Tank (LTST) of the Institute of Applied Physics (IAP RAS). The centrifugal fan equipped with an electronic frequency converter to control the discharge rate of the airflow produced the airflow in the flume with the straight working part of 10 m. The operating cross section of the airflow is $0.4 \times 0.4 \text{ m}^2$. During the experiments axis velocity in the flume varied from 10 to 17 m/s. More details of the facility construction and parameters of air flow and surface waves are described in [9]. As this work concentrates on generation and investigations of a separate bag-breakup event, the flume was closed at its bottom with rigid plates at the water level used in previous experiments [8] and bag-breakup event was forced to occur at a small reservoir installed at a distance of 7.5 m from the beginning of the working section. The measured value of the surface tension was $\sigma = (7.0 \times 0.15) \cdot 10^{-2} \text{ N/m}$. The principal scheme of the experimental setup is shown in Fig. 1.

Legend

- 1 - LED lights,
- 2 - solid flat bottom,
- 3 - opaque screen,
- 4 - high-speed wind-wave flume,
- 5 - top high-speed camera,
- 6 - bag-breakup,
- 7 - side semi-submerged box,
- 8 - side high-speed camera,
- 9 - nozzle,
- 10 - reservoir with water,
- 11 - foam rubber in water,
- 12 - nylon mesh.

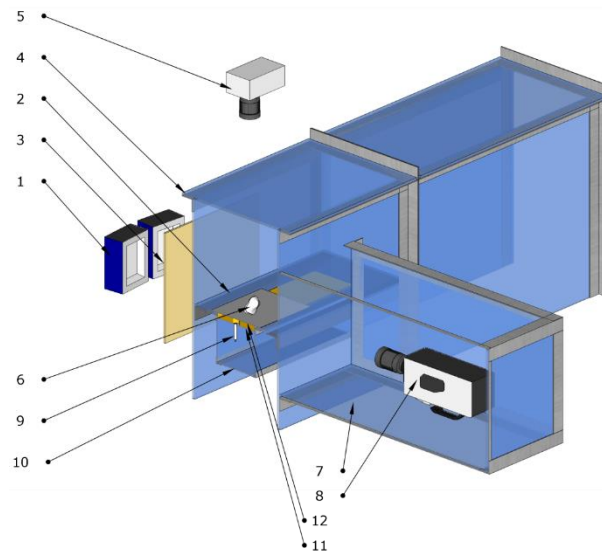


Fig. 1: The cross-section of the high-speed wind-wave flume

1.2 Initial Disturbance

Initial disturbance from which the bag breakup developed was artificially created at the desired position using the underwater jet from a submerged nozzle. The nozzle was placed in vertical orientation 15 cm under water surface. It is assembled of 5 nickel tubes 20×2 mm, lined up in a row in cross-wind direction. Water entered the nozzle at a pressure of 3 bar via an electronically controlled valve that was opened for a period of 20 ms. Driving signal for the valve was combined with triggers of both cameras in synchronization system, controlled via microcontroller.

In order to damp the disturbances that arise on the surface of the water a sheet of 20 mm thick foam rubber with a hole 30 mm in diameter was placed above the nozzle. It was additionally covered with a nylon net with cell size 2 mm. The aim was to inject about 2.5 ml of water in 20 ms with good repeatability. The dependence of the shape of the initial disturbance on time was investigated using image processing of frames from the side camera captured without wind. Comparison of successive initial disturbances showed the stability of their shape within 10% for height and diameter.

1.3 Wind Flow Parameters

The wind flow parameters were measured by the profile method at a distance of 7.5 m from the beginning of the flume. Wind velocity profiles were measured by the L-shaped Pitot tube with the differential pressure transducer Baratron MKS 226A with the accuracy of 0.5% of full scale range, i.e., 3 cm/s. The tube was mounted on the scanning device. The lower level of scanning located at a distance of 1 cm from the surface, while the upper layer was 20 cm. The scanning method with the slow continuous vertical movement of 1.1 mm/s was used. The results were binned into 100 equidistant levels. For each fixed wind parameters, at least five profiles were measured for subsequent averaging. This technique allowed obtaining wind speed profiles in logarithmic boundary layer and calculate the friction velocity and equivalent speed at a standard meteorological height of 10 m. The scaling parameter for the air turbulent boundary layer flow above the water surface is the friction velocity, u_* , defined via vertical turbulent shear stress: $F_M = \rho_{\text{air}} u_*^2$, where ρ_{air} is the air density. Experiments were performed for 10 to 17 m/s centerline wind speeds, the friction velocity, u_* , varied between 0.46 and 0.73 m/s; the equivalent wind speeds at the reference height 10m U_{10} between 16 and 26 m/s (this corresponds to Beaufort number up to 10 in field conditions [10]).

Tab. 1: Air-side logarithmic boundary layer parameters for different fan rotation frequencies F .

F (Hz)	u_* (m/s)	U_{10} (m/s)
30	0.47	16.4
35	0.52	18.8
40	0.61	21.8
45	0.69	24.5
50	0.73	26.6

1.4 High-Speed Video Recording Setup

The details of the bag-breakup fragmentation were investigated qualitatively and quantitatively using high-speed video recording. Synchronized multiperspective high-speed recordings were captured in shadowgraph configuration: vertical opaque screen behind the scene was illuminated from behind with intensive light source.

The main shadowgraph recording was carried out horizontally with high-resolution NAC Memrecam HX-3 high-speed digital video camera with Zeiss 100mm f/2.0 Makro Classic lens (f/22 aperture was used). Two 100W LED light sources were used as a backlight, and a white opaque screen was located on the opposite from the camera side of the flume. The camera is located at a distance of 60 cm from the bag-breakup area ($63 \mu\text{m}/\text{px}$ scale) so that the optical axis lies in the plane of the water surface. The shooting speed was 3990 fps, the shutter speed was $1/50000$ s, the image size was 2560×960 pixels (161×60 mm).

Additional shooting was done from above with the Optronis CamRecord CR3000x2 camera with Samyang 85mm f/1.4 lens. The camera was located at a distance of 112 cm from the surface (scale $102 \mu\text{m}/\text{px}$). The shooting speed was 1250 fps, the shutter speed was $1/5000$ s, the image size was 1696×720 pixels (173×74 mm).

We used the same LED light source for side and top shooting, so only side shooting was made in shadowgraph setup. The side view was used to obtain detailed data on the dynamics of the resulting structures: the shape of the structure before and during bag-breakup, the speed and size of the droplets formed. Top view was only used to control the shape of the structure in the transverse direction.

Records were made for 5 different wind speeds with fan rotation frequencies of 30, 35, 40, 45 and 50 Hz (centerline wind speed $10 \div 17$ m/s). For each wind speed, 9 to 17 records of the bag-breakup were captured. Each recording from the side camera consists of $250 \div 700$ frames ($63 \div 175$ ms). Before and after each recording, control measurements of the shape and size of the initial disturbance were made without wind.

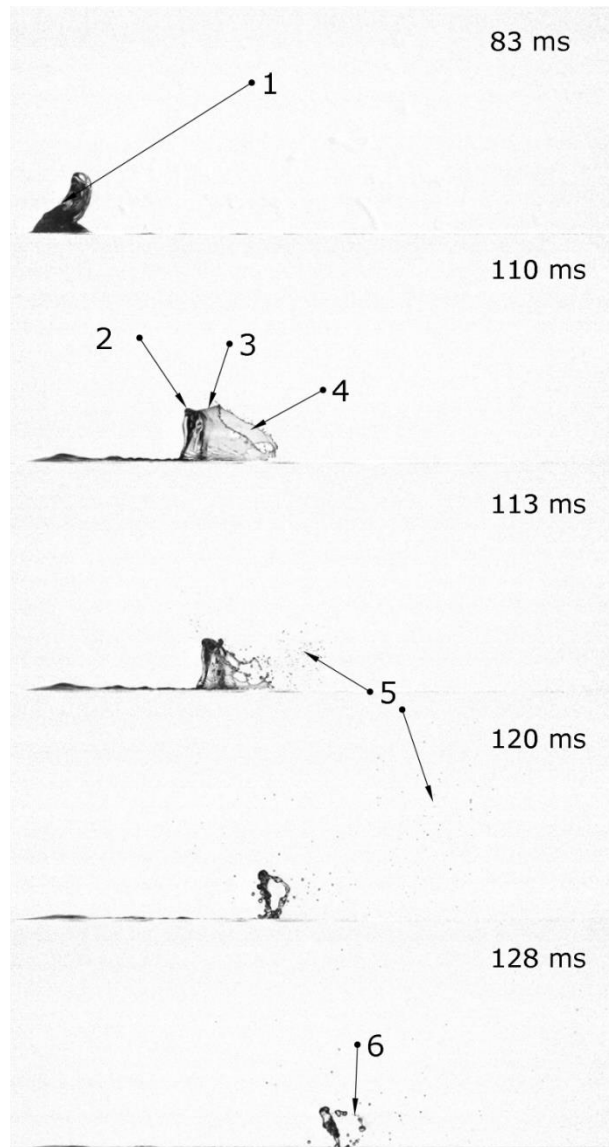


Fig. 2: Example of images obtained from the side camera (time points 83, 110, 113 and 120 ms) for wind speed $U_{10} = 21.8$ m/s. 1 - initial disturbance, 2 - rim, 3 - film, 4 - film rupture, 5 - film drops, 6 - rim drops. Full image width 161 mm.

2 Image Processing

A study of the obtained video records showed that the generation of spray during the individual bag-breakup was due to two processes: 1) rupture of the film, which leads to the formation of small droplets; 2) fragmentation of the “rim” remaining after the rupture of the liquid film, at which large drops are generated (see Fig. 2).

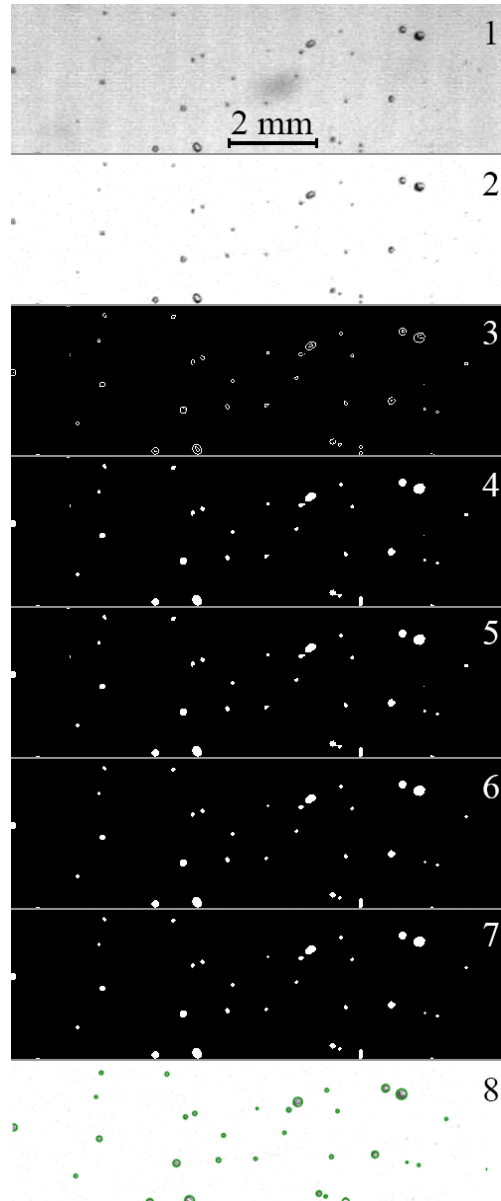


Fig. 3: Image processing sequence for a fragment of frame ($U_{10} = 21.8$ m/s, 113 ms after film puncture, 81 mm downwind the initial disturbance, 33 mm above surface), Green circles - detected droplets

Special software was developed for the processing of side video recordings. It enabled us obtaining detailed data on the dynamics of the resultant structures, such as the shape of the structure at different stages of the rupture, the speed and size of the droplets formed. It utilizes homebrew implementations of feature detection, Particle image velocimetry and particle tracking methods for droplet tacking.

2.1 Droplet Detection

At the first stage of droplet trajectories retrieving, an special algorithm was developed, which allows finding the position of all visible droplets on each frame of the record. The image processing sequence is shown in Fig. 3. for a fragment of one frame. This sequence is an evolution of an algorithm previously developed for water surface detection in laser measurements, that is described in details in [11]. First the background is subtracted from initial frame (1, 2); edge detection is performed with Sobel operator (3), morphological closing with 3-pixel disk element (4) and subsequent filling of closed areas (5) results in

binary image of large droplets; noise is suppressed with morphological opening with 1-pixel disk element (6); to preserve small droplets logical ‘or’ is performed with binarized by threshold initial image (7); positions and sizes of all isolated regions are calculated (8). Larger areas are rejected with their closes neighbors as part of the initial disturbance or “rim”. As a result we get position and size of every droplet and some false detections on every frame of side view records (Fig. 4). For images captured with current side view setup this algorithm can only detect droplets larger than 100 μm , but same algorithm can be used for smaller droplets using video with higher resolution.

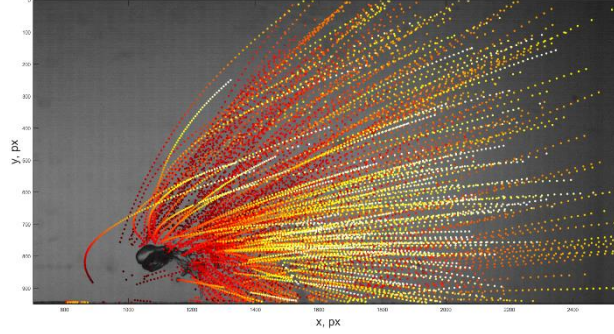


Fig. 4: Position of all droplets found on all frames in one record ($U_{10} = 21.8 \text{ m/s}$); color represents frame number. 6.2 ms after film puncture. Full image width 117 mm.

2.2 Droplet Velocity Estimates

In order to facilitate the tracking of droplets, the velocities of droplets were estimated by Particle image velocimetry method (PIV). This was possible due to the fact that most droplets in particular area of image have similar velocities. PIV processing of the images was performed by specially developed software similar to our previous studies of air velocities in marine boundary layer [12]. Successive frames were compared, interrogation window size 128×128 pixels with 50% overlapping, only one iteration is used, with tree-point interpolation for CCF maximum. Velocity fields were filtered using maximum and minimum velocity thresholds, then with 2-dimentional median filtering and then were interpolated to position of every droplet of the frame (Fig. 5).

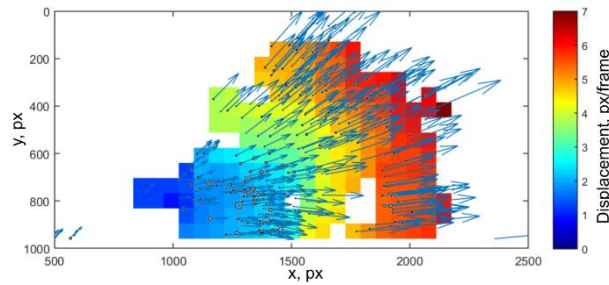


Fig. 5: Approximate velocity field obtained by PIV for equivalent wind speed $U_{10} = 21.8 \text{ m/s}$. The color represents velocity field, arrows - interpolation to position of each droplet (shown in circles).

2.3 Droplet Tracking

In order to retrieve droplet trajectories special tacking algorithm was developed. As droplet density decreases over time we run tacking backward in time: it is easier to separate trajectories if we start with lower density. Starting from the end of the record for every droplet on frame we try to find appropriate droplet on previous frame in the vicinity of its assumed position.

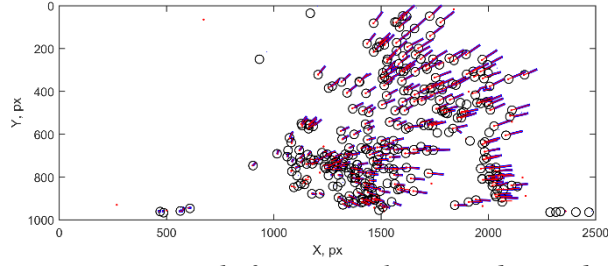


Fig. 6: Example of a trajectory search for equivalent wind speed $U_{10} = 21.8$ m/s. Circles shows the search area near the assumed position. Blue lines are the previous 4 points of each trajectory. Red dots positions of all droplets on the frame.

We used two methods for calculation of assumed position: 1) based on interpolated PIV velocity field; 2) based on parabolic extrapolation for coordinated of four previously found points of current trajectory assuming a constant acceleration. A combination of these two methods is used: the first method is used for trajectories containing less than 4 known points, the average with weights between two methods is used otherwise. Trajectory data, the last found point of which is not more than three frames from a given one, is used for each frame. Thus, if a drop has not been detected on one or two consecutive frames, the trajectory will still be constructed. The trajectory search stops when there are no droplets found in the vicinity of 20 pixels from the expected position or the radius of the droplet found is more than 3 times different from the current one. If two trajectories find the same drop, the latter is assigned to the trajectory, the distance to the supposed point of which is smaller. The use of four points for polynomial extrapolation allows taking into account the scatter of the calculated coordinates. If it is too large, then the last found point of the trajectory is neglected. The example of droplet tracking is shown on Fig. 6.

Some of trajectories are rejected as false detection. Motionless trajectories (with median displacement less than 0.001 pixels per frame) and trajectories shorter than 10 frames are rejected as noise. This algorithm can result in trajectories that are non-overlapping parts of a single real trajectory (in the case when tracking loses a droplet and then finds it and starts a new trajectory). In order to combine such trajectories into one, for each non-intersecting in time pair of trajectories, the standard deviation of the found positions and the polynomial extrapolation was calculated. In case of a deviation below the threshold, the trajectories were combined into one. The described algorithm can be performed in several iterations: On each iteration assigned to trajectories droplet detections are excluded. This algorithm enables assigning more than 75% of droplets found to trajectories for most part for the experimental condition (and significant part missed droplets are false detected ones) and getting more than 500 separate trajectories for some of the records. The example of retrieved trajectories is shown in Fig. 7.

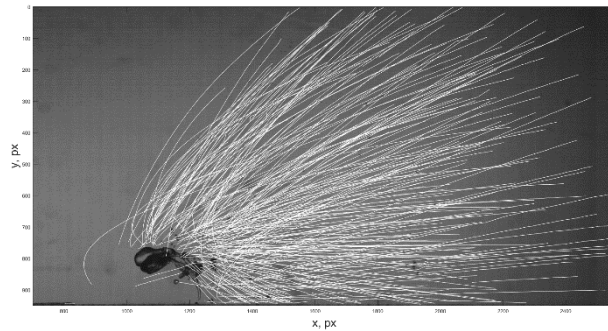


Fig. 7: All trajectories (white) found in one record ($U_{10} = 21.8$ m/s). Example frame is 6.2 ms after film puncture. Full image width 117 mm.

Conclusion

A special system that allows modeling under controlled conditions a single event of bag-breakup fragmentation, which is the dominant process of spray generation during wind-wave interaction, was developed. We used the approach of forced generation of the separate bag-breakup event in a dried high-speed wind-wave flume with water reservoir installed under the working section.

To obtain information on the characteristics of the spray, high-speed shooting in shadowgraph configuration was used and special software was developed to identify the droplets on the images and track their trajectories based on the combination of PIV and reversed in time particle tracking, utilizing the fact of reducing density of droplets in the image over time starting from the moment of fragmentation. The data obtained by this method in combination with the statistics of the occurrence of "bags" will be used to construct the empirical function of spray generation.

Acknowledgments

Carrying out experiments themselves was supported by Russian Science Foundation (Agreement No. 14-17-00667); designing of methods of measurements including: optical and visualization scheme, methods of measurements of the air flow and wave field parameters were supported by Russian Foundation of Basic Research (No 18-77-00074); the development of the software for video processing was supported by the Grant of the President No. MK-2041.2017.5.

Literature

- [1] ANDREAS, E. L.; EMANUEL, K. A.: Effects of Sea Spray on Tropical Cyclone Intensity. *Journal of the Atmospheric Sciences*. 2001, Vol. 58, pp. 3741–3751. DOI: [10.1175/1520-0469\(2001\)058<3741:EOSSOT>2.0.CO;2](https://doi.org/10.1175/1520-0469(2001)058<3741:EOSSOT>2.0.CO;2)
- [2] ANDREAS, E. L.: Fallacies of the Enthalpy Transfer Coefficient over the Ocean in High Winds. *Journal of the Atmospheric Sciences*. 2011, Vol. 68, pp. 1435–1445. DOI: [10.1175/2011JAS3714.1](https://doi.org/10.1175/2011JAS3714.1)
- [3] BAO, J.-W.; FAIRALL, C. W.; MICHELSON, S. A.; BIANCO, L.: Parameterizations of Sea-Spray Impact on the Air–Sea Momentum and Heat Fluxes. *Monthly Weather Review*. 2011, Vol. 139, pp. 3781–3797. DOI: [10.1175/MWR-D-11-00007.1](https://doi.org/10.1175/MWR-D-11-00007.1)
- [4] SOLOVIEV, A. V.; LUKAS, R.; DONELAN, M. A.; HAUS, B. K.; GINIS, I.: The air-sea interface and surface stress under tropical cyclones. *Scientific Reports*. 2014, Vol. 4, Article No. 5306. DOI: [10.1038/srep05306](https://doi.org/10.1038/srep05306)
- [5] TAKAGAKI, N. et al.: Strong correlation between the drag coefficient and the shape of the wind sea spectrum over a broad range of wind speeds. *Geophysical Research Letters*. 2012, Vol. 39, Issue 23. DOI: [10.1029/2012GL053988](https://doi.org/10.1029/2012GL053988)
- [6] TAKAGAKI, N.; KOMORI, S.; SUZUKI, N.; IWANO, K.; KUROSE, R.: Mechanism of drag coefficient saturation at strong wind speeds. *Geophysical Research Letters*. 2016, Vol. 43, Issue 18, pp. 9829–9835. DOI: [10.1002/2016GL070666](https://doi.org/10.1002/2016GL070666)
- [7] ANDREAS, E. L.: A review of spray generation function for the open ocean in Atmosphere. In: Perrie, W. (ed.), *Ocean Interactions Volume 1*. 2002, pp. 1–46.
- [8] TROITSKAYA, Y. et al.: Bag-breakup fragmentation as the dominant mechanism of sea-spray production in high winds. *Scientific Reports*. 2017, Vol. 7, Article No. 1614. DOI: [10.1038/s41598-017-01673-9](https://doi.org/10.1038/s41598-017-01673-9)

- [9] TROITSKAYA, Y. I. et al.: Laboratory and theoretical modeling of air-sea momentum transfer under severe wind conditions. *Journal of Geophysical Research: Oceans*. 2012, Vol. 117, Issue C11. DOI: [10.1029/2011JC007778](https://doi.org/10.1029/2011JC007778)
- [10] NATIONAL METEOROLOGICAL LIBRARY in conjunction with the MET OFFICE'S NATIONAL CLIMATE INFORMATION CENTRE: *National Meteorological Library and Archive Fact sheet 6 — The Beaufort Scale*. [online]. 2010. Available from WWW: http://www.metoffice.gov.uk/binaries/content/assets/mohippo/pdf/s/j/10_0425_factsheet_6_beaufort.pdf
- [11] SERGEEV, D. A.; KANDAUROV, A. A.; VDOVIN, M. I.; TROITSKAYA, Y. I.: Studying of the surface roughness properties by visualization methods within laboratory modeling of the atmospheric-ocean interaction, *Sci Vis*. 2015, Vol. 7, Issue 5, p. 109.
- [12] KANDAUROV, A. A.; TROITSKAYA, Y. I.; SERGEEV, D. A.; VDOVIN, M. I.; BAIDAKOV, G. A.: Average velocity field of the air flow over the water surface in a laboratory modeling of storm and hurricane conditions in the ocean. *Izvestiya, Atmospheric and Oceanic Physics*. 2014, Vol. 50, Issue 4, pp 399–410. DOI: [10.1134/S000143381404015X](https://doi.org/10.1134/S000143381404015X)

ZKOUMÁNÍ STIMULOVANÝCH PROCESŮ ROZTRŽENÍ VAKU V LABORATORNÍM MODELU INTERAKCÍ VLN ZPŮSOBENÝCH VĚTREM

Laboratorní experiment pro identifikaci mechanismů tvorby kapiček pěny v mořské atmosférické hraniční vrstvě, kdy silný vítr odtrhne vodu z hřebene vln, byl prováděn na vysokorychlostním vlně IAP RAS. Hlavním mechanismem, který je odpovědný za tvorbu kapiček pěny, je fragmentace roztrženého vaku a drobné poruchy, které vznikají na rozhraní vzduch-voda pod silným větrem. Tato práce se soustřeďuje na zkoumání jednotlivých případů roztržení vaků, ke kterým došlo v suchém vysokorychlostním větru. Podrobnosti fragmentace roztržení vaků byly zkoumány kvalitativně a kvantitativně pomocí synchronizovaného multiperspektivního vysokorychlostního záznamu videa v radiografické konfiguraci.

DIE ERFORSCHUNG DER STIMULIERTEN PROZESSE DES REIßENS DES SACKS IM LABORMODELL DER INTERAKTIONEN VON WINDERZEUGTEN WELLEN

Das Laborexperiment zur Identifizierung der Mechanismen der Bildung von Schaumtropfen in der Grenzschicht zwischen Meer und Atmosphäre, wobei starker Wind das Wasser von den Wellenkämmen losreißt, wurde im Hochgeschwindigkeitswind der Welle IAP-RAS-Welle durchgeführt. Der Hauptmechanismus, welcher für die Bildung von Schaumtropfen verantwortlich ist, besteht in der Fragmentierung des gerissenen Sacks und in kleinen Störungen, welche an der Luft-Wasser-Grenze unter starkem Wind entstehen. Diese Arbeit konzentriert sich auf die Erforschung der einzelnen Fälle des Reißens der Säcke, zu welchem es in trockenem Hochgeschwindigkeitswind kam. Die Details der Fragmentierung des Reißens der Säcke wurden qualitativ und quantitativ mit Hilfe einer synchronisierten multiperspektiven Hochgeschwindigkeitsaufnahme des Videos in radiografischer Konfiguration untersucht.

BADANIE STYMULOWANYCH PROCESÓW BAG-BREAKUP W LABORATORYJNYM MODELU INTERAKCJI FAL WYWOŁANYCH WIATREM

Doświadczenie laboratoryjne mające na celu zidentyfikowanie mechanizmów powstawania kropli piany w atmosferycznej warstwie granicznej nad morzem, gdy silny wiatr odrywa wodę z grzbietu fal, przeprowadzano w kanale falowo-wiatrowym o szybkim przepływie IAP RAS. Głównym mechanizmem odpowiedzialnym za powstawanie kropli piany jest fragmentacja rozerwanego worka (bag-breakup) i drobne uszkodzenia, które powstają na granicy powietrze-woda pod wpływem silnego wiatru. Niniejsze opracowanie skupia się na badaniu poszczególnych przypadków efektu bag-breakup, które wystąpiły pod wpływem szybkiego przepływu suchego powietrza. Fragmentacja była szczegółowo badana zarówno pod względem jakościowym, jak i ilościowym przy pomocy zsynchronizowanego wieloperspektywnego szybkiego zapisu wideo w konfiguracji radiograficznej.

NUMERICAL SIMULATION OF AEROELASTIC EFFECTS FOR AN AIRFOIL WITH TWO DEGREES OF FREEDOM

Marek Pátý¹; Jan Halama

Czech Technical University in Prague, Faculty of Mechanical Engineering,
Department of Technical Mathematics, Center of Advanced Aerospace Technology,
Technická Street 4, Prague 6, 166 07, Czech Republic
e-mail: ¹marek.paty@fs.cvut.cz

Abstract

The pursuit of increased steam turbine power output leads to a design of low pressure stages with large diameters, featuring long and thin blades. The interaction of the structure with flow may induce vibrations, leading to a reduced operational life of the machine due to material fatigue. This work introduces a mathematical model of fluid-structure interaction, intended for the investigation of flow-induced turbine blade vibrations. At present, it is applied to a simplified test case of an isolated airfoil. The flow model is based on 2D Euler equations in Arbitrary Lagrangian-Eulerian formulation, discretized by the Finite Volume Method with a second-order accurate AUSM⁺-up scheme. The structure is modelled as a solid body with one rotational and one translational degree of freedom. The solution is realized iteratively by a time-marching method with a two-way fluid-structure coupling. In each iteration the airfoil surface pressure is integrated to determine the forces and the torsional moment driving its motion. The position of the airfoil in the next time step is obtained and the flow is resolved on a newly recreated mesh. The results of the present model are validated by comparison with experimental data and with numerical results of other models.

Keywords

Aeroelasticity; Turbine; Airfoil; Vibrations; Arbitrary Lagrange-Euler; Finite volume method.

Introduction

The phenomenon of aeroelasticity was first investigated in the field of aeronautics. Collar [1] states that the subjects of structure dynamics and aerodynamics cannot be treated separately and they have to be regarded as components of an integral analysis. He defines aeroelasticity as a discipline studying the combined effects of aerodynamic, elastic and inertial forces. Its role has since been recognized as crucial in a variety of other disciplines, such as civil engineering, biomedicine [2] and turbomachinery ([3], [4]).

The most widely investigated dynamic aeroelastic effect in aeronautics is flutter (see e.g. the works [5], [6], [7]), which is also of interest in turbomachinery [8], together with forced response analysis [9]. Flutter is a self-excited vibration of structure, caused by the interaction of aerodynamic, elastic and inertial forces. The structure aerodynamic loading leads to a deformation of the body, which in turn increases the aerodynamic forces. The wing or blade thus vibrates with amplitude of oscillations increasing in each cycle, leading to a mechanical failure. While no loss of turbine blade due to flutter is known ([4]), it has been reported to cause cracking of the blade root [10].

The problem of flutter requires considering non-linear behaviour of both flow and elastic structure, change of domain and mesh in time, flow viscosity and turbulence effects [7]. Efforts have been made in the past to simplify the problem and to restrict the model to include

only the most essential effects. The first attempts to solve the flutter problem analytically can be traced back to the works of Theodorsen [11], of interest is also the recent examination of the model by Perry [12], who introduced a model for aeroelastic flutter behaviour of an airfoil with aileron using simplifying assumptions such as potential flow and zero thickness of the wing.

The advance of Computational Fluid Dynamics (CFD) and the rise in computational power allowed treating the aeroelasticity problems with numerical approaches. In order to keep the computational demands reasonable, flutter was first modelled by superimposing linear perturbations to a steady-state nonlinear solution and casting the equations to frequency domain. However, the assumption that the steady-state flow is identical with the time-mean flow may not always be valid and linear methods are incapable of capturing important non-linear effects such as large amplitudes of blade motion or strong unsteady shocks ([13], [6]). The shortcomings of the harmonic time-linearized method are addressed by the non-linear harmonics (NLH) method introduced by Ning and He [14]. The time-mean equations are solved simultaneously with the harmonic perturbations and coupled via extra unsteady stress terms appearing due to the time-averaging. Ning and He demonstrate on a transonic compressor cascade that the NLH method captures successfully the nonlinear effects and achieves results close to a time-marching method.

The inherent drawback of the NLH method is that the unsteadiness is resolved only in a limited number of harmonics whose frequency is not a part of the solution and it has to be given as an input at the start of the procedure. The full unsteady solution of fluid-structure interaction can be obtained by time-marching methods. Traditionally, the structural mechanics problems are modelled using Lagrangian description, while the fluid dynamics problems usually employ Eulerian description [15]. The moving fluid-domain boundaries in fluid-structure interaction problems can be conveniently treated by a hybrid Arbitrary Lagrangian-Eulerian (ALE) description, allowing a deformation of the physical domain independent of the fluid particle motion (see e.g. [15], [16], [17]). The stability and accuracy of the numerical methods in ALE formulation is closely related to the Geometric Conservation Laws (GCL) which require that a constant solution is reproduced exactly. An elaborate analysis of several time-advancing schemes in view of GCL is given in [17]. The deformation of the domain implies that the grid for the ALE formulation needs to be updated accordingly, posing a third problem additionally to the fluid and structure dynamics [15]. A brief summary of grid movement techniques is provided in [6], while a complete remeshing may be required for large domain deformations [18].

As the solution of the complete fluid-structure interaction is very complex, it is often simplified by imposing only a one-way coupling between the fluid and structure dynamics. The eigenmodes and eigenfrequencies are determined in advance by a structural solver and used to prescribe the structure motion for an unsteady fluid dynamics solver ([19], [20]). The unsteady aerodynamic load on the structure surface is extracted to compute the energy transferred from the fluid to the structure and by comparison with the structural damping to evaluate the susceptibility to flutter. The underlying assumption that the effect of aerodynamic forces on the change of the structural dynamics properties can be neglected requires that the fluid density is by several orders of magnitude lower than that of the solid. This makes the method suited for turbomachinery or aeronautics, while it is inapplicable e.g. for computational medicine where the fluid and solid densities are similar [2]. However, evidence suggests that this approach may fail even in cases with significant density difference [21] and a strong fluid-structure coupling should therefore be always included.

The efforts to avoid modelling of the complete fluid-structure interaction root mainly from the incompatibility of the approaches traditionally used to treat isolated structure and fluid

dynamics problems. Typically, CFD has been solved with Finite Volume Methods (FVM) and computational structural mechanics (CSM) with Finite Element Methods (FEM), differing often in solution and discretization techniques [22]. This poses difficulty in transferring data across the fluid-structure domain interface, where the aerodynamic surface load imposes a boundary condition for structure dynamics and the displacement of the solid body deforms the fluid computational domain. A number of works has been published on solving the structure and fluid dynamics equations in a compatible fashion, some using the same discretization methods for both domains and the others a combination of different ones: Slone et al. [23] employed a single Finite Volume Unstructured Mesh discretization strategy for both fluid and structure, Sváček [7] and Honzátko [24] computed flow around a solid airfoil with two degrees of freedom using FVM- and FEM-based incompressible flow solvers respectively, Sanches and Coda [15] discretized flow equations with FEM and modelled the structure with FEM shell elements.

In the present paper, we examine the onset of flutter for a NACA 0012 airfoil modelled as a solid body with two degrees of freedom, allowing a translational and a rotational movement. The flow around the airfoil is modelled using Euler equations in ALE formulation, discretized by the FVM. A time-marching iterative procedure is employed, solving simultaneously the unsteady flow and airfoil movement with strong coupling realized via the airfoil aerodynamic loads and displacement. As the final intended application of the model is to solve flutter in turbomachinery, the employed numerical scheme for approximation of inviscid fluxes needs to be capable of resolving compressible flows accurately and of capturing shock-waves sharply. A modern flux splitting scheme AUSM+-UP was employed, introduced originally by Liou and Steffen [25] as AUSM and modified for the low-speed flow regimes by Liou [26].

1 Mathematical Model

This chapter describes the mathematical model of fluid flow around an oscillating airfoil. First, the Euler equations describing the inviscid compressible flow are introduced in ALE formulation, including the definition of boundary conditions. Then the motion of the airfoil as a solid body with one translational and one rotational degree of freedom is defined together with the coupling to the aerodynamic field.

1.1 Flow Model

We denote Ω_t the computational domain occupied by fluid at time $t \in \langle 0, T \rangle$. We aim to find the fluid density ρ , velocity $u = u(x, t)$ and static pressure p for $t \in \Omega_t$, where $u = [u_1, u_2]^T$ has two components u_1, u_2 in the directions of Cartesian axes x_1, x_2 . Further we denote the total energy $e_t \frac{1}{2}(u_1^2 + u_2^2)$, using the notation e for internal energy.

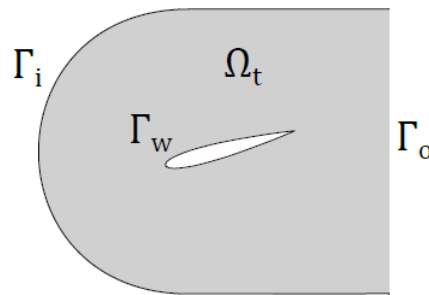


Fig. 1: Domain and boundaries (not in scale).

We consider the domain at time $t = 0$ as the reference domain $\Omega_{ref} = \Omega_0$ and introduce the ALE mapping [7]:

$$A_t: \Omega_{ref} \rightarrow \Omega_t, X \rightarrow \mathbf{x}(X, t) = A_t(X), \quad (1)$$

describing the time-dependent position $\mathbf{x} \in \Omega_t$ of a point from reference domain $X \in \Omega_{ref}$. The ALE velocity is defined as: $\mathbf{s} = \partial A_t / \partial t$. We consider the set of Euler equations [27]:

$$\frac{\partial}{\partial t} \int_{\Omega_t} \mathbf{W} d\Omega + \oint_{\Gamma(t)} \mathbf{F}(\mathbf{W}, \mathbf{n}, \mathbf{s}) d\Gamma = 0, \quad (2)$$

where $\mathbf{n} = [n_1, n_2]^T$ is the surface outward unit normal. The vector of characteristic variables \mathbf{W} , and the flux vector \mathbf{F} are defined as:

$$\mathbf{W} = \begin{bmatrix} \rho \\ \rho \mathbf{u} \\ \rho e_t \end{bmatrix}, \mathbf{F} = (\mathbf{u} - \mathbf{s}) \cdot \mathbf{n} \mathbf{W} - \begin{bmatrix} 0 \\ -p \mathbf{n} \\ -p \mathbf{s} \cdot \mathbf{n} \end{bmatrix}. \quad (3)$$

The system of equations is closed by the ideal gas law:

$$p = (\gamma - 1) \left[\rho e_t - \rho \frac{u_1^2 + u_2^2}{2} \right] \quad (4)$$

We consider three types of boundary conditions: at the airfoil wall Γ_w , at the domain inlet Γ_i and outlet Γ_o (Fig. 1). The free-slip boundary condition is applied at the airfoil wall by imposing the normal component of flow velocity equal to the normal component of wall movement velocity (Eq. 5). Freestream conditions are prescribed at the domain inlet (Eq. 6) and constant solution in the direction of boundary normal is defined at the outlet (Eq. 7).

$$[(\mathbf{u} - \mathbf{s}) \cdot \mathbf{n}]_{\Gamma_w} = 0 \quad (5)$$

$$\mathbf{u}|_{\Gamma_i} = \mathbf{u}_{FS}, \rho|_{\Gamma_i} = \rho_{FS}, p|_{\Gamma_i} = p_{FS} \quad (6)$$

$$\left. \frac{\partial \mathbf{u}}{\partial \mathbf{n}} \right|_{\Gamma_o} = \mathbf{0}, \left. \frac{\partial \rho}{\partial \mathbf{n}} \right|_{\Gamma_o} = 0, \left. \frac{\partial p}{\partial \mathbf{n}} \right|_{\Gamma_o} = 0 \quad (7)$$

The initial condition for a steady-state computation is described by freestream conditions:

$$[\rho, \mathbf{u}, p](\mathbf{x}, 0) = [\rho_{FS}, \mathbf{u}_{FS}, p_{FS}], \mathbf{x} \in \Omega_0 \quad (8)$$

The unsteady computations are performed by solving the steady-state case first and using the solution as initial condition.

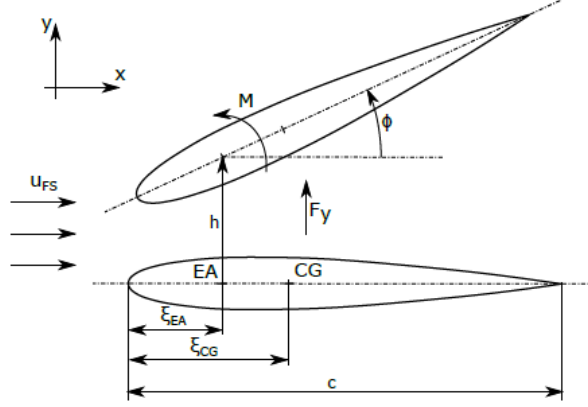


Fig. 2: Airfoil parameters and position.

1.2 Airfoil Motion

The airfoil is modelled as a solid body with two degrees of freedom, allowing movement in a vertical direction and a rotation about elastic axis (EA). The equations describing the airfoil motion can be derived from Lagrange equations (see e.g. [7]). We consider the nonlinear form:

$$\begin{aligned} m\ddot{h} + k_{hh}h + S_\phi\ddot{\phi}\cos\phi - S_\phi\dot{\phi}^2\sin\phi + b_{hh}\dot{h} &= F_y, \\ S_\phi\ddot{h}\cos\phi + I_\phi\ddot{\phi} + k_{\phi\phi}\phi + b_{\phi\phi}\dot{\phi} &= M \end{aligned} \quad (9)$$

and the linearized form, valid for small vibration amplitudes of the angle ϕ and its derivative $\dot{\phi}$:

$$\begin{aligned} m\ddot{h} + k_{hh}h + S_\phi\ddot{\phi} + b_{hh}\dot{h} &= F_y, \\ S_\phi\ddot{h} + I_\phi\ddot{\phi} + k_{\phi\phi}\phi + b_{\phi\phi}\dot{\phi} &= M, \end{aligned} \quad (10)$$

where h is the airfoil vertical displacement (positive in upwards direction), ϕ is the airfoil rotation angle (positive in counter-clockwise direction), m its mass, S_ϕ the static moment about EA and I_ϕ the moment of inertia about EA (Fig. 2). The elastic support of the airfoil has stiffness k_{hh} in vertical and $k_{\phi\phi}$ in rotational direction with the respective mechanical damping denoted as b_{hh} and $b_{\phi\phi}$. The aerodynamic load acting on the airfoil, i.e. the lifting force F_y (positive in upwards direction) and the torque M (positive in counter-clockwise direction), is calculated by integrating the airfoil pressure distribution obtained from the flow solver:

$$\mathbf{F} = \begin{bmatrix} F_x \\ F_y \end{bmatrix} = \oint_{\Gamma_w} -p\mathbf{n}d\Gamma, M = \oint_{\Gamma_w} \begin{bmatrix} x_{EA} - x \\ y - y_{EA} \end{bmatrix} \cdot \mathbf{n}pd\Gamma \quad (11)$$

2 Numerical Solution

2.1 Grid

The computational domain surrounding the NACA 0012 airfoil extends 9 chord lengths upstream, 4 chord lengths downstream and 10 chord lengths up and down vertically of the airfoil leading edge (LE). Two structured C-type grids with different level of refinement were

generated for the numerical solution. The fine grid features 516x49 cells, while the *coarse* one contains 256x24 cells (Fig. 3). The movement of the airfoil in unsteady computations requires that the mesh is updated accordingly. We consider two configurations: the reference configuration where the airfoil angle and displacement are equal to zero, and another configuration where the whole mesh is displaced and rotated as a rigid body with the airfoil.

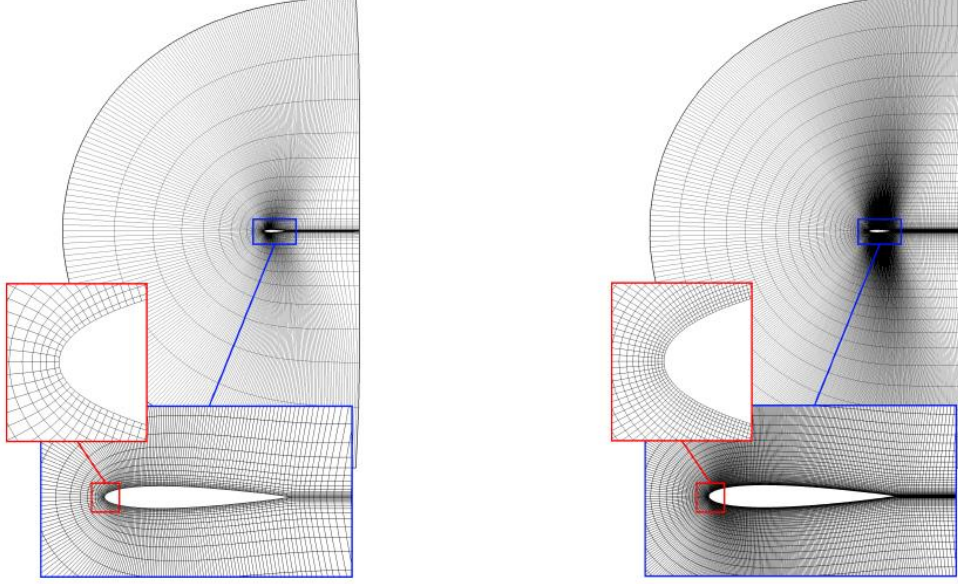


Fig. 3: Coarse (left) and fine grid (right).

The instantaneous position of each grid point is a result of linear combination of these two configurations:

$$\begin{bmatrix} x \\ y \end{bmatrix} = k \left[\begin{pmatrix} x_{ref}^{EA} \\ y_{ref}^{EA} + h \end{pmatrix} + \mathbf{Q} \begin{pmatrix} x_{ref} - x_{ref}^{EA} \\ y_{ref} - y_{ref}^{EA} \end{pmatrix} \right] + (1 - k) \begin{bmatrix} x_{ref} \\ y_{ref} \end{bmatrix}, \quad (12)$$

where h is the displacement of the airfoil elastic axis and the rotation matrix \mathbf{Q} is defined using the airfoil rotation angle ϕ :

$$\mathbf{Q} = \begin{bmatrix} \cos\phi & -\sin\phi \\ \sin\phi & \cos\phi \end{bmatrix}. \quad (13)$$

The coefficient k is a linear function of the point distance from the nearest airfoil point d_{min} , such that the grid points forming the airfoil boundary are fully displaced and the grid points further than a distance limit d_{lim} stay at their reference configuration position:

$$k = \max(1 - d_{min}/d_{lim}, 0) \quad (14)$$

2.2 Spatial Discretization of Euler Equations

The Finite Volume Method (FVM) is used for the discretization of Euler equations in ALE formulation. Let us divide the computational domain Ω into a set of N non-overlapping subsets (cells) Ω_i such that

$$\Omega = \bigcup_{i=1}^N \Omega_i, \quad \Omega_i \cap \Omega_j = \emptyset, \quad \forall i \neq j \quad (15)$$

The integral conservation law Eq. 2 has to be satisfied in each finite volume cell Ω_i . We consider the integral boundary flux of the polygonal cell as a sum of fluxes through its walls, where Γ_{ij} stands for the edge between the cell i and a neighbouring cell j and the average flux along the edge is denoted by \bar{F}_{ij} :

$$\oint_{\Gamma_i} \mathbf{F}(\mathbf{W}, \mathbf{n}, s) d\Gamma = \sum_{j \in N_i} \bar{F}_{ij} ||\Gamma_{ij}|| \quad (16)$$

The numerical approximation \tilde{F}_{ij} of the flux \bar{F}_{ij} was obtained by the AUSM-family scheme in the first (AUSM⁺, [28]) and second modification (AUSM⁺-up, [26]) by Liou. The idea of the AUSM schemes is to split the flux into the convective and pressure part and to treat them separately:

$$\tilde{F}_{1/2} = \tilde{F}_{1/2}^c + \tilde{F}_{1/2}^p, \quad (17)$$

where the $_{1/2}$ subscript indicates evaluation at cell interface.

The definition of the convective and pressure terms for M-split AUSM+ scheme in ALE formulation can be found in [29]:

$$\tilde{F}_{1/2}^c = M_{1/2}^r a_{L/R} \begin{bmatrix} \rho \\ \rho \mathbf{u} \\ \rho e_t + p \end{bmatrix}_{L/R}, \quad \tilde{F}_{1/2}^p = \begin{bmatrix} 0 \\ p \mathbf{n} \\ p \mathbf{s} \cdot \mathbf{n} \end{bmatrix}_{1/2} \quad (18)$$

where a is the speed of sound and the $_{L/R}$ subscript indicates that the expression is evaluated in either one or the other of the interface-adjacent cells, based on the upwinding principle. The notable differences of the ALE formulation in comparison to the Eulerian reference frame arise in the use of the relative Mach number $M^r = (\mathbf{u} - \mathbf{s}) \cdot \mathbf{n}/a$ instead of an absolute one and in the appearance of the new $p \mathbf{s} \cdot \mathbf{n}$ term in the pressure part of flux. Formulas for the evaluation of the interface quantities $M_{1/2}^r$, $p_{1/2}$ are introduced in [25].

The need for a universally applicable and robust numerical scheme lead to an extension of the AUSM scheme to low-speed flows with the introduction of the AUSM⁺-up modification in [26]. The newly constructed scheme is applicable to all speed regimes and removes the deficiency of the previous versions, which suffers from pressure oscillations along the grid direction with a very small velocity component, such as in the direction normal to the boundary layer. The formulation of the convective flux uses mass-flow splitting instead of Mach number splitting, here given already in the ALE formulation using the flow velocity relative to the interface to evaluate the mass-flow m^r :

$$\tilde{F}_{1/2}^c = m_{1/2}^r \begin{bmatrix} 1 \\ \mathbf{u} \\ e_t + p/\rho \end{bmatrix}_{L/R} \quad (19)$$

The extra term $p \mathbf{s} \cdot \mathbf{n}$ appears again in the pressure flux due to the ALE configuration. The reader is referred to Liou's paper [26] for the evaluation of the interface quantities. The coefficients of the scheme were set as in the example given by Liou to $K_u = 0.75$, $K_p = 0.25$ and $\sigma = 1.0$.

In order to increase the accuracy of the scheme, the quantities at the left and right side of the interface are obtained by using a linear reconstruction with TVD-based limiting of slopes [30]. In particular the min-mod limiter was employed in order to enhance the scheme stability.

2.3 Time Integration and GCL

We substitute the numerical approximation of cell fluxes (Eq.16) into the set of Euler equations (Eq. 2) and by denoting the space-averaged state vector as $\bar{\mathbf{W}}$ we obtain the following semidiscrete form:

$$\frac{d}{dt}(\bar{\mathbf{W}}\Omega)_i + \mathbf{R}_i = 0, \mathbf{R}_i = \sum_{j \in N_i} \bar{\mathbf{F}}_{ij} ||\Gamma_{ij}||, \quad (20)$$

where \mathbf{R} is the residual vector.

We use the explicit Euler scheme and the second-order accurate 4-stage Runge-Kutta scheme (RK4) to integrate the system in time. While both schemes are a routinely used technique for numerical integration, a special attention has to be paid to meeting the GCL condition for ALE formulation. The Euler scheme is defined as:

$$\mathbf{W}^{n+1} = \frac{1}{\Omega^{n+1}} [\mathbf{W}^n \Omega^n - \Delta t \mathbf{R}(\mathbf{x}^{n+1/2}, \mathbf{s}^{n+1/2}, \mathbf{W}^n)] \quad (21)$$

The GCL requires that the residual vector is evaluated on a mid-point grid in between the two time steps n and $n + 1$ [27]:

$$\mathbf{x}^{n+1/2} = \frac{\mathbf{x}^n + \mathbf{x}^{n+1}}{2}, \mathbf{s}^{n+1/2} = \frac{\mathbf{x}^{n+1} - \mathbf{x}^n}{\Delta t} \quad (22)$$

To obtain the mid-point grid, we first need to determine the position of the grid in the next time-step, denoted as \mathbf{x}^{n+1} . We transform the set of the two second-order ordinary differential equations (ODEs) describing the airfoil motion (Eq. 9 or 10) into a set of four first order ODEs:

$$\dot{\mathbf{q}} = \mathbf{f}(\mathbf{q}), \mathbf{q} = [h, \dot{h}, \phi, \dot{\phi}] \quad (23)$$

We integrate the equation numerically in time and obtain a new airfoil position:

$$\mathbf{q}^{n+1} = \mathbf{q}^n + \Delta t \mathbf{f}(\mathbf{q}^n) \quad (24)$$

Now we can employ the technique described in Section 3.1 to update the whole mesh with the new airfoil position.

The RK4 scheme is expressed as:

$$\begin{aligned} \mathbf{W}^{(0)} &= \mathbf{W}^n, \\ \mathbf{W}^{(k)} &= \frac{1}{\Omega^{(k)}} \left[\mathbf{W}^n \Omega^n - \alpha_k \Delta t \mathbf{R} \left(\mathbf{x}^{(k-\frac{1}{2})}, \mathbf{s}^{(k-\frac{1}{2})}, \mathbf{W}^{(k-1)} \right) \right], \\ k &= 1, \dots, 4, \\ \mathbf{W}^{n+1} &= \mathbf{W}^{(4)}, \end{aligned} \quad (25)$$

with the coefficients set to $\alpha_1 = 1/4, \alpha_2 = 1/3, \alpha_3 = 1/2$ and $\alpha_4 = 1$.

Again a mid-point grid is used to uphold the GCL, analogically to the Euler scheme:

$$\mathbf{x}^{(k-1/2)} = \frac{\mathbf{x}^n + \mathbf{x}^{(k)}}{2}, \mathbf{s}^{(k-1/2)} = \frac{\mathbf{x}^{(k)} - \mathbf{x}^n}{\alpha_k \Delta t} \quad (26)$$

The RK4 scheme for the temporal integration of the first order ODEs describing the airfoil motion (Eq. 23) is defined as

$$\mathbf{q}^{(k)} = \mathbf{q}^n + \alpha_k \Delta t f(\mathbf{q}^{(k-1)}) \quad (27)$$



Fig. 4: Distribution of non-dimensional pressure near airfoil LE from AUSM+ (left) and AUSM+-up scheme (right) for $u_{1,FS} = 30 \text{ m/s}$.

3 Results and Discussion

3.1 Steady-State Solution

Steady state computations were performed to validate the numerical flow model by comparison with experimental data. The airfoil is fixed in position with $h = 0 \text{ m}$ and $\phi = 0^\circ$ and the flow is iteratively computed by the time-marching method until it converges to a time-constant solution. The airfoil chord length is $c = 0.3 \text{ m}$ and the inlet boundary conditions are defined by the free-stream flow quantities $\rho_{FS} = 1.225 \frac{\text{kg}}{\text{m}^3}$, $u_{FS} = [30, 0]^T \frac{\text{m}}{\text{s}}$, $p_{FS} = 101325 \text{ Pa}$

Figure 4 shows the distribution of static pressure near the airfoil leading edge, normalized by the free-stream static pressure p_{FS} . The solutions obtained by the AUSM⁺ and AUSM⁺-up schemes are compared. As noted by Liou [26], the original AUSM⁺ scheme suffers from oscillations appearing along the grid direction with small velocity component, which are here observed in the direction normal to the airfoil surface. The pressure oscillations influence directly the airfoil pressure distribution and lead to an inaccurate computation of the airfoil aerodynamic load, yielding the AUSM⁺ scheme unusable for the present model. The modified AUSM⁺-up performs satisfactorily, as it produces a smoother static pressure distribution virtually free of spurious oscillations. The rate of convergence is demonstrated in Fig. 5 by means of density residuals. While the AUSM⁺ scheme stops converging after 70 000 iterations, the AUSM⁺-up scheme shows a steady convergence with residuals still diminishing after having dropped by 6 orders of magnitude. Note that the second order reconstruction is not employed in either of the cases, as it caused the AUSM⁺ scheme to diverge. All other computations performed in this paper employ the AUSM⁺-up scheme with reconstruction.

The comparison of computations performed on two grids with different level of refinement is shown in Fig. 6. The isolines of pressure c_p are plotted, employing the definition

$$c_p = \frac{p - p_{FS}}{\frac{1}{2} \rho_{FS} u_{ref}^2}, \quad (28)$$

where the reference velocity $u_{ref} = \sqrt{u_{1,FS}^2 + u_{2,FS}^2}$.

The discrepancy in the pressure field captured on the two grids with 256x24 and 516x49 cells is negligible, indicating that even the coarser grid is sufficiently refined.

This conclusion is further supported by the airfoil surface static pressure and velocity distribution, presented as a function of airfoil chord in Fig. 7. The pressure coefficient in Fig. 7 (a) shows close agreement between the results on the two grids and the only notable discrepancy occurs in terms of the pressure minimum at 10% C_{ax} which is by 2.4% more pronounced on the fine grid.

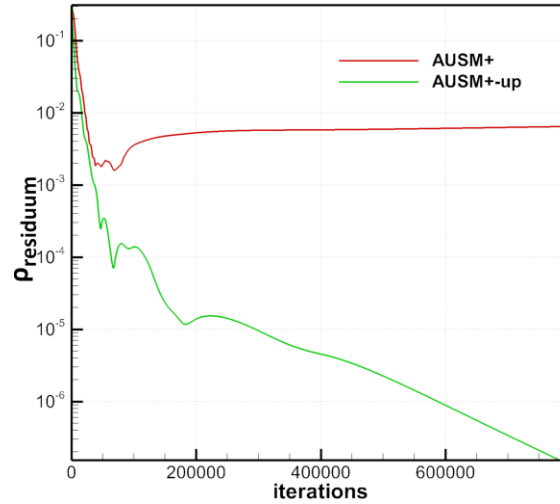


Fig. 5: Comparison of density residuals for AUSM+ and AUSM+-up schemes for $u_{1,FS} = 30$ m/s

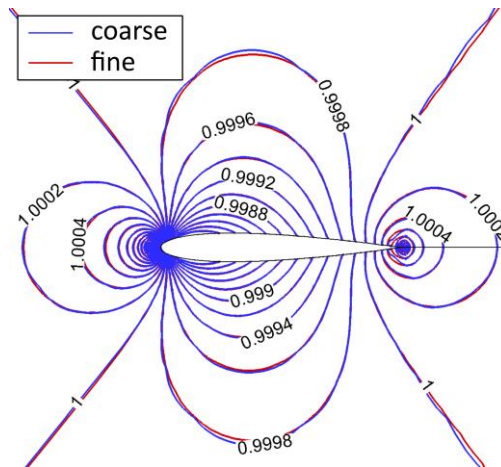
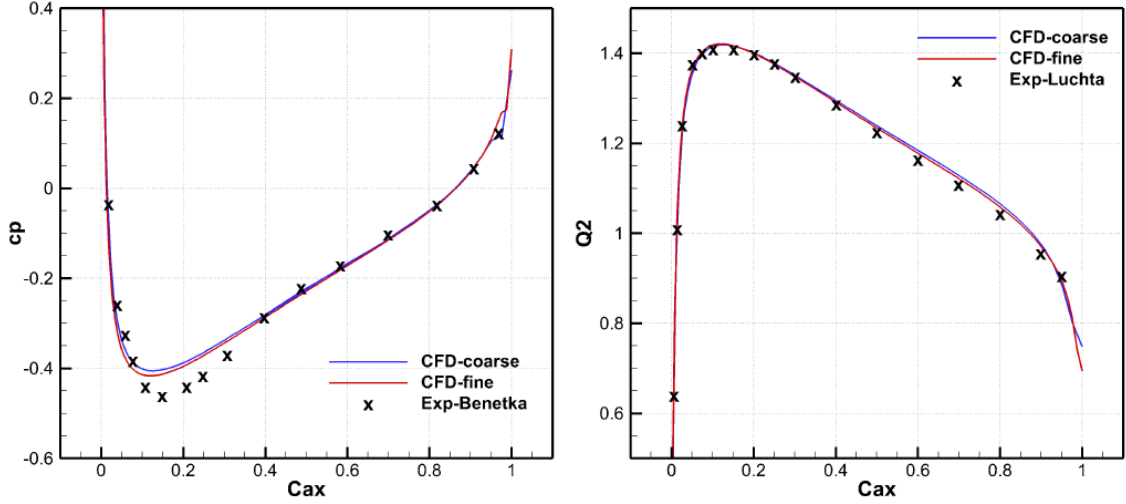


Fig. 6: Isolines of nondimensional pressure p/p_{FS} on a coarse and fine grid

Validation is provided by the experimental data of Benetka [31] which agree remarkably closely with CFD everywhere apart from the pressure minimum between 10% and 30% of C_{ax} . This underprediction of the pressure drop is not exclusive to the numerical model employed in this work and it is reported also in works of other authors using both inviscid [24] and viscous [7] flow solvers. A close match within 1.3% between numerical and experimental results [32] is found in terms of the non-dimensional squared velocity $Q^2 = (u_1^2 + u_2^2)/u_{ref}^2$, plotted in the Fig. 7 (b).



(a) Pressure coefficient

(b) Non-dimensional velocity squared

Fig. 7: Distribution of airfoil pressure coefficient c_p and non-dimensional velocity squared Q^2 on a coarse and fine grid, compared with experimental data of Luchta [32] and Benetka [31]

3.2 Prescribed Oscillation of Airfoil

This chapter presents the unsteady flow solution for a vibrating airfoil with prescribed harmonic oscillations around elastic axis. The vertical position of the elastic axis is fixed to $h = 0$ m and the rotation angle ϕ is defined as

$$\phi = \phi^{mag}(2\pi ft), \quad (29)$$

with the pitching magnitude $\phi^{mag} = 3$ and frequency $f = 30$ Hz.

The airfoil chord length is $c = 0.1322$ m and the position of elastic axis is $\xi_{EA} = 0.25c$ (Fig. 2). The inlet boundary conditions are defined by the free-stream flow quantities $\rho_{FS} = 1.225$ kg/m³, $u_{FS} = [136; 0]^T$ m/s, $p_{FS} = 101325$ Pa.

The unsteady evolution of pressure coefficient c_p is for each point on the airfoil surface approximated as

$$c_p(t) \approx c_p^{mean} + c_p^{mag} \cdot \sin(2\pi ft + c_p^\phi), \quad (30)$$

where f is the prescribed frequency of airfoil vibration, c_p^{mean} is the time-averaged value of c_p , and the magnitude of oscillations c_p^{mag} and the phase-shift c_p^ϕ are obtained by the least-squares method.

The latter three quantities are plotted in Fig. 8 together with experimental results of Benetka [33] and Triebstein [34].

The time-averaged pressure coefficient shown in Fig. 8 (a) matches well with experimental data, although the minimum at 15% C_{ax} is less pronounced. Similar discrepancy between numerical and experimental data was already discussed for the steady solution in Section 4.1. The magnitude of c_p oscillations plotted in Fig. 8 (b) is scaled to the pitching magnitude of 1 radian, i.e. multiplied by $180/\pi/\phi^{mag}$. The numerical predictions capture the trend of c_p^{mag} in agreement with the experimental results, although its magnitude is under predicted by up to 50% in the first half of C_{ax} .

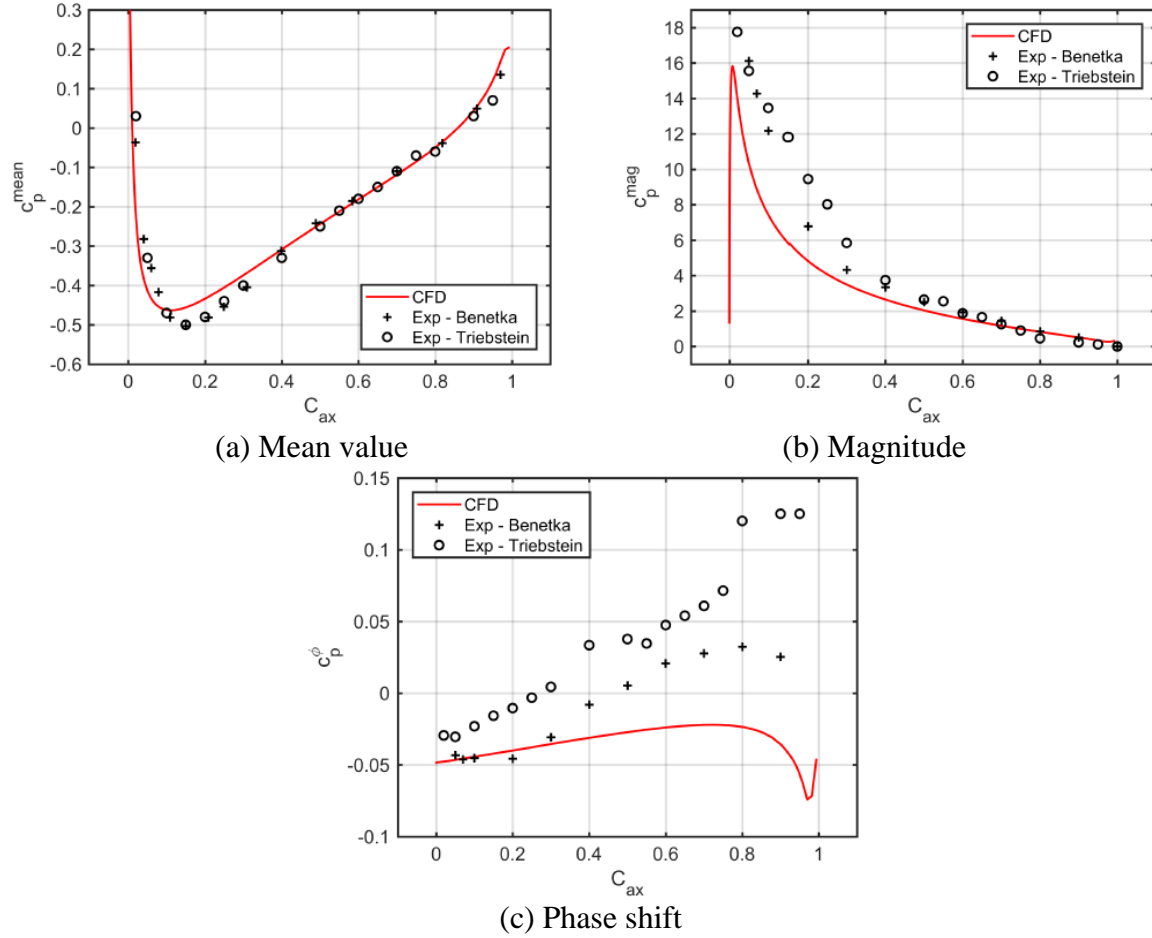


Fig. 8: Mean value, magnitude and phase shift of c_p during forced rotation. Comparison of CFD with experiments of Benetka [33] and Triebstein [34]

Both experimental and numerical data show that the phase-shift of c_p is negative near the airfoil leading edge and increases towards the airfoil trailing edge. However, while both sets measurements indicate that the phase-shift reaches positive values in the aft part of chord, the numerical prediction remains negative along the full chord length. The discrepancies can be explained by the lack of viscous flow modelling and by the difference in the size of the experimental test section and of the computational domain. While the experimental channel extends only 2.3 chord lengths up and down from the airfoil in vertical direction, the corresponding dimension of the computational domain is 10 chord lengths.

3.3 Airfoil Motion with Two Degrees of Freedom

The flow induced vibrations of an airfoil with two degrees of freedom are described in this chapter. We consider an airfoil section extruded by $l = 0.05$ m, with a weight $m = 0.086622$ kg, a static moment to elastic axis $S_\phi = -0.000779673$ kg m, a moment of inertia to elastic axis $I_\phi = 0.000487291$ kg m², a chord length $c = 0.3$ m, a stiffness of support $k_{hh} = 105.109$ N/m in vertical displacement and $k_{\phi\phi} = 3.695582$ Nm/rad in rotation and the respective damping $b_{hh} = \epsilon k_{hh}$, $b_{\phi\phi} = \epsilon k_{\phi\phi}$, with $\epsilon = 10^{-3}$. The positions of the elastic axis and center of gravity are $\xi_{EA} = 0.4c$ and $\xi_{CG} = 0.37c$ respectively, measured from the airfoil LE (Fig. 2). The remaining inlet conditions are defined by the free-stream quantities $p_{FS} = 101325$ Pa and $\rho_{FS} = 1.225$ kg/m³. The horizontal component of the freestream velocity $u_{1,FS}$ is varied, while

the vertical component $u_{2,FS} = 0$ m/s. The initial condition is obtained by running a computation with the airfoil in a fixed position until the solution converges to a steady-state.

The airfoil motion is described either by the non-linear (Eq. 9) or by the linearized (Eq. 10) equations of motion. Figure 9 compares the solutions obtained using these two definitions of airfoil movement for a freestream velocity $u_{1,FS} = 43$ m/s and an initial airfoil displacement $h_0 = 0.05$ m and pitching angle $\phi_0 = 6^\circ$. The temporal evolutions of the vertical displacement and pitching angle are plotted in Figs. 9 (a) and 9 (b) respectively. The linearization of the equations was performed under the assumption that the magnitude of the pitching angle ϕ is small and the evolutions of both quantities show that the solution is consistent with the original non-linear equations for $\phi < 13^\circ$. However, as the equations are solved numerically in either case, it is possible to use the non-linear equations without any computational penalty. The integration in time is performed using either the explicit Euler or the RK4 scheme (Eqs. 24 and 27). The figures show only the results of the latter one, as the solution obtained by the Euler scheme matches so closely that it would not be discernible within the figure resolution. This results from the small time step of the order 10^{-7} s, necessary for the stability of the explicit temporal integration schemes.

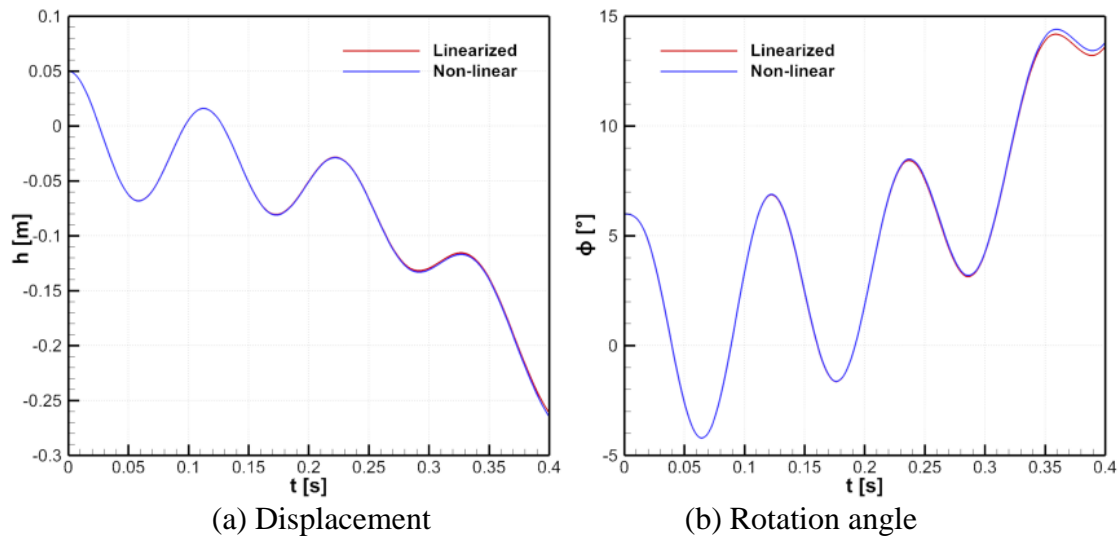


Fig. 9: Vertical displacement and rotation angle of flow-induced airfoil vibrations with $u_{1,FS} = 43$ m/s using linearized and non-linear equations of airfoil motion

The dynamic behaviour of the system for different free-stream velocities ranging from $u_{FS} = 30$ m/s to $u_{FS} = 45$ m/s is plotted in Fig. 10 by means of the airfoil displacement h (a) and pitching angle ϕ (b). The initial airfoil position is $h_0 = 0.05$ and $\phi_0 = 6^\circ$ in all cases, the airfoil motion is described by the non-linear equations and the integration in time is performed by the RK4 method. The two cases with low freestream velocities, 30 and 35 m/s, exhibit a stable behaviour with both the airfoil vertical displacement h and the pitching angle ϕ converging to zero values. An increase of freestream velocity to 40 m/s results into an unstable behavior with both parameters diverging, although the airfoil oscillations are damped and flutter does not occur. This is in agreement with the results from NASTRAN cited in Honzátko's work [24], predicting a torsional divergence to occur at $u_{FS} = 37.7$ m/s and flutter at $u_{FS} = 42.4$ m/s. According to this prediction, the last two plotted cases with freestream velocities of 43 and 45 m/s should be above the flutter boundary. The plots show that the damping of oscillations becomes substantially weaker with increasing freestream velocity, however, due to the presence of the torsional divergence it is not possible to safely conclude whether flutter actually occurs.

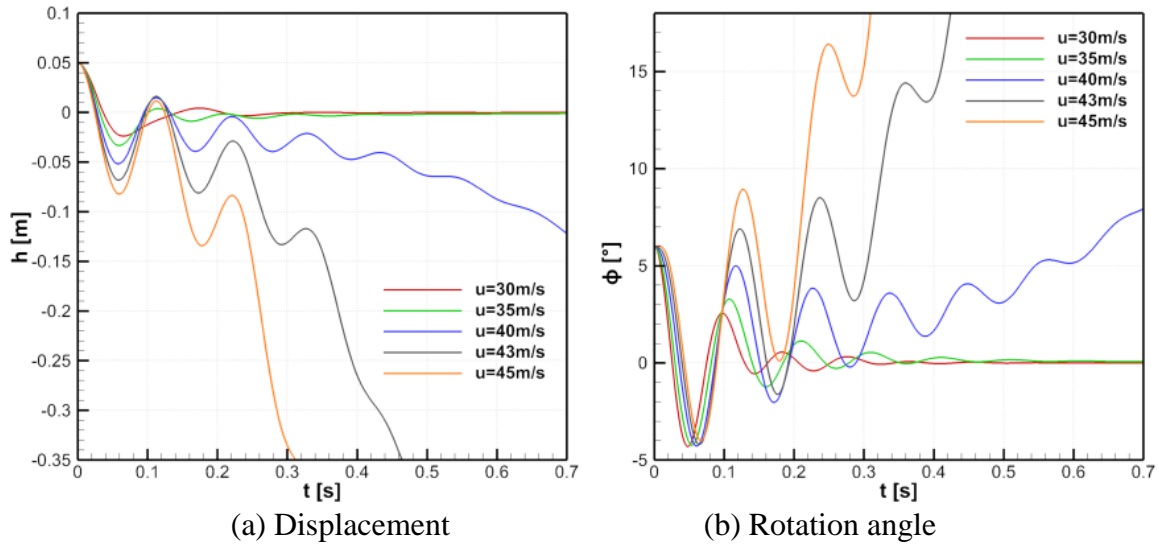


Fig. 10: Vertical displacement and rotation angle of flow-induced airfoil vibrations for varying $u_{1,FS}$

Conclusions

This paper presents results of a fluid-structure interaction model applied to the solution of flow-induced vibrations of a NACA 0012 airfoil on elastic support with two degrees of freedom. The inviscid flow model is based on the Euler equations and solved numerically by the FVM in ALE formulation. The strong two-way coupling between structure and fluid is realized via the aerodynamic loads transmitted to the structure and via the fluid-domain deformation due to the airfoil movement. The model was successfully validated by experimental data on a steady-state solution and on a test-case with forced harmonic vibrations of the airfoil. The results showed that using the AUSM⁺ scheme for low-speed flow regimes leads to a presence of spurious pressure oscillations which are removed by the modified AUSM⁺-up scheme. The predictions of the fluid-structure interaction model were in agreement with the results of other authors, showing a stable behaviour of the system for low incoming flow velocities and a torsional divergence together with a weaker damping of oscillations for higher flow velocities.

Acknowledgment

Authors gratefully acknowledge support from the ESIF, EU Operational Programme Research, Development and Education, and from the Center of Advanced Aerospace Technology (CZ.02.1.01/0.0/0.0/-16 019/0000826), Faculty of Mechanical Engineering, Czech Technical University in Prague, and from the Grant Agency of CTU in Prague, grant No. SGS16/206/OHK2/3T/12.

Nomenclature

a	speed of sound
ALE	Arbitrary Lagrangian-Eulerian
$b_{\phi\phi}$	damping in rotation
b_{hh}	damping in vertical displacement
c	airfoil chord length
C_{ax}	axial chord coordinate
c_p	pressure coefficient

CFD	Computational Fluid Dynamics
CG	center of gravity
CSM	Computational Structural Mechanics
d	distance
e	internal energy
e_t	total energy
EA	elastic axis
F	flux vector
f	frequency of airfoil oscillations
F_y	lifting force
FEM	Finite Elements Method
FVM	Finite Volumes Method
GCL	Geometric Conservation Law
h	vertical displacement of airfoil
I_ϕ	airfoil moment of inertia to EA
$k_{\phi\phi}$	stiffness in rotation
k_{hh}	stiffness in vertical displacement
l	airfoil depth
LE	airfoil leading edge
m	mass of airfoil
\dot{m}	mass-flow
M	pitching moment
n	normal
NLH	Non-Linear Harmonics
p	static pressure
Q	non-dimensionalized velocity
\mathbf{R}	vector of residuals
s	ALE velocity
S_ϕ	airfoil static moment to EA
t	time
\mathbf{u}	velocity
\mathbf{W}	vector of characteristic variables

Greek symbols

γ	Poisson constant
Ω	computational domain
Γ	domain boundary
ρ	density
ξ	coordinate along airfoil chord from LE

Sub- and Superscripts

0	initial
$\frac{1}{2}$	evaluated on the interface
FS	free-stream
I	inlet
L/R	evaluated in one of the interface-adjacent cells
mag	magnitude
mean	time-averaged
o	outlet

r	relative
ref	reference
w	wall
ϕ	phase-shift

Literature

- [1] COLLAR, A. R.: The Expanding Domain of Aeroelasticity. *The Aeronautical Journal*. 1946, Vol. 50, Issue 428, pp. 613–636. DOI: [10.1017/S0368393100120358](https://doi.org/10.1017/S0368393100120358)
- [2] WICK, T.: Coupling of fully Eulerian and arbitrary Lagrangian-Eulerian methods for fluid-structure interaction computations. *Computational Mechanics*. 2013, Vol. 52, Issue 5, pp. 1113–1124. DOI: [10.1007/s00466-013-0866-3](https://doi.org/10.1007/s00466-013-0866-3)
- [3] RZĄDKOWSKI, R.; GNESIN, V.: 3-D inviscid self-excited vibrations of a blade row in the last stage turbine. *Journal of Fluids and Structures*. 2007, Vol. 23, Issue 6, pp. 858–873. DOI: [10.1016/j.jfluidstructs.2006.12.003](https://doi.org/10.1016/j.jfluidstructs.2006.12.003)
- [4] PETRIE-REPAR, P.; MAKHNOV, V.; SHABROV, N.; SMIRNOV, E.; GALAEV, S.; ELISEEV, K.: Advanced Flutter Analysis of a Long Shrouded Steam Turbine Blade. In: *ASME Turbo Expo 2014: Turbine Technical Conference and Exposition*. 2014, Paper No. GT2014-26874. ISBN 978-0-7918-4577-6. DOI: [10.1115/GT2014-26874](https://doi.org/10.1115/GT2014-26874)
- [5] SLONE, A. K.; PERICLEOUS, K.; BAILEY, C.; CROSS, M.; BENNETT, C.: A finite volume unstructured mesh approach to dynamic fluid–structure interaction: an assessment of the challenge of predicting the onset of flutter. *Applied Mathematical Modelling*. 2004, Vol. 28, Issue 2, pp. 211–239. DOI: [10.1016/S0307-904X\(03\)00142-2](https://doi.org/10.1016/S0307-904X(03)00142-2)
- [6] KAMAKOTI, R.; SHYY, W.: Fluid–structure interaction for aeroelastic applications. *Progress in Aerospace Sciences*. 2004, Vol. 40, Issue 8, pp. 535–558. DOI: [10.1016/j.paerosci.2005.01.001](https://doi.org/10.1016/j.paerosci.2005.01.001)
- [7] SVÁČEK, P.; FEISTAUER, M.; HORÁČEK, J.: Numerical simulation of flow induced airfoil vibrations with large amplitudes. *Journal of Fluids and Structures*. 2007, Vol. 23, Issue 3, pp. 391–411. DOI: [10.1016/j.jfluidstructs.2006.10.005](https://doi.org/10.1016/j.jfluidstructs.2006.10.005)
- [8] CORRAL, R.; JAVIER, C.: Development of an Edge-Based Harmonic Balance Method for Turbomachinery Flows. In: *ASME 2011 Turbo Expo: Turbine Technical Conference and Exposition*. 2011, Paper No. GT2011-45170. ISBN 978-0-7918-5467-9. DOI: [10.1115/GT2011-45170](https://doi.org/10.1115/GT2011-45170)
- [9] GNESIN, V. I.; KOLODYAZHNAYA, L. V.; RZĄDKOWSKI, R.: A numerical modelling of stator–rotor interaction in a turbine stage with oscillating blades. *Journal of Fluids and Structures*. 2004, Vol. 19, Issue 8, pp. 1141–1153. DOI: [10.1016/j.jfluidstructs.2004.07.001](https://doi.org/10.1016/j.jfluidstructs.2004.07.001)
- [10] MASSEREY, P.-A.; McBEAN, I.; LORINI, H. Analysis and improvement of vibrational behaviour on the ND37 A last stage blade. *VGB Powertech Journal*. 2012, Vol. 92, pp. 42–48.
- [11] THEODORSEN, T.: *Report No. 496: General Theory of Aerodynamic Instability and the Mechanism of Flutter*. 1935. Technical Report. NASA Technical Documents.
- [12] PERRY, B.: *Re-Computation of Numerical Results Contained in NACA Report No. 496*. 2015. Technical Report. NASA Langley Research Center; Hampton, Virginia, United States.

- [13] DOI, H.; ALONSO, J. J.: Fluid/Structure Coupled Aeroelastic Computations for Transonic Flows in Turbomachinery. In: *ASME Turbo Expo 2002: Power for Land, Sea, and Air*. 2002, Paper No. GT2002-30313. ISBN 0-7918-3609-6. eISBN 0-7918-3601-0. DOI: [10.1115/GT2002-30313](https://doi.org/10.1115/GT2002-30313)
- [14] NING, W.; HE, L.: Computation of Unsteady Flows Around Oscillating Blades Using Linear and Nonlinear Harmonic Euler Methods. *Journal of Turbomachinery*. 1998, Vol. 120, Issue 3, pp. 508–514. DOI: [10.1115/1.2841747](https://doi.org/10.1115/1.2841747)
- [15] SANCHES, R. A. K.; CODA, H. B.: On fluid–shell coupling using an arbitrary Lagrangian–Eulerian fluid solver coupled to a positional Lagrangian shell solver. *Applied Mathematical Modelling*. 2014, Vol. 38, Issue 14, pp. 3401–3418. DOI: [10.1016/j.apm.2013.11.025](https://doi.org/10.1016/j.apm.2013.11.025)
- [16] DONEA, J.; GIULIANI, S.; HALLEUX, J. P.: An arbitrary lagrangian-eulerian finite element method for transient dynamic fluid-structure interactions. *Computer Methods in Applied Mechanics and Engineering*. 1982, Vol. 33, Issues 1–3, pp. 689–723. DOI: [10.1016/0045-7825\(82\)90128-1](https://doi.org/10.1016/0045-7825(82)90128-1)
- [17] BOFFI, D.; GASTALDI, L.: Stability and geometric conservation laws for ALE formulations. *Computer Methods in Applied Mechanics and Engineering*. 2004, Vol. 193, Issues 42–44, pp. 4717–4739. DOI: [10.1016/j.cma.2004.02.020](https://doi.org/10.1016/j.cma.2004.02.020)
- [18] SAKSONO, P. H.; DETTMER, W. G.; PERIĆ, D.: An adaptive remeshing strategy for flows with moving boundaries and fluid–structure interaction. *International Journal for Numerical Methods in Engineering*. 2007, Vol. 71, Issue 9, pp. 1009–1050. DOI: [10.1002/nme.1971](https://doi.org/10.1002/nme.1971)
- [19] MAY, M.; MAUFFREY, Y.; SICOT, F.: Numerical flutter analysis of turbomachinery bladings based on time-linearized, time-spectral and time-accurate simulations. In: *Proceedings of IFASD 2011 – 15th International Forum on Aeroelasticity and Structural Dynamics*. 2011, Paper No. IFASD-2011-080.
- [20] HÖHN, W.: Numerical Investigation of Blade Flutter at or Near Stall in Axial Turbomachines. In: *ASME Turbo Expo 2001: Power for Land, Sea, and Air*. 2001, Paper No. 2001-GT-0265. ISBN 978-0-7918-7853-8. DOI: [10.1115/2001-GT-0265](https://doi.org/10.1115/2001-GT-0265)
- [21] STOREY, P.: Holographic Vibration Measurement of a Rotating Fluttering Fan. In: *Proceedings of AIAA/SAE/ASME 18th Joint Propulsion Conference*. 1982. DOI: [10.2514/6.1982-1271](https://doi.org/10.2514/6.1982-1271)
- [22] SLONE, A. K.; BAILEY, C.; CROSS, M.: Dynamic Solid Mechanics Using Finite Volume Methods. *Applied Mathematical Modelling*. 2003, Vol. 27, Issue 2, pp. 69–87. DOI: [10.1016/S0307-904X\(02\)00060-4](https://doi.org/10.1016/S0307-904X(02)00060-4)
- [23] SLONE, A. K.; PERICLEOUS, K.; BAILEY, C.; CROSS, M.: Dynamic fluid–structure interaction using finite volume unstructured mesh procedures. *Computers & Structures*. 2002, Vol. 80, Issues 5–6, pp. 371–390. DOI: [10.1016/S0045-7949\(01\)00177-8](https://doi.org/10.1016/S0045-7949(01)00177-8)
- [24] HONZÁTKO, R.: *Numerical Simulations of Incompressible Flows with Dynamical and Aeroelastic Effects*. PhD thesis. Czech Technical University in Prague, 2007.
- [25] LIOU, M.-S.; STEFFEN Jr., Ch. J.: A New Flux Splitting Scheme. *Journal of Computational Physics*. 1993, Vol. 107, Issue 1, pp. 23–39. DOI: [10.1006/jcph.1993.1122](https://doi.org/10.1006/jcph.1993.1122)

- [26] LIOU, M.-S.: A sequel to AUSM, Part II: AUSM⁺-up for all speeds. *Journal of Computational Physics*. 2006, Vol. 214, Issue 1, pp. 137–170. DOI: [10.1016/j.jcp.2005.09.020](https://doi.org/10.1016/j.jcp.2005.09.020)
- [27] SMITH, R. W.: AUSM(ALE): A Geometrically Conservative Arbitrary Lagrangian–Eulerian Flux Splitting Scheme. *Journal of Computational Physics*. 1999, Vol. 150, Issue 1, pp. 268–286. DOI: [10.1006/jcph.1998.6180](https://doi.org/10.1006/jcph.1998.6180)
- [28] LIOU, M.-S.: A Sequel to AUSM: AUSM⁺. *Journal of Computational Physics*. 1996, Vol. 129, Issue 2, pp. 364–382. DOI: [10.1006/jcph.1996.0256](https://doi.org/10.1006/jcph.1996.0256)
- [29] DARRACQ, D.; CHAMPAGNEUX, S.; CORJON, A.: Computation of Unsteady Turbulent Airfoil Flows with an Aeroelastic AUSM+ Implicit Solver. In: *Proceedings of 16th AIAA Applied Aerodynamics Conference*. 1998. DOI: [10.2514/6.1998-2411](https://doi.org/10.2514/6.1998-2411)
- [30] HIRSCH, Ch.: *Numerical Computation of Internal and External Flows. The Fundamentals of Computational Fluid Dynamics*. Elsevier, 2007. ISBN 978-0-7506-6594-0. DOI: [10.1016/B978-0-7506-6594-0.X5037-1](https://doi.org/10.1016/B978-0-7506-6594-0.X5037-1)
- [31] BENETKA, J.: *Měření kmitajícího profilu v různě vysokých měřicích prostorech*. 1981. Technical Report Z-2610/81. Aeronautical Research and Test Institute, Prague, Letňany.
- [32] LUCHTA, J.: *Sborník charakteristik profilů křídel*. 1955. Technical Report 1669/55. VTA AZ, Brno.
- [33] BENETKA, J.; KLADRUBSKÝ, J.; VALENTA, R.: *Measurement of NACA 0012 profile in a slotted measurement section*. 1998. Technical Report R-2909/98. Aeronautical Research and Test Institute, Prague, Letňany.
- [34] TRIEBSTEIN, H.: Steady and unsteady transonic pressure distributions on NACA 0012. *Journal of Aircraft*. 1986, Vol. 23, Issue 3, pp. 213–219. DOI: [10.2514/3.45291](https://doi.org/10.2514/3.45291)

NUMERICKÁ SIMULACE AEROELASTICKÝCH ÚČINKŮ PRO PROFIL KŘÍDLA S DRUHÝM STUPNĚM VOLNOSTI

Zvyšování výkonu parních turbín vede k návrhu nízkotlakých stupňů o velkém průměru, vyznačujících se dlouhými a tenkými lopatkami. Interakce pevných těles s prouděním může způsobit vibrace, které mají za následek sníženou životnost stroje kvůli únavě materiálu. Tato práce představuje matematický model interakce pevného tělesa s tekutinou, navržený za účelem zkoumání vibrací způsobených prouděním. Model je zde aplikován na zjednodušený testovací případ osamocenému profilu leteckého křídla. Model proudění je založen na Eulerových rovnicích v Arbitrary Lagrange-Euler formulaci, diskretizovaných metodou konečných objemů. Jeho validace je provedena prostřednictvím srovnání s experimentálními daty a s numerickými výsledky jiných autorů.

NUMERISCHE SIMULATION AEROELASTISCHER WIRKUNGEN FÜR DAS PROFIL DER TRAGFLÄCHE MIT DEM ZWEITEN FREIHEITSGRAD

Die Erhöhung der Leistung von Dampfturbinen führt zum Entwurf von Niedrigdruckgraden mit einem großen Durchmesser. Diese Grade zeichnen sich durch lange und dünne Schaufeln aus. Die Interaktion der Festkörper mit der Strömung kann Vibrationen erzeugen, welche eine kürzere Lebensdauer der Maschine auf Grund von Materialermüdung zur Folge haben. Diese Arbeit stellt ein mathematisches Modell der Interaktion des festen Körpers mit Flüssigkeit vor, welches zum Zweck der Erforschung von durch Strömung verursachten Vibrationen entworfen worden ist. Das Strömungsmodell basiert auf den Eulergleichungen in der Arbitrary Lagrange-Euler-Formulierung, welche durch die Methode der endlichen Inhalte diskretisiert werden. Die Validierung des Strömungsmodells wird mittels Vergleich mit den experimentellen Daten und mit den numerischen Ergebnissen anderer Autoren durchgeführt.

NUMERYCZNA SYMULACJA AEROELASTYCZNEGO ODDZIAŁYWANIA NA PROFIL SKRZYDŁA Z DRUGIM STOPNIEM SWOBODY

Zwiększanie mocy turbin parowych skutkuje projektowaniem stopni niskociśnieniowych o dużej średnicy, charakteryzujących się długimi i cienkimi łopatkami. Interakcja ciał stałych ze strumieniem powietrza (wiatrem) może wywołać drgania, które wpływają na skrócenie okresu wytrzymałości maszyny z powodu zmęczenia materiału. Niniejsze opracowanie przedstawia matematyczny model interakcji ciała stałego z płynem, opracowany w celu badania drgań spowodowanych przepływem powietrza. Model można zastosować do uproszczonego testowania samodzielnego profilu skrzydła samolotu. Model przepływu powietrza bazuje na równaniach Eulera w procedurze Arbitrary Lagrange-Euler (ALE), zdyskretizowanych metodą objętości skończonych. Jego walidację przeprowadzono w drodze porównania z danymi doświadczalnymi i numerycznymi wynikami innych autorów.

LASER GENERATED PLASMA FOLLOWED BY SHOCKS AND INCREASING CAVITATION BUBBLE IN A MINI-GLASS TUBE

Petr Schovanec¹; Walter Garen²; Sandra Koch³; Walter Neu⁴; Petra Dančová⁵; Darina Jašíková⁶; Michal Kotek⁷; Václav Kopecký⁸

^{1,6,7,8} Technical University of Liberec, Department of Physical Measurement,
The Institute for Nanomaterials, Advanced Technology and Innovation,
Studentská 1402/2, Liberec, 461 17, Czech Republic

^{2,3,4} Hochschule Emden/Leer, University of Applied Sciences, Institute for Laser and Optics,
Constantiaplatz 4, Emden, 26723, Germany

⁵ Technical University of Liberec, Faculty of Mechanical Engineering,
Department of Power Engineering Equipment,
Studentská 1402/2, Liberec, 461 17, Czech Republic
e-mail: ¹petr.schovanec@tul.cz

Abstract

There have been tried many types of micro-capillaries, square or round and with different sizes of inner diameter. In which a cavitation bubble was created. The purpose of these experiments was to observe the velocity of the shock wave just after the initial cavitation bubble the rebound ones inside the micro-capillary and outside the micro-capillary. The most of the method was spark to induced superheat limit of liquid. Here we used the laser-induced breakdown (LIB) method. There were described the set cavitation setting that affects the stability and size of the bubble. We used here shadowgraphy setup for visualized the cavitation bubbles and shock wave with a camera. There were observed time development of the shock wave velocity; the velocity of the initial shock wave inside the micro-capillary was higher than the shock velocity outside the micro-capillary.

Keywords

Shockwave; Cavitation; Explosion bubble; Laser-induced breakdown (LIB).

Introduction

Cavitation can be defined as a collection of effects connected to the origin, activities and collapse of macroscopic bubbles in liquid. In nature and in real applications cavitation bubbles usually create a cloud, nevertheless, bubbles are not separated. The bubbles create structures which act collectively, however the essential elements of these structures are the individual bubbles. The cavitation phenomena have a great potential to be utilized in the industry, medicine, biology, pharmacy, or tissue engineering [3-4].

The research in the field of cavitation previously focused mainly on the investigation of bubble behavior in the vicinity of rigid or flexible boundaries and the bubble behavior in various liquids; [1-2] however, the current investigations also require the description of the shock waves to be included. The definition of the shock waves response can help in development of new, more resistant structures or layers. The key in understanding of cavitation shock waves interaction with various materials is investigation of impact of an individual shock wave inside a micro-capillary.

We are still not able to produce a single controllable bubble according to the cavitation definition, by pressure decrease in the liquid volume even though the current state of technology is at a very high level [1-3]. Most methods, such as spark or laser generated bubbles, are based on evaporation of a small volume of liquid, which is closer to the boiling. Another method closer to the cavitation definition is the bubbles generated by the ultrasonic field, but in this case it is almost impossible to produce a single bubble. In any case, we use the technique of laser-induced breakdown (LIB), where is still a lack of information in the experimental part of the bubble cavity investigation [1-2].

LIB is a convenient method for generating a single cavitation bubble that can be very accurately geometrically positioned in a volume of liquid and inside a glass tube [6-10]. The LIB method, using ultrashort pulses of millijoules energy, enables to generate a cavitation bubble. This method also generates natural plasma, as in thermal breakdown. Moreover, if the pulse exposure is from microseconds to femtoseconds, the plasma is in the form of optical breakdown. Multi-photon and cascade ionization occur directly during the LIB. Furthermore, impurities of the medium, spot size, light wavelength and the pulse width during the breakdown play important role. Kennedy [6] explains the entire mechanism of ionization in more detail.

Propagation of shock waves in complex media is one of the most important topics of current shock wave research. Investigation of shock wave emission in distilled water during the first bubble collapse. Shock waves generated by LIB in a glass tube filled with water are investigated experimentally.

1 Experimental

The experiment contains two lasers, a camera and a function generator. One laser serves to generate plasma, shock waves and cavitation bubbles in the liquid by means of the laser-induced breakdown the method. The second laser is double-pulse and is used to illuminate the glass tube in a cuvette for camera to take photos. The function generator serves time synchronization between the lasers and the camera.

1.1 Shock Waves in a Micro-Capillary

Shock waves propagation in the micro-capillary is seen in Fig.1. Frame (A) shows laser induced plasma in focal point that leads to a shock wave. In frame (B) shock wave induces a cavitation bubble. Frame (D) shows reflection from capillary walls. In frame (F) mutual interaction of shock waves is seen. In (G) there is rarefaction wave at cross-section. And in the last frame evolution of gas bubbles is seen [13-14].

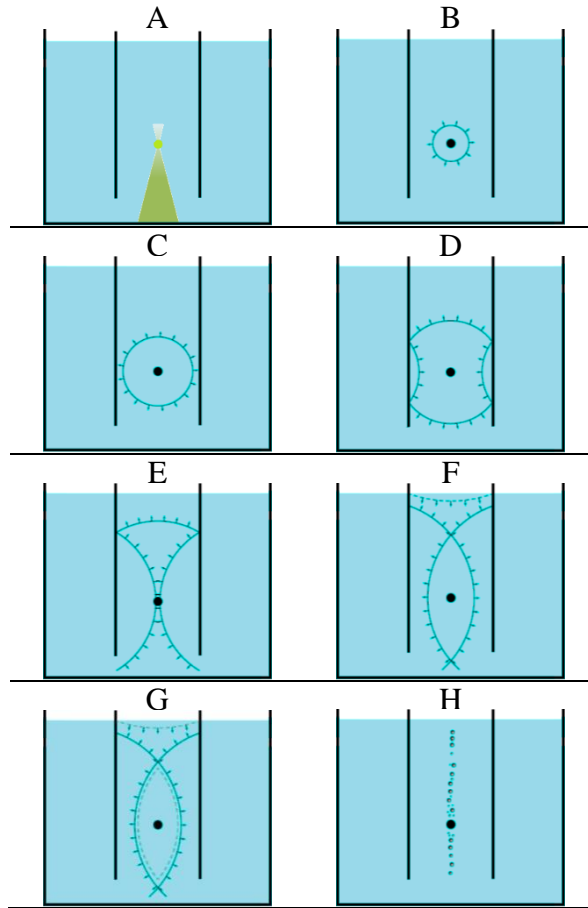


Fig. 1: Propagation of shock wave in a micro-capillary

1.2 Laser Induced Breakdown

Focusing the laser light through suitably designed optics is the most often produced optical breakdown in the liquid. Kennedy [7] described in detail the laser induced breakdown in aqueous media and its collateral effects. In addition, Vogel in [11] and [12] described the energy distribution during the growth and collapse of a laser induced bubble.

In our case we used a short pulse ($t = 6$ ns) high power laser ($\lambda = 532$ nm). The 6 ns short laser pulse was generated using the Q-switched Nd: YAG New Wave Solo III PIV pulse laser. This laser worked with one cavity for single shot generation on the wavelength of 532 nm. The Q-switch signal synchronized the camera running in a triggering mode with laser.

1.3 Optical Setup

Laser-induced breakdown (LIB) was set as an optical direct way and is seen in Fig. 2. The outlet diameter of the laser beam was 5 mm with Gaussian characteristics of the intensity. This arrangement was followed by a concave lens $f_s = 20$ mm and two plano-convex lenses $f_s = 60$ mm and $f_s = 40$ mm of 1 inch diameter. The focused laser beam created the laser point – probe (diameter < 0.1 mm).

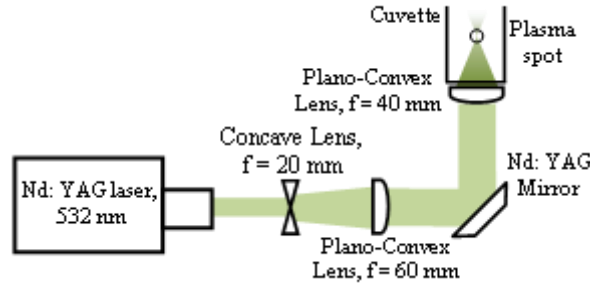


Fig. 2: The optical setup of LIB technique

1.4 Visualization Setup

Here we used a shadowgraphy setup (Fig. 3) for the shock waves visualization. This setup consists of a Nd: YAG INNOLAS pulse laser, set with DCM dye and optical filter. Opposite to the illumination laser a source CCD camera IMAGER with a microscope was placed. This camera was working in a triggering mode with a resolution of (640 x 480) pixels, and the dynamic range of 12 bit. The camera exposure time was twice 100 ns with a 100 ns time break.

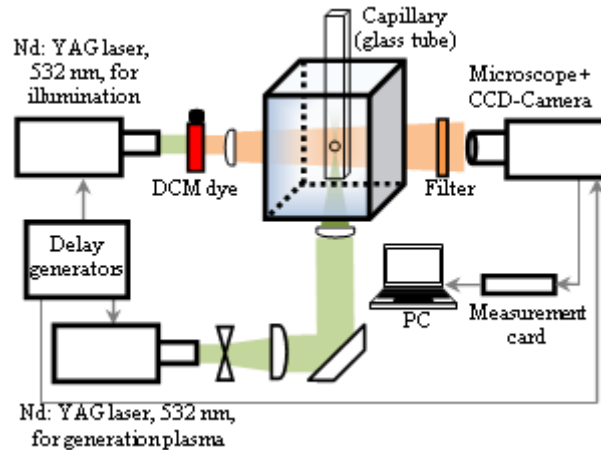


Fig. 3: The experimental setup of the visualization system

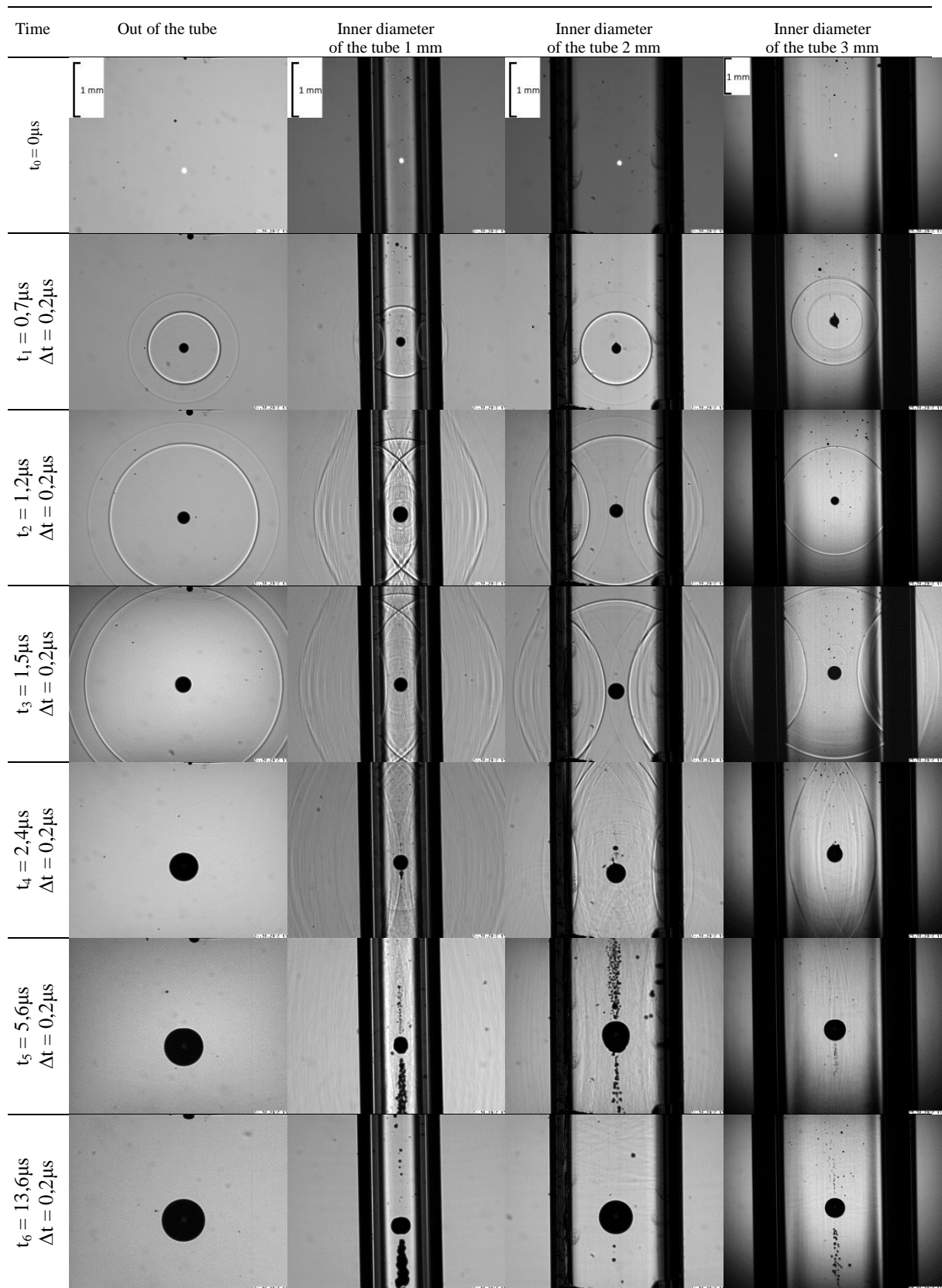


Fig. 4: Evolution of the shock waves in a micro-capillary

2 Results

There is the plasma generated in the spot due the concentration of the laser energy and the plasma is visible due the emission. The pressure in liquid increase to 103 bar, and temperature

to 103 K in the spot volume. This leads to plasma expansion at supersonic velocities, producing an acoustic shock wave followed by cavitation bubble effect. It is important to mark for the figure 4 that the laser light comes from the bottom side in the pictures.

Figure 4 presents a selected part of a series of images which has an internal frame time of 200 ns and an exposure time of two times of 6 ns. The bubbles have been generated with laser energy of 5.6 mJ. The first frames in the time of t_0 show the position of the optical breakdown. The last frames in the time of t_6 show the enlargement of the cavitation bubble, which is very close to maximum, and the frames between them show the evolution of shock wave inside the micro-capillary and outside the micro-capillary.

The frames in time t_1 show the generated bubble and its shock wave. This shock wave is captured in time 700 ns after the optical breakdown and in the same frame we can see the same shock wave for another 200 ns. The image at time t_2 represents the shock wave progress in additional after 500 ns. In the frames in the $t_3 - t_4$ time, it can be seen that the shock waves are reflected from the inner wall and move towards the bubble. Shock wave reflections occur later at the tube with a larger inner diameter. Moreover, in the smaller tube there is higher pressure. After the reflection of the shock waves from the wall of tube hits the bubble and gradually come into contact with each other, complex wave structures occur. After reflection of the colliding shock waves, first vapor bubbles become visible in the frame with tube in time t_4 , then increase in number and diameter in frame with tube in time $t_5 - t_6$.

Figure 4 in the frame in the time t_1 also shows the velocity of shock wave in the tube and outside of the tube, because we know the time and the sub-pixel resolution. The velocity of the shock wave is seen in Table 1, where we can see that velocity of the initial shock wave inside the micro-capillary was higher than the shock velocity outside the micro-capillary. Also the shock velocity as a function of time depends on the tube diameter as well the 'bubble leakage' after some microseconds.

Figure 5 shows the original pictures transformed to binary for calculation of the magnitude of the velocity of shock wave and the size of the bubble volume.

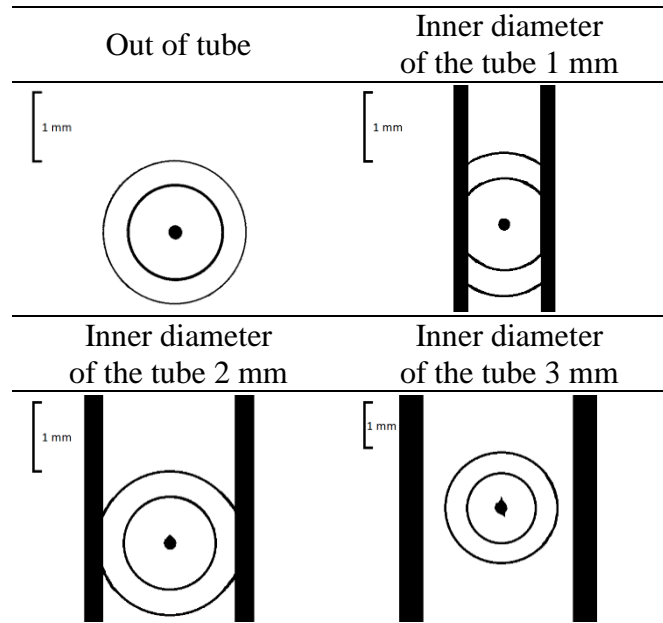


Fig. 5: Original pictures (from time t_1) transformed to binary.

Unfortunately, after transforming the original image to binary, the shock waves reflected from the inner wall of the tube cannot be seen. But for measurement of velocity of shock wave this

is very convenient. The velocity of the shock wave can seem the same, but the velocity is different, and it even depends on the diameter of the tube.

Figure 6 shows modified binary pictures. In these pictures tubes and shock waves for volume calculation are removed.

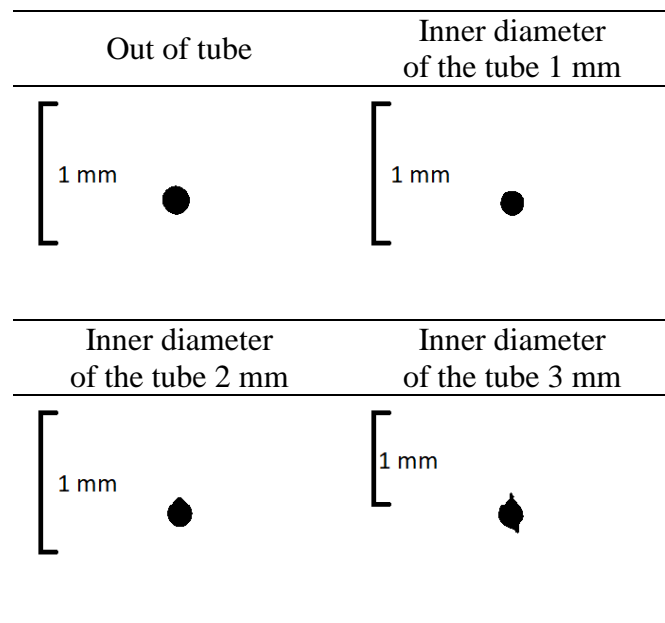


Fig. 6: Binary pictures (from time t_1) for volume calculation.

Conclusions

The visualization of cavitation bubbles and shock wave is very important and useful tool in study of cavitation process. Here we use several types of tubes where we compare the behavior and velocity of the shock wave. Velocity of propagation of shock wave in the cuvette filled with water corresponds to the speed of sound in liquids, i.e. 1500 m/s. But the velocity of shock wave in the micro-capillary is higher. It is because of pressure increase at a smaller spot, and also that shock velocity is a function of time and depends on tube diameter as well as on 'bubble leak' after several microseconds. The volume in table 1 was obtained by calculating the pixel area of captured image in Figure 6 by the approximation of the sphere.

Tab. 1: Velocity of shock wave.

Images in the time t_1	Out of the tube	1 mm tube	2 mm tube	3 mm tube
Sub-pixel resolution	1 mm = 150 px	1 mm = 150 px	1 mm = 150 px	1 mm = 100 px
Velocity of shock wave [m/s]	1500 ± 67	1600 ± 67	1667 ± 67	2000 ± 100
Time [s]	$2 \cdot 10^{-7}$	$2 \cdot 10^{-7}$	$2 \cdot 10^{-7}$	$2 \cdot 10^{-7}$
Distance [m]	$3 \cdot 10^{-6}$	$3,2 \cdot 10^{-6}$	$3,3 \cdot 10^{-6}$	$4 \cdot 10^{-6}$
Volume of bubble [mm ³]	0,015	0,014	0,015	0,016

However, in spite of these results in Figure 4, it is not yet clear whether the vapor bubbles emerge due to the pressure reduction on the vertical axis from the evaporation in the liquid or from the leakage of the cavitation bubble. Therefore, there will be a great interest in more detailed research with the use of a high-speed camera.

Acknowledgments

This work was supported by the Ministry of Education, Youth and Sports of the Czech Republic and the European Union – European Structural and Investment Funds in the frames of Operational Programme Research, Development and Education – project Hybrid Materials for Hierarchical Structures (HyHi, Reg. No. CZ.02.1.01/0.0/0.0/16_019/0000843), and the SGS project no. 21176/115.

The authors gratefully thank to the support of the Institute for Laser and Optics of the University of Applied Sciences Hochschule Emden/Leer and support of Ulrich Teubner Lab where the work was done.

Literature

- [1] JAŠÍKOVÁ, D.; SCHOVANEC, P.; KOTEK, M.; KOPECKÝ, V.: Comparison of cavitation bubbles evolution in viscous media. *EPJ Web of Conferences*. 2018, Vol. 180, Paper No. 02038. DOI: [10.1051/epjconf/201818002038](https://doi.org/10.1051/epjconf/201818002038)
- [2] JAŠÍKOVÁ, D.; SCHOVANEC, P.; KOTEK, M.; MÜLLER, M.; KOPECKÝ, V.: Comparison of ultrasound and LIB generated cavitation bubble. *EPJ Web of Conferences*. 2017, Vol. 143, Paper No. 02044. DOI: [10.1051/epjconf/201714302044](https://doi.org/10.1051/epjconf/201714302044)
- [3] JAŠÍKOVÁ, D.; SCHOVANEC, P.; KOTEK, M.; MÜLLER, M.; KOPECKÝ, V.: Experimental setup for laser-induced breakdown in aqueous media. In: *Proceedings of Optics and Measurement International Conference 2016*. SPIE 2016, Vol. 10151, Paper No. 101510L. DOI: [10.1117/12.2260998](https://doi.org/10.1117/12.2260998)
- [4] JAŠÍKOVÁ, D.; KOTEK, M.; MÜLLER, M.; KOPECKÝ, V.: Single cavitation bubble interaction close to hydrophobic surface. *International Journal of Mechanics*. 2017, Vol. 11, pp. 73–81. Available from WWW: https://www.researchgate.net/publication/316964593_Single_cavitation_bubble_interaction_close_to_hydrophobic_surface
- [5] JAŠÍKOVÁ, D.; MÜLLER, M.; KOTEK, M.; KOPECKÝ, V.: The synchronized force impact measurement and visualization of single cavitation bubble generated with LIB. *International Journal of Mechanics*. [online]. 2015, Vol. 9, pp. 76–82. Available from WWW: https://www.researchgate.net/publication/281940252_The_synchronized_force_impact_measurement_and_visualization_of_single_cavitation_bubble_generated_with_LIB
- [6] BRENNEN, Ch. E.: *Cavitation and Bubble Dynamics*. Cambridge University Press, 2013. Online ISBN 9781107338760. DOI: [10.1017/CBO9781107338760](https://doi.org/10.1017/CBO9781107338760)
- [7] KENNEDY, P. K.; HAMMER, D. X.; ROCKWELL, B. A.: Laser-induced breakdown in aqueous media. *Progress in Quantum Electronics*. 1997, Vol. 21, Issue 3, pp. 155–248. DOI: [10.1016/S0079-6727\(97\)00002-5](https://doi.org/10.1016/S0079-6727(97)00002-5)
- [8] BRUJAN, E.-A.; NAHEN, K.; SCHMIDT, P.; VOGEL, A.: Dynamics of laser-induced cavitation bubbles near an elastic boundary. *Journal of Fluid Mechanics*. 2001, Vol. 433, pp. 251–281. DOI: [10.1017/S0022112000003347](https://doi.org/10.1017/S0022112000003347)
- [9] LAUTERBORN, W.; KURZ, T.; METTIN, R.; KOCH, P.; KRÖNINGER, D.; SCHANZ, D.: Acoustic Cavitation and Bubble Dynamics. *Archives of Acoustics*. 2008, Vol. 33, Issue 4, pp. 609–617. Print ISSN 0137-5075. Online ISSN 2300-262X.

- [10] SHIMA, A.; TOMITA, Y.: The behavior of a spherical bubble near a solid wall in a compressible liquid. *Ingenieur-Archiv*. 1981, Vol. 51, Issue 3–4, pp 243–255. DOI: [10.1007/BF00535992](https://doi.org/10.1007/BF00535992)
- [11] VOGEL, A.; BUSCH, S.; PARLITZ, U.: Shock wave emission and cavitation bubble generation by picosecond and nanosecond optical breakdown in water. *The Journal of the Acoustical Society of America*. 1996, Vol. 100, Issue 1. DOI: [10.1121/1.415878](https://doi.org/10.1121/1.415878)
- [12] VOGEL, A. et al.: Energy balance of optical breakdown in water at nanosecond to femtosecond time scales. *Applied Physics B: Lasers and Optics*. 1999, Vol. 68, Issue 2, pp. 271–280. DOI: [10.1007/s003400050617](https://doi.org/10.1007/s003400050617)
- [13] KAI, Y.; MEYERER, B.; GAREN, W.; TEUBNER, U.: Experimental investigation of laser generated shock waves and the onset of evaporation in a mini-shock glass tube filled with water. In: *ISIS21, the 21st International Shock Interaction Symposium*. Riga, Latvia, 2014, pp. 168-170.
- [14] GAREN, W.; HEGEDŰS, F.; KAI, Y.; KOCH, S.; MEYERER, B.; NEU, W.; TEUBNER, U.: Shock wave emission during the collapse of cavitation bubbles. *Shock Waves*. 2016; Vol. 26, Issue 4, pp 385–394. DOI: [10.1007/s00193-015-0614-z](https://doi.org/10.1007/s00193-015-0614-z)

LASEROVĚ VYGENEROVANÁ PLASMA NÁSLEDOVANÁ RÁZY A ZVÝŠENOU KAVITAČNÍ BUBLINOU V MIKROKAPILÁŘE

Bylo testováno mnoho typů mikrokapilár, čtvercových, kulatých a různých velikostí vnitřního průměru, ve kterých byla vytvořena kavitační bublina. Účelem těchto experimentů bylo sledovat rychlost rázové vlny těsně po počáteční kavitační bublině a odrazové vlny uvnitř i vně mikrokapilár. Hlavní metodou byla jiskra indukovaného limitu přehřátí kapaliny. Zde jsme použili metodu rozbití indukovanou laserem (LIB). Bylo popsáno nastavení kavitace, které ovlivňuje stabilitu a velikost bubliny. Pro snímání bublinek kavitace a rázové vlny jsme použili radiografické nastavení s kamerou. Byl pozorován časový vývoj rychlosti rázové vlny; rychlost počáteční rázové vlny uvnitř mikrokapiláry byla vyšší než rychlost rázu mimo mikrokapiláru.

LASERGENERIERTES PLASMA, GEFOLGT VON STÖSSEN UND EINER ERHÖHTEN KAVITATIONSBLASE IN EINER MIKROKAPILLARE

Es wurden viele Typen von Mikrokapillaren getestet, quadratische, runde und verschiedene Größen des inneren Durchschnitts, in welchen eine Kavitationsblase gebildet wurde. Der Zweck dieser Experimente bestand in der Beobachtung der Geschwindigkeit der Stoßwelle gleich nach der anfänglichen Kavitationsblase und der Abprallwelle innerhalb und außerhalb der Mikrokapillare. Die Hauptmethode bestand im Funken des induzierten Limits der Überhitzung der Flüssigkeit. Hier haben wir die mit dem Laser induzierte Methode des Zerschlagens (LIB) angewendet. Es wurde die Einstellung der Kavitation beschrieben, welche die Stabilität und die Größe der Blase beeinflusst. Für die Abnahme der Kavitationsblase und der Stoßwelle haben wir eine radiografische Einstellung mit der Kamera benutzt. Es wurde die zeitliche Entwicklung der Geschwindigkeit der Stoßwelle beobachtet; die Geschwindigkeit der anfänglichen Stoßwelle innerhalb der Mikrokapillare war höher als die Geschwindigkeit des Stoßes außerhalb der Mikrokapillare.

LASEREM WYGENEROWANA PLAZMA POCIĄGAJĄCA ZA SOBĄ FALE UDERZENIOWE I ZWIĘKSZONY PĘCHERZYK KAWITACYJNY W MIKROKAPILARZE

Testowi poddano wiele rodzajów mikrokapilar, kwadratowych, okrągłych i o różnych wielkościach wewnętrznej średnicy, w których powstał pęcherzyk kawitacyjny. Doświadczenia te miały na celu zbadanie prędkości fali uderzeniowej powstającej tuż po początkowym pęcherzyku kawitacyjnym oraz odbicia fali wewnątrz i na zewnątrz mikrokapilary. Główną zastosowaną metodą było wywołanie indukowanej granicy przegrzania cieczy. W tym przypadku zastosowaliśmy metodę rozbitia indukowaną laserem (LIB). Opisano charakterystykę kawitacji, wpływającą na stabilność i wielkość pęcherzyka. Do badania pęcherzyków kawitacyjnych i fali uderzeniowej zastosowaliśmy radiografię z kamerą. Obserwowano kształtowanie się szybkości fali uderzeniowej w czasie. Prędkość początkowej fali uderzeniowej wewnątrz mikrokapilary była większa od prędkości uderzenia poza mikrokapilarą.

APPLICATION OF MACH-ZEHNDER INTERFEROMETERS FOR ISOLATOR SHOCK TRAINS

Taishi Takeshita¹; Shinichiro Nakao; Yoshiaki Miyazato

The University of Kitakyushu, Faculty of Environmental Engineering,
Department of Mechanical Systems Engineering,
1-1 Hibikino, Wakamatsu-ku, Kitakyushu, Fukuoka, 808-0135, Japan
e-mail: y7mba011@eng.kitakyu-u.ac.jp

Abstract

A Mach-Zehnder interferometer system combined with a high-speed camera is applied for a shock train in a constant-area straight duct to clarify its unsteady characteristic in which just upstream of the shock train the freestream Mach number is 1.44, the unit Reynolds number is $4.97 \times 10^7 \text{ m}^{-1}$, and the boundary layer thickness is 0.472 mm. An instantaneous two-dimensional density field in the shock train is quantitatively obtained with high spatial resolution. The present Mach-Zehnder interferometer system is found to be effective for unsteady density measurements in shock-dominated flows in a two-dimensional duct. The oscillatory characteristic of each shock in the shock train is demonstrated by power spectral analysis of the unsteady density field.

Keywords

Shock train; Supersonic flow; Unsteady flow; Mach-Zehnder interferometer; Density measurement.

Introduction

Over the past few decades, the development of dual-mode scramjet engines for realizing next-generation propulsion systems has been aggressively conducted. Dual-mode scramjet engines provide a practical solution to supersonic flight by operating under a wide range of Mach numbers. In the ramjet mode, the incoming air is compressed through shock trains known as precombustion shocks before entering the combustion chamber. To isolate the effect of flight conditions on shock trains, a nearly constant area duct referred to as an isolator is placed between the inlet and the combustor [1].

Matsuo et al.[2] have reviewed past experimental, theoretical, and numerical investigations on the subject of shock trains and showed that when a normal shock in a constant-area straight duct is strong enough to separate the boundary layer, the shock is bifurcated and one or more shocks appear downstream of the bifurcated shock. A series of repeated shocks has been called in many ways by many researchers, multiple shocks, shock systems, for example. Matsuo et al. referred to such a series of repeated shocks as a shock train in their review paper in 1999 [2]. The shock train is followed by a pressure recovery region contributed to mixed supersonic-subsonic if the duct is long enough. Therefore, the effect of the interaction extends over a great distance and the flow is decelerated from supersonic to subsonic through the whole interaction region. In this sense, the interaction region including the shock train in it is called “pseudo-shock”. However, the term “shock train” as well as “pseudo-shock” has been used in confusing way even now.

Under certain operating conditions shock trains or pseudo-shocks are widely observed in various fluid machineries such as supersonic intakes, supersonic diffusers and high-pressure

pipe lines, strongly affecting local heat transfer rates as well as aerodynamic loading. Most of the research so far has focused on time-averaged characteristics of shock trains including the length of a pseudo-shock and pressure distribution along the duct wall, the structure of shock trains by Schlieren visualization. In addition, from studies conducted mainly in the Japanese research institutions including Kyushu University, Tokyo Institute of Technology, and Muroran Institute of Technology, it is widely recognized that a shock train oscillates across its time-mean position and extreme pressure fluctuation caused by the shock train oscillation, induces vibration of the machineries or causes heavy sound noise to be emitted into the atmosphere [2]. In recent years, the physics on the behavior of an unsteady shock train has attracted much attention from researcher community engaged in the design of scramjet engines all over the world [3-9], because higher engine thrust can be achieved if a shock train is confined to the isolator of the scramjet engine and shock train oscillations have a significant effect on the unstart of the engine.

Previous research found that shock trains have two-types of unsteady motions: one is the self-excited oscillation [10, 11] associated closely with the unsteadiness induced by the interaction of a shock wave with a boundary layer, and the other is the forced-shock train oscillation [11, 12] contributed to fluctuating back-pressures. In most of the experimental studies on shock train oscillations, wall pressure measurements were performed and hence, little is investigated about the detail of unsteady characteristics inside of a shock train. Therefore, the aims of the present study are to provide reliable experimental data for validating numerical simulations of shock trains in internal gas flows and to clarify unsteady characteristics of the two-dimensional density field in a shock train in which a Mach-Zehnder interferometer system combined with a high-speed digital camera is utilized. The wedge fringe method is applied to perform the fringe shift analysis of the interferogram for density fields. The two-dimensional unsteady density field including the shock-train is for the first time elucidated by the present experiment.

1 Experimental Apparatus

Experiments were carried out in a blow down facility with a Mach-Zehnder interferometer system of High-Speed Gasdynamics Research Laboratory at the University of Kitakyushu. A schematic diagram of the experimental apparatus is shown in Figure 1. The air supplied by a compressor that pressurizes the ambient air up to 1 MPa is filtered, dried and stored in a reservoir with a total capacity of 4 m³. The high-pressure dry air from the reservoir is stagnated in a plenum chamber shown in Figure 1 and then discharged into the atmosphere through a test section. In the present experiment, the plenum pressure is controlled and maintained constant during the testing by a solenoid valve. The operating pressure ratio p_{os}/p_b of plenum pressure p_{os} to back pressure p_b was held constant at 1.7.

Figure 2 shows a schematic diagram of the test section. The test section consists of a Laval nozzle followed by a constant-area straight duct. The nozzle is designed by the method of characteristics to provide uniform and parallel flow at the nozzle exit plane and its design Mach number is 1.5. The nozzle has heights of 4.24 mm and 5 mm at the throat and exit, respectively, a constant width of 13 mm over the full length from the inlet to exit. The constant-area duct with a height of 5 mm and a width of 13 mm is connected to the exit of the supersonic nozzle. The duct has 40 static pressure measuring locations with a tap of 0.5 mm in diameter along the center line of the upper and lower walls at an equal interval of 1 mm over the range from $x = 0$ mm to $x = 39$ mm. Each static pressure tap is connected to the digital pressure sensor (Yokogawa Model MT220) with uncertainty of ± 50 Pa through a polyvinyl chloride tube with an inner diameter of 0.7 mm and a length of 500 mm. The dashed line in Figure 2 indicates the range of an optical window for flow visualization.

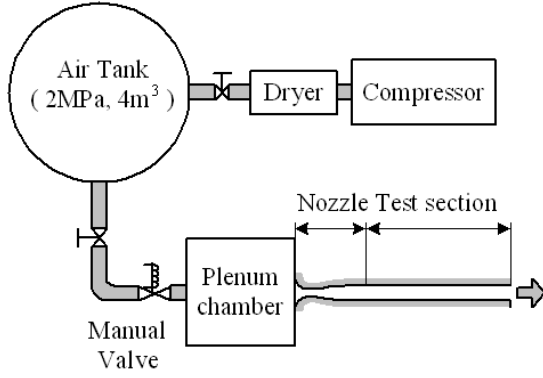


Fig. 1: Schematic diagram of experimental set up

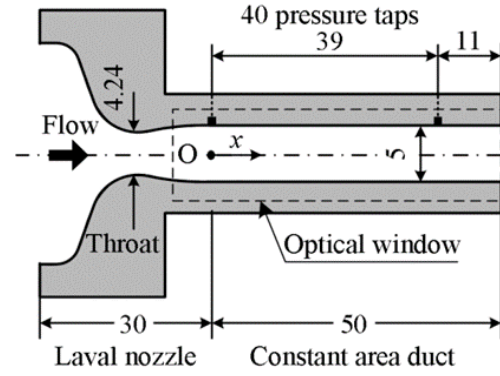


Fig. 2: Test nozzle

2 Mach-Zehnder Interferometers

As shown in Figure 3, a Mach-Zehnder interferometer system combined with a high-speed digital camera is used to measure an unsteady two-dimensional density field including a shock train and a He-Ne laser is utilized as a light source. Mach-Zehnder interferometers can estimate the unsteady features of the whole density field in the duct including the shock displacement by analyzing the fringe shift from a reference image. The wedge fringe method can measure density more minutely than the infinite fringe method by analyzing a fringe shift and it is also capable to capture density fields with high spatial resolutions, therefore, in the present work, the wedge fringe method is employed for the fringe shift analysis. Visualization of the shock train for a specified operating pressure ratio is recorded in 20,000 pictures with 2,000 frames per second. The effective spatial resolution of the present imaging system is 22 pixel/mm or 0.045 mm/pixel. Using the present Mach Zehnder system, the instantaneous position of each shock in the shock train and the corresponding frequency can be measured with high spatial and temporal resolution.

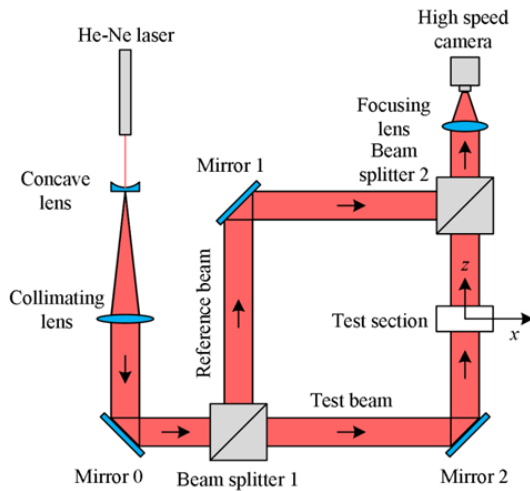


Fig. 3: Mach-Zehnder interferometer system

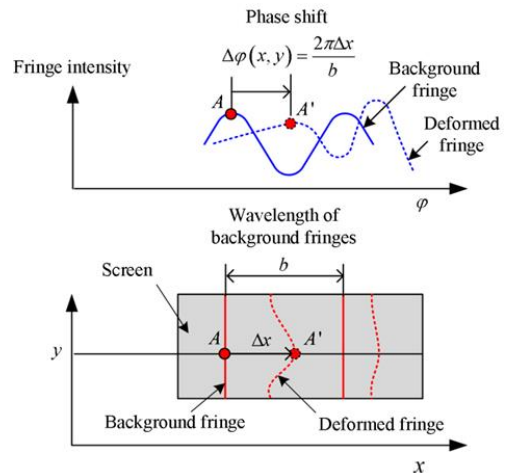


Fig. 4: Background and deformed fringe patterns

The analytical procedure for interferograms obtained from experiments is divided into two steps, which are the fringe shift analysis and density calculation from the fringe shift, see Figure 4. The former is done using the Fourier transform method, which is presented by Takeda et al. [13] and can obtain a fringe shift two-dimensionally with a high space resolution. The latter is done under the assumption that a flow field is two-dimensional. The

quantitative methodology of extracting the two-dimensional density field in the test section is described below.

The intensity profile $g(x, y)$ of the deformed fringe pattern can be given by

$$g(x, y) = g_0(x, y) + g_1(x, y) \cos[k_0 x + \Delta\varphi(x, y)] \quad (1)$$

with the phase shift $\Delta\varphi(x, y)$ containing the desired information on the density field in the test section where $g_0(x, y)$ and $g_1(x, y)$ represent unwanted irradiance variations arising from the nonuniform light reflection or transmission when the test beam passes through the test section, and $k_0 = 2\pi/b$. The coordinates x and y form the vertical plane, which is perpendicular to the test beam propagation direction, and the z -axis is taken as the direction in which the test beam propagates.

Eq. (1) is rewritten in the following expression

$$g(x, y) = g_0(x, y) + c(x, y) \exp(ik_0 x) + c^*(x, y) \exp(-ik_0 x) \quad (2)$$

with

$$c(x, y) = \frac{1}{2} g_1(x, y) \exp[i\Delta\varphi(x, y)] \quad (3)$$

where i is the imaginary number and the asterisk $*$ denotes a complex conjugate.

The Fourier transform of Eq. (2) with respect to x is given by

$$G(k, y) = G_0(k, y) + C(k - k_0, y) + C^*(k + k_0, y) \quad (4)$$

where the capital letters denote the Fourier transforms of the respective primitive functions and k is the spatial wave number in the x direction. Since the spatial variations of, $g_0(x, y)$, $g_1(x, y)$, $\Delta\varphi(x, y)$ and are slow compared with the spatial frequency k_0 when the interval between fringes is sufficiently small, the Fourier spectra in Eq. (4) are separated by the wave number k_0 and have the three independent peaks, as schematically shown in Figure 5 (a) [14].

We make use of either of the two spectra on the carrier, say $C(k - k_0, y)$, and translate it by k_0 on the wave number axis toward the origin to obtain $c(x, y)$, as shown in Figure 5 (b).

The unwanted background variation $G_0(k, y)$ has been filtered out in this stage by a pertinent band pass filter. We compute the inverse Fourier transform of $C(k, y)$ with respect to the k to obtain $c(x, y)$, defined by Eq. (3). Then we calculate a complex logarithm of Eq. (3) as follows:

$$\ln c(x, y) = \ln \frac{g_1(x, y)}{2} + i\Delta\varphi(x, y) \quad (5)$$

From Eq. 5, we can obtain the phase shift $\Delta\varphi(x, y)$ in the imaginary part completely separated from the unwanted amplitude variation $g_1(x, y)$ in the real part. The phase shift $\Delta\varphi(x, y)$ is related to the density field through the Gradstone-Dale formula as follows:

$$\frac{\Delta\varphi(x, y)}{2\pi} = \frac{K}{\lambda_0} \int_{-w/2}^{w/2} [\rho(x, y) - \rho_a] dz \quad (6)$$

where $w = 13$ mm is the span-wise length of the test section, ρ_a is the atmospheric density, λ_0 is the wavelength of a light source in vacuum, and $K = 2.2587 \times 10^{-4} \text{ m}^3/\text{kg}$ is the Gradstone-Dale constant. Considering the two-dimensional refractive index field, i.e., independent of the z axis, the density $\rho(x, y)$ in the flow field is expressed by

$$\rho(x, y) = \rho_a + \frac{\lambda_0}{2\pi K w} \Delta\varphi(x, y) \quad (7)$$

Since Eq. (7) shows that the phase shift at a fixed time is directly proportional to the flow density at the same time, characteristics of an unsteady flow field including a shock train can be evaluated by examining the time history of the fringe shift. An image of the flow field in the test section by the Mach-Zehnder interferometer is formed onto the CMOS sensor of a high-speed digital camera (Photron, FASTCAM SA1.1) which records a JPEG RGB image (24-bit each color) at a resolution of 1024×288 square pixels. The plane of focus is located in the front window of the test section. The RGB image is then turned into an 8-bit grayscale image by a linear transformation. Therefore, the distributions of background and deformed fringes with 256 different possible intensities can be calculated from the Mach-Zehnder images for the density-field in the test section.

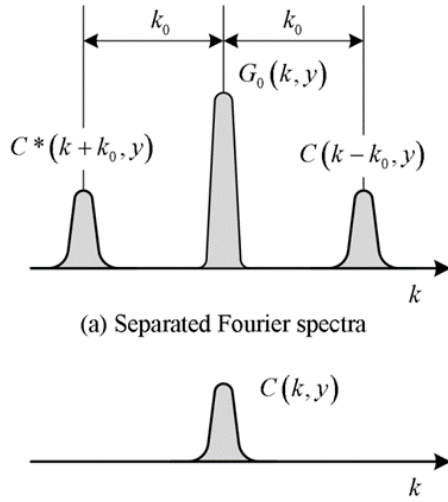


Fig. 5: Fourier transform method fringe patterns

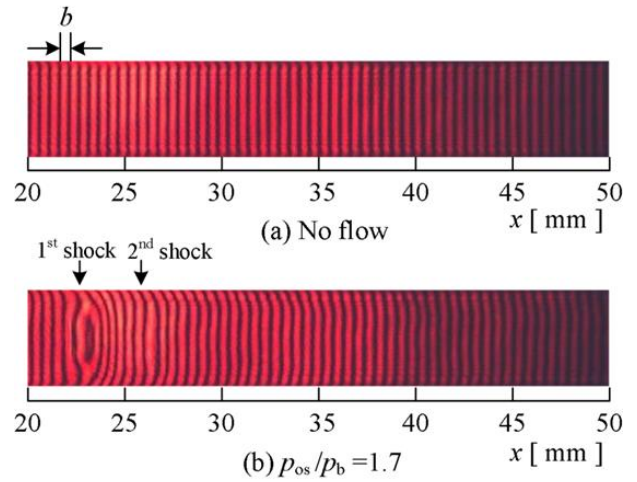


Fig. 6: Interferograms of density field

3 Results and Discussion

A typical interferogram before an experiment is performed ($p_{os}/p_b = 1.0$) is shown in Figure 6 (a) in which parallel fringes with an interval b perpendicular with respect to the duct centerline can be observed where the x is the stream-wise distance from the test section inlet. The interferograms visualized in Figure 6 (a) is called the background fringe. When the ratio of plenum to back pressures increases to $p_{os}/p_b = 1.7$, deformed fringes of a two-dimensional density field including a shock train with the flow from left to right are produced as shown in Figure 6 (b) in which the plenum pressure p_{os} is 172.2 kPa, the back pressure p_b is 101.3 kPa (the atmospheric pressure), and the atmospheric temperature T_b is 300.2 K.

The fringe displacements due to the interaction of a normal shock wave with a boundary layer can also be clearly seen in an area between $x = 20$ mm and 30 mm and fringe displacements in the stream-wise direction are almost symmetric with respect to the duct centerline. Although a shock train consisting of around two shocks can be faintly visible in the test section, we cannot obtain more information on the detailed structures of the shock train from this interferogram alone.

A typical contour plot of the two-dimensional density field including a shock train in a constant-area straight duct is presented in Figure 7 with the flow from left to right. The three

shock waves can be observed in the picture. The positions of each shock constituting the shock train are indicated in Figure 7 as the downward arrows. Just upstream of the shock train, the freestream Mach number $M_{1\infty}$ is 1.44, the unit Reynolds number Re/m is $4.97 \times 10^7 \text{ m}^{-1}$, the boundary layer thickness δ_1 is 0.472 mm, and the boundary layer displacement thickness δ_1^* is 0.189 mm. The first shock wave is bifurcated at the near the wall surface, while following two shock waves are not. The structure of the two-dimensional density field in the shock train and the downstream region is demonstrated in detail with hue spatial variations.

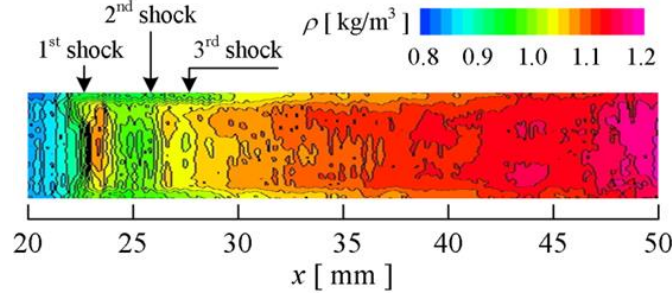


Fig. 7: Density contour map for shock train

The time-mean density distribution along the duct centerline in an unsteady density field including a shock train is indicated in Figure 8 where the downward arrows show the time-mean position for each shock in the shock train. It shows that a successive sudden increase in the density is due to the presence of the successive three shock waves constituting the shock-train. The steepest slope in the density is observed at the location of the first shock and the slopes of the following shocks gradually decrease in the downstream direction because the strength of the shock decreases toward the downstream. The density abruptly increases with a density spike at the location just behind of the first shock and then decreases soon before sudden increase again by the second shock and a similar density variation is repeated between the successive downstream shocks. After the shock train region, the density continues to rise gradually towards the downstream because of the mixing zone between supersonic flows near the wall surface and subsonic flows after the shock train [1] and it finally becomes to be equal to the atmospheric density at the nozzle exit.

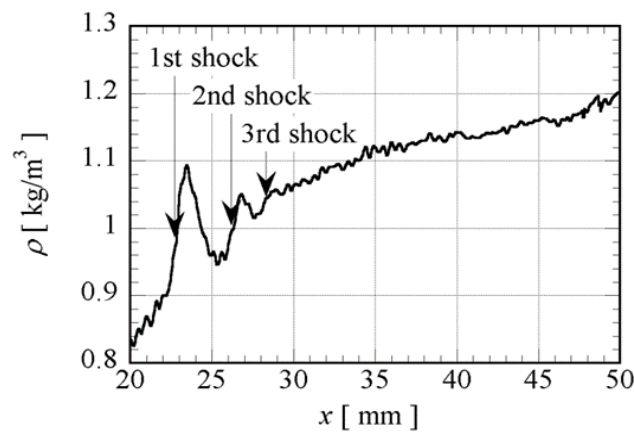


Fig. 8: Centerline density profile in shock train

The power spectral density distributions of the density fluctuation responsible for the oscillation of each shock in the shock train are given in Figure 9 where the density time histories are captured at the time-mean position of each shock at the duct centerline. The first shock wave oscillates at a dominant frequency of around 10 Hz and the second and third

shocks also show almost the same dominant frequency. These dominant frequencies obtained from the density fluctuations are of almost the same order of magnitude as those from wall pressure measurements in a past research [1].

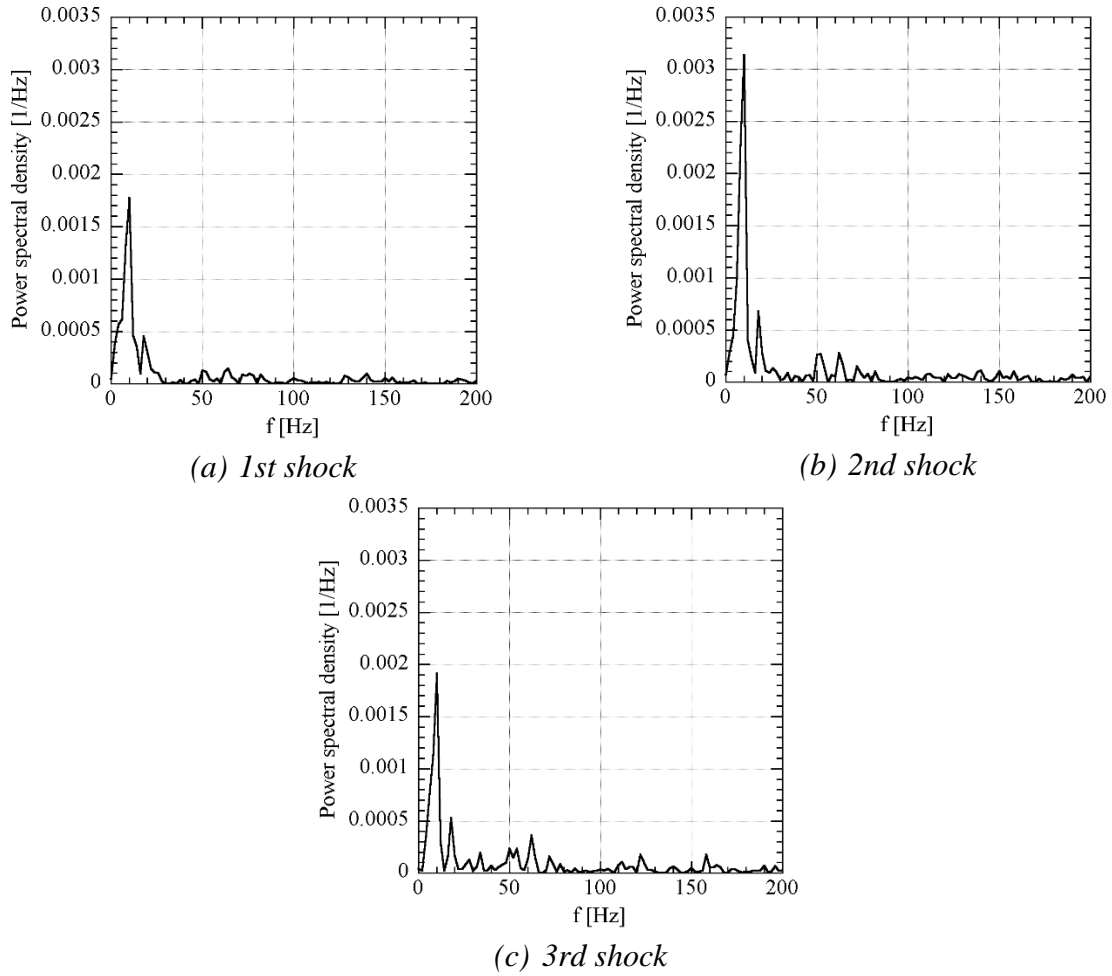


Fig. 9: Power spectral density for each shock in shock train

Conclusions

The Mach-Zehnder interferometer is effective in studying quantitatively the density fields in supersonic flows at high precision and high spatial resolution. However, there has been no practical application of the Mach-Zehnder interferometer for shock trains. The present study quantitatively observed the two-dimensional unsteady density field including a shock train using a high-speed Mach-Zehnder system. The unsteady characteristic of each shock in the shock train was shown by the power spectral density representation. As a result, it is found that the present high-speed Mach-Zehnder system is an effective tool to investigate quantitatively the dynamics of the interaction of a shock wave with a turbulent boundary layer in a two-dimensional confined duct.

This research is an extension of the previous experimental study [15] in which the rainbow Schlieren deflectometry was applied for measurements of the density field in a shock-train and time-mean flow characteristics of the shock train were quantitatively captured. The present results from the Mach-Zehnder interferometer will be compared with those from the rainbow Schlieren deflectometry in the near future.

Acknowledgment

The authors would like to gratefully acknowledge the assistance of graduate students Yusuke Awata and Yuki Sakamoto of the University of Kitakyushu for their invaluable support to the experimental work and exceptional skills in the fabrication of the facility.

Nomenclature

i	imaginary number
g_0	background intensity
g_1	amplitude of the intensity distribution of fringes
k_0	wave number
φ	fringe shift distribution, rad
x	stream-wise coordinate from the throat, mm
y	vertical coordinate on lower wall, mm
λ_0	wave length of a light source in vacuum, nm
K	Gladstone-Dale constant, m ³ /kg
w	span-wise width of duct, mm
M	Mach number
R	gas constant, J/kg-K
Re/m	unit Reynolds number, 1/m
T	temperature, K
δ^*	boundary layer displacement thickness, mm
δ	boundary layer thickness, mm
ρ	density, kg/m ³
ρ_a	the atmospheric density, kg/m ³

Subscripts

b	value at surrounding air
os	total or stagnation state
l	just upstream of shock train

Literature

- [1] MATUO, K.; MIYAZATO, Y.; KIM, H.-D.: Shock train and pseudo-shock phenomena in internal gas flows. *Progress in Aerospace Sciences*. 1999, Vol. 35, Issue 1, pp. 33–100. DOI: [10.1016/S0376-0421\(98\)00011-6](https://doi.org/10.1016/S0376-0421(98)00011-6)
- [2] GNANI, F.; ZARE-BEHTASH, H.; KONTIS, K.: Pseudo-shock waves and their interactions in high-speed intakes. *Progress in Aerospace Sciences*. 2016, Vol. 82, pp. 36–56. DOI: [10.1016/j.paerosci.2016.02.001](https://doi.org/10.1016/j.paerosci.2016.02.001)
- [3] LEE, H. J.; LEE, B. J.; KIM, S. D.; JEUNG, I.-S.: Investigation of the pseudo-shock wave in a two-dimensional supersonic inlet. *Journal of Visualization*. 2010, Vol. 13, Issue 1, pp. 25–32. DOI: [10.1007/s12650-009-0008-3](https://doi.org/10.1007/s12650-009-0008-3)
- [4] QIN, B.; CHANG, J.; JIAO, X.; BAO, W.; YU, D.: Numerical investigation of the impact of asymmetric fuel injection on shock train characteristics. *Acta Astronautica*. 2014, Vol. 105, Issue 1, pp. 66–74. DOI: [10.1016/j.actaastro.2014.08.025](https://doi.org/10.1016/j.actaastro.2014.08.025)
- [5] XU, K.; CHANG, J.; ZHOU, W.; YU, D.: Mechanism of shock train rapid motion induced by variation of attack angle. *Acta Astronautica*. 2017, Vol. 140, pp. 18–26. DOI: [10.1016/j.actaastro.2017.08.009](https://doi.org/10.1016/j.actaastro.2017.08.009)

- [6] LI, N.; CHANG, J.; YU, D.; BAO, W.; SONG, Y.: Mathematical Model of Shock-Train Path with Complex Background Waves. *Journal of Propulsion and Power*. Vol. 33, Issue 2, pp. 468–478. DOI: [10.2514/1.B36234](https://doi.org/10.2514/1.B36234)
- [7] DENG, R.; JIN, Y.; KIM, H. D.: Numerical simulation of the unstart process of dual-mode scramjet. *International Journal of Heat and Mass Transfer*. 2017, Vol. 105, pp. 394–400. DOI: [10.1016/j.ijheatmasstransfer.2016.10.004](https://doi.org/10.1016/j.ijheatmasstransfer.2016.10.004)
- [8] SU, W.-Y.; CHEN, Y.; ZHANG, F.-R.; TANG, P.-P.: Control of pseudo-shock oscillation in scramjet inlet-isolator using periodical excitation. *Acta Astronautica*. 2018, Vol. 143, pp. 147–154. DOI: [10.1016/j.actaastro.2017.10.040](https://doi.org/10.1016/j.actaastro.2017.10.040)
- [9] JIAO, X.; CHANG, J.; WANG, Z.; YU, D.: Periodic forcing of a shock train in a scramjet inlet-isolator at overspeed condition. *Acta Astronautica*. 2018, Vol. 143, pp. 244–254. DOI: [10.1016/j.actaastro.2017.12.005](https://doi.org/10.1016/j.actaastro.2017.12.005)
- [10] XIONG, B.; WANG, Z.-G.; FAN, X.-Q.; WANG, Y.: Experimental study on the flow separation and self-excited oscillation phenomenon in a rectangular duct. *Acta Astronautica*. 2017, Vol. 133, pp. 158–165. DOI: [10.1016/j.actaastro.2017.01.009](https://doi.org/10.1016/j.actaastro.2017.01.009)
- [11] XIONG, B.; FAN, X.-Q.; WANG, Y.; TAO, Y.: Experimental Study on Self-Excited and Forced Oscillations of an Oblique Shock Train. *Journal of Spacecraft and Rockets*. 2018, Vol. 55, Issue 3, pp. 640–647. DOI: [10.2514/1.A33973](https://doi.org/10.2514/1.A33973)
- [12] XIONG, B.; WANG, Z.-G.; FAN, X.-Q.; WANG, Y.: Response of Shock Train to High-Frequency Fluctuating Backpressure in an Isolator. *Journal of Propulsion and Power*. 2017, Vol. 33, Issue 6, pp. 1–9. DOI: [10.2514/1.B36291](https://doi.org/10.2514/1.B36291)
- [13] TAKEDA, M.; INA, H.; KOBAYASHI, S.: Fourier-transform method of fringe-pattern analysis for computer-based topography and interferometry. *Journal of the Optical Society of America*. 1982, Vol. 72, Issue 1, pp. 156–160. DOI: [10.1364/JOSA.72.000156](https://doi.org/10.1364/JOSA.72.000156)
- [14] YAGI, S.; INOUE, S.; NAKAO, S.; ONO, D.; MIYAZATO, Y.: Optical Measurements of Shock Waves in Critical Nozzles at Low Reynolds Numbers. *Journal of Flow Control, Measurement & Visualization*. 2017, Vol. 5, Issue 2, pp. 36–50. DOI: [10.4236/jfcmv.2017.52003](https://doi.org/10.4236/jfcmv.2017.52003)
- [15] TAKESHITA, T.; TAKANO, H.; ONO, D.; NAKAO, S.; MIYAZATO, Y.: Rainbow Schlieren visualization of shock trains in rectangular ducts. In: *Proceedings of the 23rd International Symposium on Air Breathing Engines (ISABE 2017)*. [online]. 2017. Available from WWW: <https://www.isabe.org/>

POUŽITÍ MACH-ZEHNDEROVA INTERFEROMETRU V ŘETĚZCI RÁZU VLN („SHOCK TRAINS“) IZOLÁTORU

Systém Mach-Zehnderova interferometru kombinovaný s vysokorychlostní kamerou se aplikuje na řetězec rázu („shock train“) konstantním přímým kanálem pro vyjasnění jeho nestabilní charakteristiky, kde je Machovo číslo 1,44, Reynoldsovo číslo je $4,97 \times 10^7 \text{ m}^{-1}$ a tloušťka hraniční vrstvy je 0,472 mm. Okamžitého dvojrozměrného hustotního pole v řetězci rázu je kvantitativně dosaženo s vysokým prostorovým rozlišením. Současný Mach-Zehnderův interferometrický systém se jeví jako účinný pro měření nestálé hustoty v rázově dominantních proudech v dvojrozměrném kanálu. Oscilační charakteristika každého rázu v rázovém řetězci je demonstrována výkonovou spektrální analýzou pole nestálé hustoty.

DIE VERWENDUNG DES MACH-ZEHNDER-INTERFEROMETERS IN DER KETTE VON SCHOCKWELLEN („SHOCK TRAINS“) DES ISOLATORS

Das System des Mach-Zehnder-Interferometers ist mit einer Hochgeschwindigkeitskamera kombiniert und findet Anwendung für die Kette von Schockwellen („shock trains“) in einem konstanten direkten Kanal zur Klärung seiner instabilen Charakteristik, wobei die Machzahl 1,44, die Reynoldszahl $4,97 \times 10^7 \text{ m}^{-1}$ und die Dicke der Grenzschicht 0,472 beträgt. Ein sofortiges zweidimensionales Dichtigkeitsfeld in der Kette der Stoßwellen wird quantitativ mit einer hohen Raumunterscheidung erreicht. Das gegenwärtige Mach-Zehnder-interferometrische System erweist sich als wirksam für die Messung unbeständiger Dichte in stoßdominanten Strömungen im zweidimensionalen Kanal. Die Oszillationscharakteristik eines jeden Stoßes in der Stoßkette wird durch eine Leistungsspektralanalyse des Feldes der unbeständigen Dichte demonstriert.

ZASTOSOWANIE INTERFEROMETRU MACHA-ZEHNDERA W ŁAŃCUCHU FAL UDERZENIOWYCH („SCHOCK TRAINS“) IZOLATORA

Zestaw interferometru Macha-Zehndera połączony z szybką kamerą zastosowany został do łańcucha uderzeń („shock train“) w stałym prostym tunelu w celu wyjaśnienia jego niestabilnej cechy, przy czym liczba Macha wynosi 1,44, liczba Reynoldsa wynosi $4,97 \times 10^7 \text{ m}^{-1}$ a grubość warstwy granicznej to 0,472 mm. Pod względem jakościowym, natychmiastowe dwuwymiarowe pole gęstości powstaje w łańcuchu uderzeń z dużą rozdzielczością przestrzenną. Obecny zestaw interferometru Macha-Zehndera wydaje się skuteczny w przypadku pomiarów niestabilnej gęstości w zdominowanych przez wstrząsy przepływach w dwuwymiarowym tunelu. Oscylacyjna charakterystyka każdego wstrząsu w łańcuchu uderzeń prezentowana jest poprzez analizę spektralną pola niestabilnej gęstości.

FLOW CONTROL AROUND A CIRCULAR CYLINDER BY A SMALL ROD

Takayuki Tsutsui

National Defense Academy of Japan, Department of Mechanical Engineering,
1-10-20 Hashirimizu, Yokosuka, Kanagawa, 238-8686, Japan
e-mail: tsutsui@nda.ac.jp

Abstract

Several control methods for the flow around a bluff body have been proposed in previous studies. One such method is the forced reattachment method, which is a type of separated shear layer control that uses a small rod. The small rod is placed in the optimal position on the shear layer from a circular cylinder, thus dividing the shear layer into upper and lower parts. The upper shear layer is supported and elongated by the small rod, and the lower shear layer reattaches and adheres to the rear side of the cylinder. A large stagnant region forms behind the cylinder. This method reduces drag and generates a lift, and is promising for bluff body flow control. However, the forced reattachment phenomenon occurs only under certain conditions. The aim of the present study was to clarify the rod position and diameter required for forced reattachment.

Keywords

Circular cylinder; Flow control; Drag reduction; Fluid force; Flow visualization.

Introduction

Forced reattachment has been reported in previous papers as a unique flow control method [1–5]. Figure 1 (a) is a flow visualization photograph demonstrating this phenomenon. Figure 1 (b) shows a schematic of the forced reattachment phenomenon. A small rod is positioned on the shear layer separated from the upper side of a circular cylinder. In this setup, the upper shear layer is supported and elongated by the small rod, and the lower shear layer reattaches and adheres to the rear side of the cylinder. A large stagnant region forms behind the cylinder. This forced reattachment phenomenon is not an intermittent phenomenon, and the wake motion is thus not active than that of a single circular cylinder [5].

Applying this control method, a drag is reduced and a lift force is generated. These facts regarding the forced reattachment phenomenon have been numerically simulated in a previous study [3]. Recently, the instantaneous characteristics of this method have been reported [5].

The forced reattachment phenomenon occurs only under certain conditions. The aim of this study was to elucidate these conditions, which are related to the position and diameter of the small rod. This paper presents the effect of the position and diameter of the small rod and a mathematical representation of the condition for forced reattachment.

1 Experimental Device and Methods

The coordinate systems and notation used in the present study are shown in Figure 2. The diameter D of the circular cylinder was 40 mm, and the diameter d of the small rod was varied from 2 to 18 mm. The gap G between the cylinder and small rod was varied from 2 to 7 mm. The angular position α of the rod was varied from 90° to 180° .

Experiments were carried out in a low-speed wind tunnel, the working section of which has a height of 1,000 mm, a width of 150 mm, and a length of 1,200 mm. The free-stream velocity U was varied from 6 to 20 m/s, and the turbulent intensity was approximately 0.4% in this velocity range. The Reynolds number based on D ranged from 1.6×10^4 to 6.3×10^4 . In the experiment, d , G , and α were systematically changed, and the surface pressure of the circular cylinder and the vortex shedding frequency were measured. The drag and lift coefficients were obtained by integrating the pressure distribution. The vortex shedding frequencies behind the circular cylinder were obtained from frequency analysis of the velocity fluctuation of an I-type hot-wire anemometer. Flow visualization was conducted using a smoke tunnel.

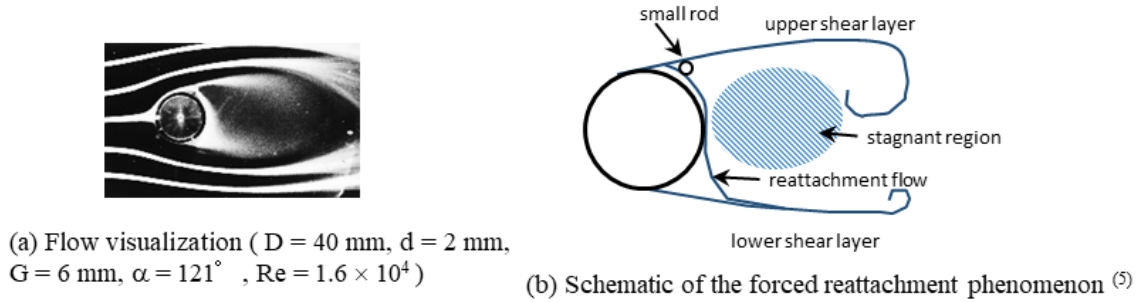


Fig. 1: Forced reattachment.

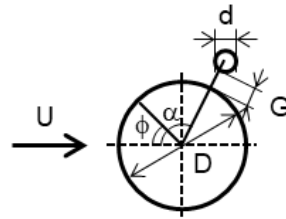


Fig. 2: Coordinate system and notation.

2 Results and Discussion

2.1 Flow Patterns

Typical flow patterns are presented in Figure 3. It shows the pressure distributions and flow visualization photographs for several angular positions of the small rod. The open circle and the dotted line indicate the pressure distribution of the cylinder with and without small rod respectively. Two types of photographs, a long exposure (1 s) photograph and an instantaneous exposure photograph, are included in Figure 3.

At $\alpha = 115^\circ$, the small rod was outside of the separated shear layer from the circular cylinder and had little effect on the pressure distribution.

At $\alpha = 121^\circ$, the forced reattachment phenomenon occurred. The separated shear layer was divided by the small rod, and the lower side of the shear layer reattached at the rear face of the cylinder. In this case, the value of C_p , pressure coefficient, near the separation point at approximately $\phi = 75^\circ$ was much lower than that in the pressure distribution with no rod. The value of C_p then increased suddenly and reached a local maximum in the range of $\phi = 145^\circ$ to 150° because the flow through the gap was accelerated to 1.6 times the free stream velocity and separated under these conditions [4]. The value of C_p on the rear lower face of the cylinder was higher than that in the case of the lone cylinder because of the stagnant region near the rear lower side of the cylinder.

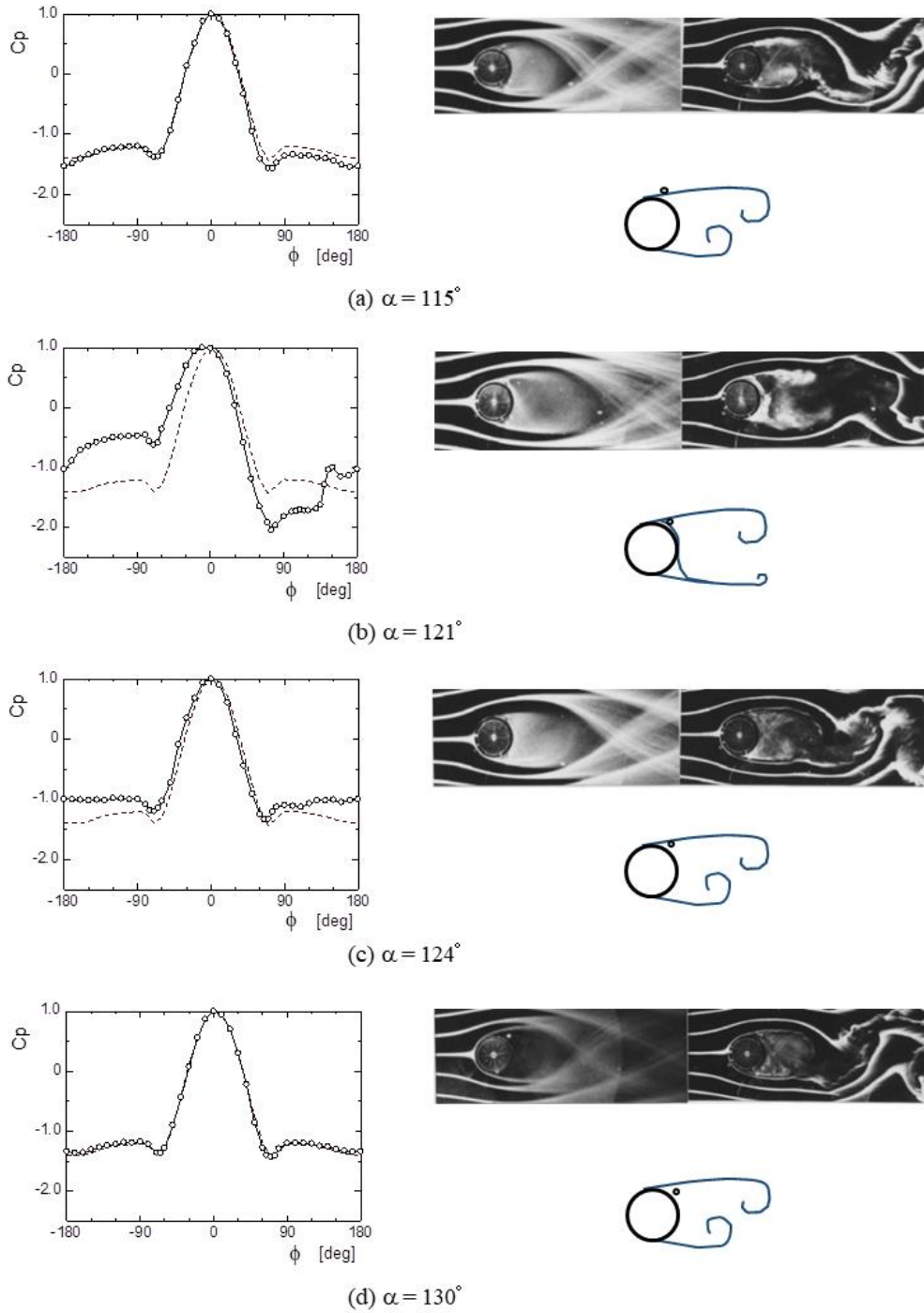


Fig. 3: Flow pattern, pressure distribution and flow visualization photograph at different value of α ($D = 40$ mm, $d = 2$ mm, $G = 6$ mm, $Re = 4.2 \times 10^4$)

At $\alpha = 124^\circ$, the small rod was located just inside the separated shear layer. The forced reattachment phenomenon did not occur, but the separated shear layer was elongated by the support of the small rod. This phenomenon has been described in previous papers [1, 2]. The value of C_p on the rear face was higher than that of the lone circular cylinder.

At $\alpha = 130^\circ$, the small rod was inside the separated shear layer and had little effect on the pressure distribution.

The features of the flow patterns are shown in Figure 4. The drag coefficient C_D , the lift coefficient C_L , and the Strouhal number St are plotted against α in Figure 4. The Strouhal

number is defined as $St = f D / U$, where f is the frequency of vortex shedding from the cylinder. Under the conditions $d = 2$ mm and $G = 6$ mm, forced reattachment occurred at $\alpha = 121^\circ$. In this case, C_D and C_L reached their minimum and maximum recorded values in the range $\alpha = 122^\circ$ to 124° . The change in St with α was dramatic. In the range $\alpha = 90^\circ$ to 110° , vortex shedding was suppressed by the small rod. At $\alpha = 121^\circ$, the value of St decreased as a result of forced reattachment. Just after that, at $\alpha = 124^\circ$, St increased; at this position, forced reattachment did not occur, but the upper separated shear layer was elongated by the support of the small rod, causing the vortex shedding frequency to increase. When α was increased further, St took a constant value of 2.05, which is standard St value for single circular cylinder.

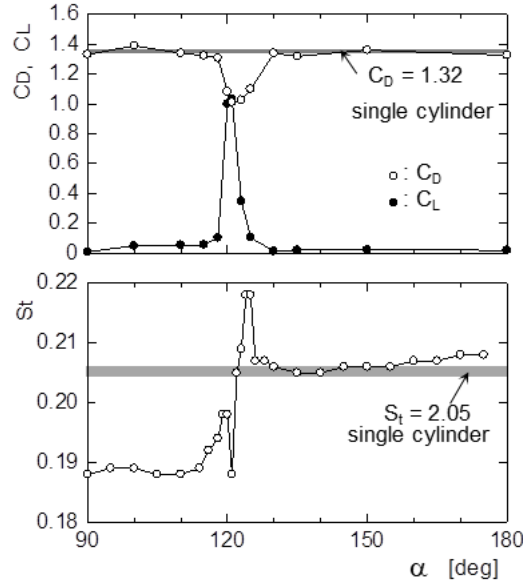


Fig. 4: Drag, lift and Strouhal number plotted against the angular position of the small rod ($D = 40$ mm, $d = 2$ mm, $G = 6$ mm, $Re = 4.2 \times 10^4$)

2.2 Effect of Rod Diameter

The forced reattachment phenomenon occurred with several small rods of different diameters. Figure 5 shows the pressure distributions and flow visualization photographs for $d = 6$, 10, and 18 mm. The open circle and the dotted line indicate the pressure distribution of the cylinder with and without small rod respectively.

For $d = 6$ and 10 mm, the pressure distributions were similar and had features similar to the case with $d = 2$ mm shown in Fig. 3 (b).

For $d = 18$ mm, the pressure distribution was different from that for $d = 2$, 6, and 10 mm. From $\phi = 30^\circ$ to 120° , the value of C_p was higher than that in the case of single circular cylinder and with $d = 2$, 6, and 10 mm because the separated shear layer was dammed by the small rod. Furthermore, from $\phi = -180^\circ$ to -60° , the value of C_p was lower than those in the other cases. On the basis of this pressure distribution, a reduced drag and the generation of lift cannot be expected. In this case, the forced reattachment phenomenon occurs intermittently [3]; that is, its occurrence is unstable.

Figure 6 shows the effect of the small rod diameter on the drag and lift coefficients. The value of C_D was approximately 1.1 and remained almost constant from $d / D = 0.04$ to 0.25; over $d / D = 0.25$, the value of C_D increased with increasing d / D . At $d / D = 0.45$, the value of C_D was 1.6, which exceeds that of single circular cylinder. The value of C_L decreased with

increasing d/D . At $d/D = 0.45$, the value of C_L was negative. These results indicate that there is an optimal rod size for forced reattachment.

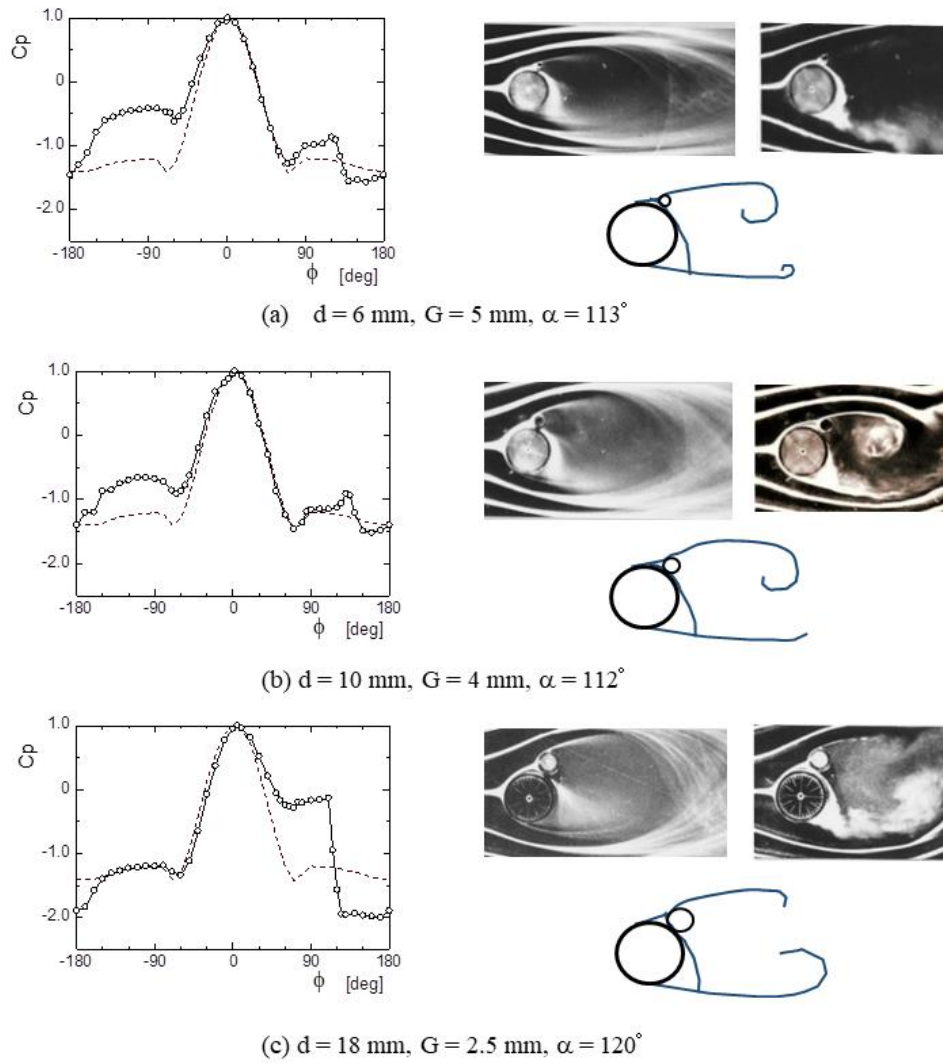


Fig. 5: Effect of small rod diameters ($D = 40 \text{ mm}$, $Re = 4.2 \times 10^4$)

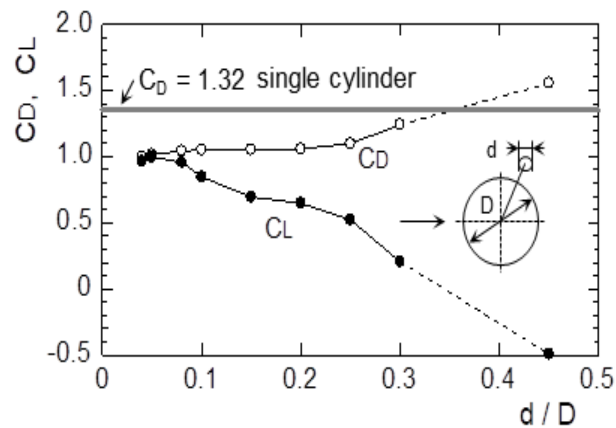


Fig. 6: Effect of rod diameter on drag and lift coefficients

2.3 Optimal Conditions for Forced Reattachment

Figure 7 shows the small rod positions at which the forced reattachment phenomenon occurs. The dotted line indicates the separated shear layer obtained from the photograph of the lone circular cylinder. The open circles show the positions and sizes of the small rod. For forced reattachment to occur, the small rod must be located along the dotted line.

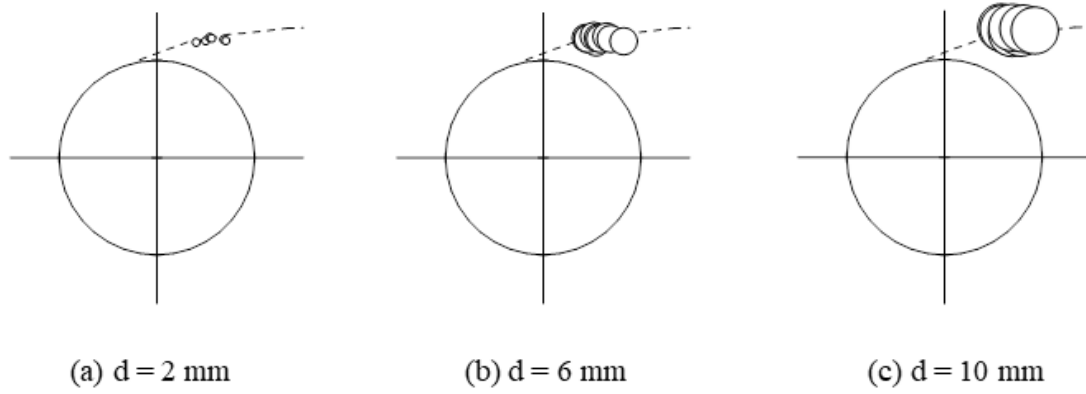


Fig. 7: Location of the small rod

To derive a formula for the angular position α , a simple analysis was performed. The separated shear layer was assumed to lie along the line tangent to the surface of the circular cylinder passing through the separation point, as shown in Figure 8.

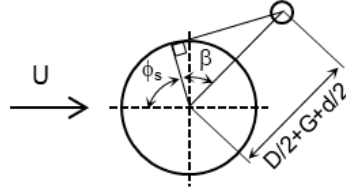


Fig. 8: Analysis of optimum rod position

The forced reattachment phenomenon occurs when the center of the small rod is on this tangent line. The angular position α was derived as function of D , d , and G based on the separation point ϕ_s as

$$\alpha = \phi_s + \beta, \quad \phi_s = 78^\circ \quad (1)$$

$$\cos \beta = (D / 2) / (D / 2 + G + d / 2) \quad (2)$$

$$D = 40 \text{ mm}, d = 2 - 10 \text{ mm}, G = 2 - 7 \text{ mm}.$$

Figure 9 shows the experimental data and the analytical lines for α at different values of D , d , and G . The open circles indicate the experimental conditions under which the forced reattachment phenomenon occurred, and the dotted lines represent the values of α obtained from Equations (1) and (2). The analytical form of α corresponds reasonably well with the experimental data.

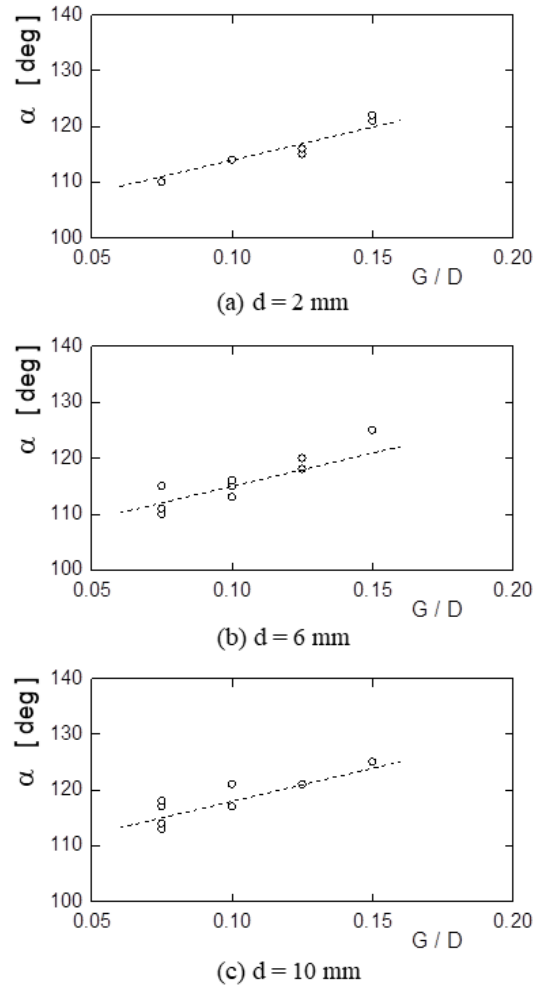


Fig. 9: Optimal rod position

Conclusions

A unique flow control method, the forced reattachment method, was considered in this study. The features of this phenomenon, the effect of the rod size, and the optimal rod size and position were investigated. An equation that can be used to determine the conditions required for occurrence of the forced reattachment phenomenon was successfully derived. The equation was found to be reasonably well with the experimental data. However, if the diameter of the rod is large, reduced drag and the generation of lift cannot be expected.

Literature

- [1] IGARASHI, T.; TSUTSUI, T.: Flow Control around a Circular Cylinder by a Small Cylinder. In: *Proceedings of the 11th Australasian Fluid Mechanics Conference*. Hobart, Australia, 1992, pp. 519–522.
- [2] IGARASHI, T.; TSUTSUI, T.: Flow Force Acting on a Circular Cylinder Controlled by a Small Rod. In: *Proceedings of the 3rd JSME-KSME Fluids Engineering Conference*. Sendai, Japan, 1994, pp. 571–576.
- [3] TSUTSUI, T.; IGARASHI, T.; KAMEMOTO, K.: Interactive flow around two circular cylinders of different diameters at close proximity. Experiment and numerical analysis by vortex method. *Journal of Wind Engineering and Industrial Aerodynamics*. 1997, Volumes 69–71, pp. 279–291. DOI: [10.1016/S0167-6105\(97\)00161-X](https://doi.org/10.1016/S0167-6105(97)00161-X)

- [4] TSUTSUI, T.; IGARASHI, T.: Flow control around a circular cylinder by a small cylinder (Properties of reattachment jet). In: *Proceedings of the 3rd ASME-JSME Joint Fluids Engineering Conference*. San Francisco, California, FEDSM'99-6943, 1999.
- [5] TSUTSUI, T.: Instantaneous fluid force acting on a circular cylinder control by a small rod. *EPJ Web of Conferences*. 2018, Vol. 180, Paper No. 02110. DOI: [10.1051/epjconf/201818002110](https://doi.org/10.1051/epjconf/201818002110)

OVLÁDÁNÍ PRŮTOKU KOLEM KRUHOVÉHO VÁLCE MALOU TYČÍ

V předchozích studiích bylo navrženo několik kontrolních metod pro tok kolem oblého tělesa. Jednou z takových metod je metoda nuceného opětovného přiřazení, což je typ separátního řízení smykové vrstvy, která používá malou tyč. Malá tyč je umístěna v optimální poloze na smykové vrstvě z kruhového válce, čímž se rozděluje smykovou vrstvu na horní a dolní část. Horní smyková vrstva je nesena a prodloužena malou tyčí, a spodní smyková vrstva se připojí a přilne k zadní straně válce. Za válcem se tvoří velká stojatá oblast. Tato metoda snižuje tah a vytváří zdvih a pomáhá řízení toku kolem oblého tělesa. Avšak fenomén nuceného opětovného připojení nastává pouze za určitých podmínek. Cílem této studie bylo objasnit polohu a průměr tyče potřebné pro nucené opětovné nasazení.

STEUERUNG DER DURCHFLUSSMENGEN UM DIE KRESIWALZE DURCH EINE KLEINE STANGE

In den vorangegangenen Studien wurden einige Kontrollmethoden für den Fluss um einen runden Körper entworfen. Eine dieser Methoden ist die Methode der gezwungenen wiederholten Zuordnung, was einen Typ der separaten Steuerung der Rutschschicht darstellt, welche sich einer kleinen Stange bedient. Die kleine Stange wird in einer optimalen Position auf der Rutschschicht aus der Kreiswalze heraus gelagert, wodurch die Rutschschicht in einen oberen und einen unteren Teil geteilt wird. Die obere Rutschschicht wird getragen und verlängert von der kleinen Stange, und die untere Rutschschicht schmiegt sich an die hintere Seite der Walze an. Hinter der Walze bildet sich ein großer stehender Bereich. Diese Methode vermindert den Zug und schafft eine Hebung und hilft der Steuerung des Flusses um den runden Körper herum. Aber das Phänomen der gezwungenen wiederholten Anbindung tritt nur unter bestimmten Bedingungen ein. Ziel dieser Studie war die Klärung der Position und des Durchschnitts der Stange, welche für den erzwungenen wiederholten Einsatz notwendig ist.

KONTROLOWANIE PRZEPŁYWU WOKÓŁ OKRĄGŁEGO CYLINDRA PRZY POMOCY MAŁEGO DRAŻKA

W wyniku poprzednich badań zaproponowano kilka metod służących kontroli przepływu wokół okrągłego ciała. Jedną z takich metod jest metoda wymuszonego ponownego przyczepienia, będąca rodzajem oddzielnego kontrolowania warstwy ścinającej, wykorzystująca mały drążek. Mały drążek umieszczony jest w optymalnym położeniu w warstwie ścinającej okrągłego cylindra, w wyniku czego warstwa ta jest podzielona na część górną i dolną. Górna warstwa jest niesiona i zostaje przedłużona przez mały drążek a dolna warstwa przyczepia się do tylnej strony cylindra. Za cylindrem powstaje duży obszar stojącej cieczy. Metoda ta zmniejsza opór i powoduje unoszenie, pomagając w kontroli przepływu wokół okrągłego ciała. Zjawisko wymuszonego ponownego przyczepienia powstaje jednak tylko w pewnych warunkach. Celem opisywanych badań było wyjaśnienie położenia i średnicy drążka niezbędnych dla wymuszonego ponownego przyczepienia.

Miscellanea

EFFICIENT HEATING AND COOLING WITH BOREHOLE HEAT EXCHANGERS

Axel Gerschel¹; Markus Haack²; Prasanth Subramani; Lukas Stöckmann; Thomas Schäfer; Tom Walter; Tino Schütte; Jörn Krimmling

Hochschule Zittau/Görlitz, University of Applied Sciences,
Fakultät Wirtschaftswissenschaften und Wirtschaftsingenieurwesen,
Theodor-Körner-Allee 16, 02763, Zittau, Germany
e-mail: ¹axel.gerschel@hszg.de; ²m.haack@hszg.de

Abstract

Ground-source heat pumps are a sustainable technology to increase the use of renewable energy sources. In order to exploit the maximum potential of near-surface geothermal energy, optimization concepts for borehole heat exchanger systems that combine heating and cooling are being developed at the University of Applied Sciences Zittau/Görlitz. The objectives of this research are not only the reduction of primary energy consumption but also the development of predictive models for system planning, especially with respect to the influence of groundwater. Additionally, constructive and economic aspects of borehole heat exchanger systems are evaluated.

Keywords

Near-surface geothermal energy; Heat pump; Borehole heat exchanger; Renewable energy; Seasonal thermal energy storage; Groundwater flow.

Introduction

The use of near-surface geothermal energy for heating and cooling of buildings is an efficient alternative to conventional systems. Utilizing geological subsoil as a heat source and sink provides large potential for saving primary energy. By this, it helps to achieve ambitious energy transition targets [1]. Together with panel heating and cooling systems, geothermal probes are particularly suitable as underground heat exchangers. Ground-source heat pump (GSHP) systems can unfold their maximum performance capabilities by using subsoil as thermal storage and in case of combined heating and cooling applications. For this purpose further research on planning methods, prediction models and practical operational concepts are essential. Therefore, an interdisciplinary junior research group at Zittau/Görlitz University of Applied Sciences was established. This group consists of researchers specialized in the fields of applied mathematics, engineering, geosciences and economics.

1 Optimization Issues of Geothermal Energy Systems

The main topic of research deals with geothermal energy supply concepts for non-residential buildings. In addition to covering heating demand, the energy supply systems in these buildings more and more often have to cover construction and usage-related cooling demand. However, complex energy demand structures lead in planning practice often to uncertainties in the design of borehole heat exchanger (BHE) fields [2]. Therefore, the optimal utilization of natural regeneration and energy storage effects of the subsoil requires the development of new approaches in the constructive design of the BHE field and the BHE itself. Associated problems have to be investigated through parameter studies with the aid of high-resolution numerical building and system simulation models. The aim is to systematize the decision-

making process for an optimal system configuration (building and its entire technical equipment) by model-based optimization and evaluation of multidimensional efficiency criteria. Additional aspects are the assessment of planning models with respect to their prediction accuracy and the evaluation of over as well as under dimensioning effects in the constructive design of BHEs.

2 The Influence of Geology and Groundwater

The heat transport and possible thermal storage in the subsoil varies considerably, depending on local geological and hydrogeological conditions. Hence, the influence of the prevailing geology and groundwater situation in association with the usage of near-surface geothermal energy is another key topic of this research project. Detailed knowledge of the thermal properties of the subsoil is essential for a profound design of BHE systems. In this context, the thermal conductivity and heat capacity of the rock layers as well as natural underground temperature belong to the most important properties that are highly location-dependent. Unfortunately, hydrogeological factors, especially convective heat transport induced by groundwater flow, are often neglected during system dimensioning. The reason for this is that currently no well-engineered application-oriented planning guide exists for this specific problem. In addition, generation of costly and time-consuming numerical groundwater flow models are often not justified in planning practice [3, 4]. However, especially when the geological subsoil is used as a seasonal thermal storage by combined heating and cooling applications, the groundwater flow induces convection that influences the system performance negatively. The ignorance of groundwater flow may lead to under dimensioning of BHE fields. Contrary to that, groundwater flow can increase the performance of solo heating applications. The utilization of the subsoil rock for thermal storage can increase the efficiency of ground-source heat pump systems. Therefore, considerations of hydrogeological factors in the development of planning and design tools are inevitable.

The above-mentioned questions are being answered within the framework of thermo-hydraulic modelling at Zittau/Görlitz University of Applied Sciences. The permeability coefficient (k_f -value) and the effective porosity of relevant rock layers as well as the hydraulic gradient of groundwater belong to the hydraulic aquifer properties in the centre of attraction [3]. These hydrogeological parameters have to be systematized with respect to their influence on the heat transport and its consequences for the overall system dimensioning. Based on this, simplifications can be derived for perspective developments of new approaches in dimensioning of BHE fields.

3 BHE Test Bench for Experimental Investigations

In order to validate the model through experimental investigation a test bench equipped with extensive measurement technology is available (Fig. 1). The system consists of three BHEs of type PE-Xa 32 mm double-U with different depths arranged in triangular form. Heating operation can be realized by means of a built-in compression chiller. On the other hand, simulation of the cooling operation, as well as feeding of solar thermal energy, can be realized with the help of a gas-condensing boiler. All main components as well as integrated thermal buffer storage are connected to each other via a comprehensive hydraulic system (Fig. 2). All BHEs, including the control probe at the centre, have a full-length fieldbus sensor system to measure the temperature every meter in depth.

The system design allows operations of single or multiple BHEs with individually adjustable flow rates and defined heating or cooling power (heating power: max. 132 kW, cooling power: max. 45 kW, circulation pump: max. 12.6 m³/h). The operating range of the test bench

goes from $-10\text{ }^{\circ}\text{C}$ to $+90\text{ }^{\circ}\text{C}$ in order to map operating points of commercially available heat pump systems adequately.

In addition to sophisticated model validation, the test bench is used for determining the location-dependent storage utilization rate depending on borehole depth [5]. By doing so, the influence of groundwater convection on thermal storage process can also be analysed.

4 Constructive Issues of BHEs

The analysis of constructive and material-technical issues of BHEs represents another important topic. Here, mechanically, thermally and chemically induced damages on geothermal probes are under investigation. BHE installation mistakes are a frequent cause of mechanical damage. Structural damage in the grout material caused by intensive and rapid frost-thaw cycles is one of the reasons for thermally induced damage. As a possible consequence, undesired annular gaps between grout and probe may form. If a damaged segment of borehole backfilling is located in the depth of aquifers, this is critical with regard to the system tightness, demanded by the authorities. The same is true in case of chemical decompositions of the grout caused by unsuitable materials in corrosive underground conditions. Without the presence of groundwater, the cavities or defects within the grout act as a thermal insulation, which leads to a reduction in the BHE performance. Therefore, the objectives of research are to analyze possible damages caused by means of multiphysical simulations and to derive recommendations for reduction of risk of damage.



Fig. 1: Test bench (from left to right): gas-condensing boiler, compression chiller, thermal storage

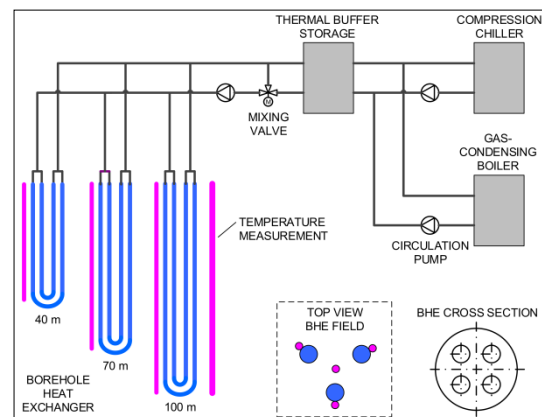


Fig. 2: System scheme

Conclusion

The junior research group in the ESF-funded research project „*Thermal storage process around borehole heat exchanger for heating and cooling of buildings with heat pumps*“ provides the opportunity to examine the complex topics of near-surface geothermal energy in multidisciplinary manner at Zittau/Görlitz University of Applied Sciences. With reference to the increasing demand of energy supply in buildings using heat pumps, an application-oriented contribution to the planning practice can be realized.

Acknowledgment

The European Union and Free State of Saxony fund the described research project. For professional advice, many thanks also go to Prof. Dr. Jens Meinert.

Literature

- [1] BUNDESMINISTERIUM FÜR WIRTSCHAFT UND ENERGIE (2015): *Energieeffizienzstrategie Gebäude*. Brochure. 146 pp. Berlin.
- [2] BAYER, P.; de PALY, M.; BECK, M. (2014): Strategic optimization of borehole heat exchanger field for seasonal geothermal heating and cooling. *Applied Energy*. Vol. 136, pp. 445–453. DOI: [10.1016/j.apenergy.2014.09.029](https://doi.org/10.1016/j.apenergy.2014.09.029)
- [3] KÖLBEL, T. (2010): *Grundwassereinfluss auf Erdwärmesonden: Geländeuntersuchungen und Modellrechnungen*. Dissertation. 146 pp. Karlsruher Institute of Technology.
- [4] BAUER, D. (2011): *Zur thermischen Modellierung von Erdwärmesonden und Erdsonden-Wärmespeichern*. Dissertation. 121 pp. University of Stuttgart.
- [5] KRIMMLING, J. et al. (2015): Speichervorgänge im Umfeld vertikaler Erdsonden von Wärmepumpen. *HLH*. Vol. 66 (1): 19 pp.

EFEKTIVNÍ KONCEPTY NA TOPENÍ A CHLAZENÍ POMOCÍ GEOTERMÁLNÍCH SOND

Na pozadí stanovení energeticko-politických cílů představují tepelná čerpadla spojená se zemí slibnou technologií na zásobování budov termickou energií. Na odkrytí nevyužívaných potenciálů v povrchní geotermii jsou proto na Vysoké škole Zittau/Görlitz vyvíjeny optimalizační koncepty na zařízení geotermálních sond v kombinovaném topném a chladicím provozu. Hlavní zaměření výzkumu náleží úspoře primární energie, jakož i zlepšení prediktivních modelů pro návrh zařízení, zvláště s ohledem na vliv podzemních vod. Předmětem studie jsou také konstrukční a ekonomické aspekty systémů geotermálních sond.

EFFIZIENTE HEIZ- UND KÜHLKONZEPTE MIT ERDWÄRMESONDEN

Vor dem Hintergrund energiepolitischer Zielstellungen [1] sind erdgekoppelte Wärmepumpen eine zukunftsfähige Technologie für die thermische Gebäudeenergieversorgung. Zur Erschließung von ungenutzten Potenzialen in der oberflächennahen Geothermie werden daher an der Hochschule Zittau/Görlitz Optimierungskonzepte für Erdwärmesondenanlagen im kombinierten Heiz- und Kühlbetrieb entwickelt. Hierbei steht die Einsparung von Primärenergie ebenso wie die Verbesserung von Vorhersagemodellen zur Anlagenauslegung, insbesondere unter Berücksichtigung von Grundwassereinfluss, im Fokus der Forschung. Untersuchungsgegenstand sind darüber hinaus konstruktive und wirtschaftliche Aspekte von Erdwärmesondenanlagen.

EFEKTYWNE KONCEPCJE OGRZEWANIA I CHŁODZENIA PRZY POMOCY SOND GEOTERMALNYCH

W odniesieniu do celów określonych w zakresie polityki energetycznej pompy ciepłe połączone z ziemią stanowią obiecującą technologię służącą do zasilania budynków energią cieplną. W celu zbadania niewykorzystanego potencjału geotermii powierzchniowej w Szkole Wyższej Zittau/Görlitz opracowywane są koncepcje optymalizujące urządzenia sond geotermalnych pracujących w trybie ogrzewania i chłodzenia. Badania skupiają się głównie na oszczędności energii pierwotnej a także udoskonaleniu modeli prognostycznych w celu zaprojektowania urządzeń, ze szczególnym uwzględnieniem wpływu wód podziemnych. Przedmiotem badań są także aspekty konstrukcyjne i ekonomiczne systemów sond geotermalnych.




LIST OF AUTHORS

Name	E-Mail and Page Number of Contribution	
Shigeyuki Hibi	hibiteru@nda.ac.jp	7
Kazuki Yabushita	-	7
Robert Kalista	robert.kalista@doosan.com	17
Lukáš Kanta	-	17
Lev Feldberg	-	17
Alexander Kandaurov	kandaurov@hydro.appl.sci-nnov.ru	28
Daniil Sergeev	sergeev4758@gmail.com	28
Yuliya Troitskaya	yuliya@hydro.appl.sci-nnov.ru	28
Marek Pátý	marek.paty@fs.cvut.cz	39
Jan Halama	-	39
Petr Schovanec	petr.schovanec@tul.cz	58
Walter Garen	-	58
Sandra Koch	-	58
Walter Neu	-	58
Petra Dančová	-	58
Darina Jašíková	-	58
Michal Kotek	-	58
Václav Kopecký	-	58
Taishi Takeshita	y7mba011@eng.kitakyu-u.ac.jp	68
Shinichiro Nakao	-	68
Yoshiaki Miyazato	-	68
Takayuki Tsutsui	tsutsui@nda.ac.jp	78
Axel Gerschel	axel.gerschel@hszg.de	88
Markus Haack	m.haack@hszg.de	88
Prasanth Subramani	-	88
Lukas Stöckmann	-	88
Thomas Schäfer	-	88
Tom Walter	-	88
Tino Schütte	-	88
Jörn Krimmling	-	88

GUIDELINES FOR CONTRIBUTORS

Guidelines for contributors are written in the form of a template which is available as a Word document at http://acc-ern.tul.cz/images/journal/ACC_Journal_Template.docx.

EDITORIAL BOARD

<i>Editor in Chief</i>  Prof. Ing. Pavel Mokrý, Ph.D.	Technical University of Liberec pavel.mokry@tul.cz
<i>Assistant of the Editor in Chief</i>  Prof. Ing. Miroslav Žižka, Ph.D.	Technical University of Liberec miroslav.zizka@tul.cz
<i>Executive Editor</i>  PaedDr. Helena Neumannová, Ph.D.	Technical University of Liberec helena.neumannova@tul.cz phone: +420 734 872 413

Other Members of the Editorial Board

 Doc. PaedDr. Hana Andrášová, Ph.D.	University of South Bohemia in České Budějovice andras@pf.jcu.cz
 Doc. PhDr. Tomáš Kasper, Ph.D.	Technical University of Liberec tomas.kasper@tul.cz
 Prof. Ing. Jiří Militký, CSc.	Technical University of Liberec jiri.militky@tul.cz
 Doc. Ing. Iva Petříková, Ph.D.	Technical University of Liberec iva.petrikova@tul.cz
 Doc. Dr. Ing. Miroslav Plevný	University of West Bohemia in Pilsen plevny@fek.zcu.cz
 Doc. Ing. Petr Šidlof, Ph.D.	Technical University of Liberec petr.sidlof@tul.cz
 Dr. Eckhard Burkatzki	TU Dresden / IHI Zittau burkatzki@tu-dresden.de
 Prof. Dr.-Ing. Frank Hentschel	Hochschule Zittau / Görlitz f.hentschel@hszg.de
 Prof. Dr. phil. PhDr. (MU Brno) Annette Muschner	Hochschule Zittau / Görlitz a.muschner@hszg.de
 Dr. Piotr Gryszel	Universitet Ekonomiczny we Wrocławiu Wydział Ekonomii Zarządzania i Turystyki piotr.gryszel@ue.wroc.pl
 Prof. UE Dr. hab. Elżbieta Sobczak	Universitet Ekonomiczny we Wrocławiu Wydział Ekonomii Zarządzania i Turystyki elzbieta.sobczak@ue.wroc.pl
 Prof. UE Dr. hab. Grażyna Węgrzyn	Universitet Ekonomiczny we Wrocławiu Wydział Ekonomii Zarządzania i Turystyki grazyna.wegrzyn@ue.wroc.pl

Assistant of the editorial office:

Ing. Dana Nejedlová, Ph.D., Technical University of Liberec, Department of Informatics,
phone: +420 485 352 323, e-mail: dana.nejedlova@tul.cz

Název časopisu (<i>Journal Title</i>)	ACC JOURNAL
Rok/Ročník/Číslo (<i>Year/Volume/Issue</i>)	2019/25/1 (2019/XXV/Issue A)
Autor (<i>Author</i>)	kolektiv autorů (<i>composite author</i>)
Vydavatel (<i>Published by</i>)	Technická univerzita v Liberci Studentská 2, Liberec 1, 461 17 IČO 46747885, DIČ CZ 46 747 885
Schváleno rektorem TU v Liberci dne	15. 1. 2019, č. j. RE 01/19
Vyšlo (<i>Published on</i>)	30. 6. 2019
Počet stran (<i>Number of pages</i>)	95
Vydání (<i>Edition</i>)	první (<i>first</i>)
Číslo publikace (<i>Number of publication</i>)	55-001-19
Evidenční číslo periodického tisku (<i>Registry reference number of periodical print</i>)	MK ČR E 18815
Počet výtisků (<i>Number of copies</i>)	60 ks (<i>pieces</i>)
Adresa redakce (<i>Address of the editorial office</i>)	Technická univerzita v Liberci Akademické koordinační středisko v Euroregionu Nisa (ACC) Studentská 2, Liberec 1 461 17, Česká republika Tel. +420 485 352 318, Fax +420 485 352 229 e-mail: acc-journal@tul.cz http://acc-ern.tul.cz
Tiskne (<i>Print</i>)	Vysokoškolský podnik Liberec, spol. s r.o. Studentská 1402/2, Liberec 1 460 01, Česká republika

Upozornění pro čtenáře

Příspěvky v časopise jsou recenzovány a prošly jazykovou redakcí.

Readers' notice

Contributions in the journal have been reviewed and edited.

Předplatné

Objednávky předplatného přijímá redakce. Cena předplatného za rok je 900,- Kč mimo balné a poštovné. Starší čísla lze objednat do vyčerpání zásob (cena 200,- Kč za kus).

Subscription

Subscription orders must be sent to the editorial office. The price is 40 € a year excluding postage and packaging. It is possible to order older issues only until present supplies are exhausted (8 € an issue).

Časopis ACC JOURNAL vychází třikrát ročně (červen, září, prosinec).

Three issues of ACC JOURNAL are published every year (June, September, December).

Liberec – Zittau/Görlitz – Wrocław/Jelenia Góra

© Technická univerzita v Liberci – 2019

ISSN 1803-9782 (Print)

ISSN 2571-0613 (Online)